



**MULTIDIMENSIONAL ANALYSIS OF  
ATMOSPHERIC NUCLEAR DETONATIONS**

DISSERTATION

Robert C. Slaughter, Captain, USAF

AFIT-ENP-DS-15-S-029

**DEPARTMENT OF THE AIR FORCE  
AIR UNIVERSITY**

**AIR FORCE INSTITUTE OF TECHNOLOGY**

**Wright-Patterson Air Force Base, Ohio**

DISTRIBUTION STATEMENT A  
APPROVED FOR PUBLIC RELEASE; DISTRIBUTION UNLIMITED.

The views expressed in this document are those of the author and do not reflect the official policy or position of the United States Air Force, the United States Department of Defense or the United States Government. This material is declared a work of the U.S. Government and is not subject to copyright protection in the United States.

MULTIDIMENSIONAL ANALYSIS OF ATMOSPHERIC NUCLEAR  
DETONATIONS

DISSERTATION

Presented to the Faculty  
Graduate School of Engineering and Management  
Air Force Institute of Technology  
Air University  
Air Education and Training Command  
in Partial Fulfillment of the Requirements for the  
Degree of Doctor of Philosophy

Robert C. Slaughter, B.S., M.S.  
Captain, USAF

16 September 2015

DISTRIBUTION STATEMENT A  
APPROVED FOR PUBLIC RELEASE; DISTRIBUTION UNLIMITED.

MULTIDIMENSIONAL ANALYSIS OF ATMOSPHERIC NUCLEAR  
DETONATIONS

Robert C. Slaughter, B.S., M.S.  
Captain, USAF

Committee Membership:

Dr. John W. McClory  
Chairman

Col Karl C. Walli, PhD  
Member

Col Matthew D. Sambora, PhD  
Member

Maj Benjamin R. Kowash, PhD  
Member

ADEDJI B. BADIRU, PhD  
Dean, Graduate School of Engineering and Management

## Abstract

Digitized versions of atmospheric nuclear testing films represent a unique data set that enables the scientific community to create accurate multidimensional data using modern digital image processing techniques. The focus of this research is to develop methods for 3-dimensional reconstructions and temperature distributions of the early time nuclear fireballs. Initial developments have resulted in the first 2-dimensional temperature distribution of a nuclear fireball using digitized film. This temperature analysis underwent verification using the Digital Imaging and Remote Sensing Image Generation model and validation using historic thermal output data in combination with a 1-dimensional heat flux technique. This same process was then extended to perform the first limb-darkening calculation of nuclear fireballs. Limb darkening coefficients were then used to derive a temperature profile of the nuclear fireball as a function of optical path length. A 3-dimensional reconstruction was performed using a variation of a structure from illuminance technique in combination with limb-darkening coefficients to produce structure using a single image. This dissertation also highlights the difficulties in using common computer vision feature descriptors such as Scaled Invariant Feature Transform and Speeded Up Robust Features on the nuclear weapons testing films because of the expanding and emissive nature of the nuclear fireball. The use of these techniques to produce accurate dense reconstructions is likely to require both single image and multiple view geometry in order to produce consistently accurate results.

*Dedicated to my beautiful bride and our little girl*

## Acknowledgements

Like all things in life the more challenging the obstacle, the more you rely on other people for support. There is no way that I could have completed this document without the support of advisers, mentors, peers, and of course family and friends. There naturally are too many to name, but here are a few:

I'd like to thank and acknowledge the Defense Threat Reduction Agency, National Nuclear Security Administration, Air Force Technical Applications Center, Sandia National Laboratory, and Lawrence Livermore National Laboratory for providing feedback, input, funding, and/or support of this research. There were a long list of technical experts at these organizations that provided me invaluable insight into nuclear detonation phenomenon.

I want to thank Peter Kuran and James Moye for always being responsive to questions and for teaching me everything I know about film. I want to thank Tyler Peery and Austin DeLorme for frequent edits of all my work. Lt Col Dan Schmidt for assisting in research and in many ways mentoring me. I want to send a special thank you to Dr. Greg Spriggs for having a vision and starting investigation into scientific nuclear testing films. I believe you have opened Pandora's box, and have enabled the ability to perform scientific investigations into a phenomena that ideally the world will never have the ability to record firsthand again.

My committee members Col Matthew Sambora and Maj Ben Kowash who both challenged me to dive deeper into a variety of different aspects of my research. Col Karl Walli for educating me on computer vision and digital image processing, as well as being my original supporter in helping me start this endeavor.

I want to especially thank my research adviser Dr. John McClory for mentoring me, educating me, and ultimately being the epitome of "service before self". Thank you for taking on an additional research student while already being over booked.

For all the late nights, early mornings, and weekend work, a direct result of always having a generous open door policy and taking such amazing care of both myself and all the rest of your students. Thank you.

To my friends in particular TJ, Jess, Scot, Austin, Tyler, and Amanda, thank you for being the most amazing friends on the planet. To my family, in particular my parents, thank you for always supporting me and valuing my education. I want to thank my daughter Audrey, for not always crying, for being adorable, and for doing cute baby things. And last, but certainly not least, my wife Jennifer for not only providing professional support (graphic design and proof reading), but for being the most loving and supportive partner anyone could ask for these last three years.

Thank you.

Robert C. Slaughter

## Table of Contents

	Page
Abstract .....	iv
Acknowledgements .....	vi
List of Figures .....	x
List of Tables .....	xiii
List of Abbreviations .....	xiv
I. Introduction .....	1
1.1 Overview and Research Objectives .....	1
1.2 Overview of Atmospheric Nuclear Testing .....	2
1.3 Fireball Physics .....	4
1.4 Early Fireball Growth .....	5
1.5 Nuclear Yield Estimation .....	7
1.6 Dissertation Outline .....	8
II. Introduction To Digitized Nuclear Testing Films .....	10
2.1 Introduction .....	10
2.2 Historical Nuclear Testing Films .....	10
2.3 Introduction to Scanned Nuclear Testing Films .....	11
2.4 Historical Nuclear Film Preparation .....	19
2.5 Film and Rapatronic Plate Dimensions .....	22
2.6 Digitized Nuclear Testing Film Intensity Variation .....	24
2.7 Summary .....	27
III. 2D Temperature of Nuclear Fireballs .....	31
3.1 2D Temperature Introduction .....	31
3.2 Research Methodology .....	33
Conversion From Digital Counts to Energy .....	33
Real World Time Alignment .....	34
Power Temperature Derivation .....	34
3.3 Results .....	40
Power Temperature Results .....	40
Thermal Yield Calculation .....	40
3.4 Validation and Verification of Results .....	47
Verification of Results Using DIRSIG .....	47
Validation of Results Using Heat Flux Method .....	51
Limitations of Results .....	52

	Page
3.5 Discussion . . . . .	53
IV. Limb-Darkening Analysis of Nuclear Detonations . . . . .	55
4.1 Limb-Darkening Laws . . . . .	55
Introduction . . . . .	55
Limb-Darkening Laws Overview . . . . .	60
Film Analysis . . . . .	62
RANSAC . . . . .	64
4.2 Results . . . . .	66
Limb-Darkening Coefficients . . . . .	66
Limb-Darkening Coefficients Validation and Verification . . . . .	70
Limb-Darkening Law Consistency . . . . .	76
Temperature Profiles from Limb-Darkening Laws . . . . .	79
4.3 Discussion . . . . .	82
V. 3D Reconstructions of Nuclear Fireballs . . . . .	84
5.1 Computer Vision Introduction . . . . .	84
Multiple View Geometry Reconstruction . . . . .	84
Bundle Adjustment . . . . .	88
Feature Detection . . . . .	88
3D Reconstruction Uncertainty . . . . .	90
Issues with Automatic Feature Detection . . . . .	92
5.2 3D Reconstruction of a Nuclear Fireball . . . . .	96
3D Reconstruction Using Limb-Darkening Coefficients . . . . .	96
Limb-Darkening Coefficients . . . . .	100
Single Image 3D Reconstruction Limitations . . . . .	103
5.3 Time Alignment Using the Fundamental Matrix . . . . .	104
5.4 Discussion . . . . .	109
VI. Conclusions . . . . .	111
6.1 Dissertation Summary . . . . .	111
6.2 Recommendations for Future Work . . . . .	112
Bibliography . . . . .	114

## List of Figures

Figure	Page
1. Camera Truck .....	11
2. Golden-Eye Scanner.....	12
3. MF OD Curve.....	14
4. Scanned Step Wedge .....	15
5. Scanned Step Wedge Irradiance Example .....	16
6. MF HD Curve Example .....	17
7. Timing Mark.....	18
8. Frame of First Light .....	19
9. Lacquered Image .....	20
10. Scratched Image .....	21
11. Rapatronic Plate Image .....	23
12. Difference in Scans (Minutes Apart) .....	24
13. Two Scans of the Same Frame .....	28
14. Fireball Variance Single Frame .....	29
15. Variance in Scans .....	30
16. Historical Power Temperature Tesla .....	32
17. W-12 Yellow Filter.....	36
18. Threshold Image .....	37
19. Temperature Weighting Function .....	39
20. Power Temperature Wasp Prime .....	41
21. Power Temperature for Event Tesla .....	42
22. Wasp Prime temperature at $T_{min}$ .....	43

Figure	Page
23. Wasp Prime Temperature at $T_{max}$ .....	44
24. Tesla Temperature at $T_{min}$ .....	45
25. Tesla temperature at $T_{max}$ .....	46
26. DIRSIG Wasp Prime Scene .....	49
27. Verification of Temperature Using DIRSIG .....	50
28. Heat Flux Method Wasp Prime .....	52
29. Wasp Prime Temperature .....	54
30. Wasp Prime Limb-Darkening .....	56
31. Limb-Darkening Graphic .....	57
32. Limb-Darkening Geometry .....	59
33. Wasp Prime Centroid .....	63
34. RANSAC Used For Limb-Darkening .....	65
35. Limb-Darkening Results Equation 15 .....	66
36. Limb-Darkening Results Equation 16 .....	67
37. Limb-Darkening Results Equation 17 .....	68
38. Limb-Darkening Results Equation 18 .....	68
39. Limb-Darkening Results Equation 19 .....	69
40. Limb-Darkening Results Equation 20 .....	70
41. Limb-Darkening Results Equation 21 .....	71
42. $T_{min}$ Limb-Darkening Comparison at $T_{min}$ .....	72
43. $T_{max}$ Limb-Darkening Comparison at $T_{max}$ .....	73
44. $T_{min}$ Limb-Darkening Difference Image .....	74
45. $T_{max}$ Limb-Darkening Comparison .....	75
46. Limb-Darkening Intensity Profile .....	77

Figure	Page
47. Limb-Darkening Law Comparison . . . . .	78
48. Intensity Profile Average Wasp Prime . . . . .	79
49. Limb-Darkening as a Function of Time . . . . .	80
50. Temperature Profile Wasp Prime $T_{min}$ . . . . .	81
51. Temperature Profile Wasp Prime $T_{max}$ . . . . .	82
52. Epipolar Geometry . . . . .	86
53. SIFT Matches . . . . .	90
54. Tesla Tower . . . . .	91
55. Sparse Point Cloud . . . . .	93
56. Sparse Point Cloud Side . . . . .	94
57. ColorTesla . . . . .	95
58. 3D Spares Reconstruction . . . . .	97
59. Limb-Darkening Analysis Using RANSAC (Wasp Prime) . . . . .	99
60. 3D Reconstruction Using RANSAC . . . . .	100
61. 3D NUDET Image . . . . .	102
62. Time Alignment Using Fundamental Matrix Test Setup . . . . .	105
63. Deflating Balloon Figure . . . . .	106
64. Time Alignment Using Fundamental Matrix Test Results . . . . .	107
65. Time Allignment Using F-Test . . . . .	108

## List of Tables

Table	Page
1. Overview of United State Atmospheric Nuclear Testing Operations . . . . .	3
2. Temperature Profile for Various Limb-Darkening Laws . . . . .	62
3. Limb-Darkening Results Compared to Film: Per Film . . . . .	76
4. Limb-Darkening Results Compared to Film: Per Equation . . . . .	76
5. Time Alignment of Frames Using F-Test . . . . .	109

## List of Abbreviations

Abbreviation	Page	
3D	3-dimensional . . . . .	1
1D	1-dimensional . . . . .	1
DoD	Department of Defense . . . . .	1
LLNL	Lawrence Livermore National Laboratory . . . . .	1
2D	2-dimensional . . . . .	8
EG&G	Edgerton, Germeshausen, and Grier . . . . .	10
MF	Microfile . . . . .	10
HD	Hurter-Driffield . . . . .	13
$T_{max}$	time at temperature maximum . . . . .	37
$T_{min}$	time at temperature minimum . . . . .	38
DIRSIG	Digital Imaging and Remote Sensing Image Generation Model . . . . .	47
RANSAC	Random Sample Consensus . . . . .	63
SIFT	Scaled Invariant Feature Transform . . . . .	89
SURF	Speeded Up Robust Features . . . . .	89

# MULTIDIMENSIONAL ANALYSIS OF ATMOSPHERIC NUCLEAR DETONATIONS

## I. Introduction

### 1.1 Overview and Research Objectives

The primary objective of this research is to extend the dimensionality of the analysis of nuclear detonations. In particular, the focus is on multidimensional temperature and 3-dimensional (3D) reconstructions of nuclear fireballs. Nearly all nuclear diagnostic information has relied upon 1-dimensional (1D) analysis to support scientific investigation of capabilities and limitations of Department of Defense (DoD) nuclear effects related mission areas. The United States is now looking to address a growing threat-space with a focus on isolated terrorist activities as opposed to nation-to-nation warfare. As a result, requirements have emerged for which 1D analysis methods may be insufficient. Additionally, further reductions in nuclear warheads mandated in the Strategic Arms Reduction Treaty (New Start Treaty) have reduced the acceptable margins of error. Multidimensional analysis provides the modern approach to nuclear weapon effects studies required to meet the national nuclear mission objectives of today and into the future.

Lawrence Livermore National Laboratory (LLNL) recently began the digitization of all United States atmospheric nuclear testing films. These films represent a unique data set that will allow the scientific community access to the information necessary to expand upon the knowledge of nuclear weapon effects. This data set has the potential to provide accurate multidimensional atmospheric nuclear weapon effects data.

This dissertation outlines the work that has been performed to increase the dimensionality of analysis of atmospheric nuclear detonations. In particular, this research focuses on the time-varying dimensions and temperature of the early time nuclear fireballs. It is the author's assessment that with knowledge of the time varying fireball temperature and dimensions that most other parameters used for thermal or shock nuclear effects results can be derived.

## 1.2 Overview of Atmospheric Nuclear Testing

The first nuclear weapons test, Project Trinity, was conducted in 1945. From 1945-1962 the United States conducted a total of 210 atmospheric, underwater, and space nuclear detonation tests (summarized in Table 1) [1]. Atmospheric nuclear testing spanned 20 tests series, advancing the United State's understanding of nuclear weapon design, effects, and diagnostic capability. Following the signing of the Limited Test Ban Treaty all nuclear detonation testing for the United States moved underground.

Although nuclear testing continued for the United States for another 30 years, much of the data regarding atmospheric nuclear weapons effects was generated during this roughly 17 year period of atmospheric testing. The primary reason this data is so valuable is that the majority of nuclear weapon effects are a byproduct of the interaction between the nuclear detonation and its surrounding environment. This environment includes not only the case surrounding the physics package, but also materials near the point of detonation to include delivery mechanism, atmosphere, and, in some cases, the ground. In many scenarios these interactions between nuclear explosion and the surrounding environment cannot be duplicated with an underground test.

Additionally, following the presidential moratorium on nuclear weapons testing of 1992, the United States put an end to all super critical nuclear weapons testing

**Table 1. Overview of United State Atmospheric Nuclear Testing Operations**

<b>Test Series</b>	<b>Year</b>	<b>Number of Tests</b>
Project Trinity	1945	1
Operation Crossroads	1946	2
Operation Sandstone	1948	3
Operation Ranger	1951	5
Operation Greenhouse	1951	4
Operation Buster-Jangle	1951	7
Operation Tumbler-Snapper	1952	8
Operation Ivy	1952	2
Operation Upshot-Knothole	1953	11
Operation Castle	1954	6
Operation Teapot	1955	14
Operation Wigwam	1955	1
Operation Redwing	1956	17
Operation Plumbbob	1957	24
Operation Hardtack I	1958	34
Operation Argus	1958	3
Operation Hardtack II	1958	19
Operation Dominic I	1962	36
Operation Dominic II	1962	4
Plowshare Program	1961-1962	9

of any kind. Over the course of the next two decades, the Department of Energy transitioned its efforts into a stockpile stewardship program.

This long term moratorium highlights the importance of data collected during the five decades of domestic nuclear testing. The original and re-analysis of these tests represent an invaluable source of technical information that will guide key decisions regarding a multitude of current and future DoD mission areas. In particular, the nuclear weapon effects data generated during testing that was conducted in the 1950's and the 1960's is the only source of testing information that can be used to answer some of the scientifically strenuous questions being asked in the 21st century and beyond.

### 1.3 Fireball Physics

Upon reaching criticality, a nuclear detonation releases a near instantaneous amount of energy in the form of fission fragments, x-rays, neutrons, and gamma rays. These particles interact with the surrounding environment to include the bomb casing, delivery mechanism, and any other adjacent material. The majority of energy released in a nuclear explosion is in the form of x-rays.

These x-rays deposit their energy in the surrounding material for low altitude events. In air, this energy is deposited in a radius on the order of meters. This volumetric region around the detonation, referred to as the x-ray fireball, is heated to temperatures on the order of millions of degrees Kelvin. Expansion of this fireball can be segmented into three phases of growth: burn out, diffusion, and hydrodynamic.

Initially at  $10^7$  Kelvin this fireball region has more in common with a plasma than to the fire observed in a conventional explosive. This stage of fireball growth is referred to as burn out. For the 1D approximation, the complete ionization of surrounding material continues until a burn out radius is reached. The rate at which

the radiation front absorbs the x-ray radiation and re-emits approaches the speed of light in a vacuum for higher yields [2, 3]. The total amount of volume in the burn out phase of growth is material and yield dependent; the radius of that volume is on the order of meters for air, and on the order of centimeters for metals.

Following the complete ionization of surrounding material, the fireball will eventually cool to a point in which only partial ionization is induced, marking the beginning of the diffusive growth phase. During this phase, the volume of the fireball continues to expand, while the average temperature continues to decrease. Diffusion refers to the process by which molecules interact due to the kinetic energy of motion. For a nuclear detonation, this diffusion process occurs near the fireball edge where the colder surrounding air and other materials interact with the nuclear fireball that is at a temperature high enough to continue to thermally radiate x-rays.

This diffusive fireball growth continues until the rate of expansion decreases below the local acoustic velocity of sound. At this time, a shock wave advances ahead of the radiation front, in a process referred to as hydrodynamic separation [4, 5]. During this time, the inner fireball continues to growth diffusively.

During hydrodynamic separation, the temperature at the surface of the shock front is greater than 100,000 K. The volume encompassing the shock front continues to advance and the temperature in the shock front decreases following a hydrodynamic growth model. Eventually the temperature of the shock front is reduced to approximately 3,000 K upon which the inner fireball can now be observed again (in a phenomenon called breakaway).

#### 1.4 Early Fireball Growth

The expansion of the early time fireball can be modeled as a system in which a finite amount of energy is instantaneously released in a uniform medium. This can

be expressed as

$$R = \left( \frac{t}{0.926} \right)^{\frac{2}{5}} \frac{Y^{1/5}}{\rho_o^{1/5}}, \quad (1)$$

where  $R$  is the radius of fireball,  $t$  is the time since detonations,  $\rho_o$  is the density of the medium and  $Y$  is the yield or the energy that is released. Equation 1 is commonly referred to as Taylor's equation [4].

If the uncertainty in radius is the dominating term, then the uncertainty ( $\sigma$ ) in the yield determined from Equation 1 can be approximated as

$$\frac{\sigma_Y}{Y} = 5 \frac{\sigma_R}{R}. \quad (2)$$

In Equation 2,  $\sigma_R$  is the uncertainty in the radius, and  $\sigma_Y$  is the uncertainty in yield. A 5% uncertainty in radius results in a 25% uncertainty in yield. One way to reduce this large uncertainty is to determine fireball volume instead of fireball radius for yield analysis. Replacing radius with the volume,  $V$ , of a sphere, the uncertainty in yield becomes

$$\frac{\sigma_{Yield}}{Yield} = \frac{5}{3} \frac{\sigma_{Volume}}{Volume}. \quad (3)$$

A 5% uncertainty in volume results in an approximately 8% uncertainty in yield. Hence, if analytical volume methods can be developed with accuracy equivalent to radius measurements, then uncertainty in fireball yields using Taylor's method will be reduced by a factor of 3. A volume measurement is also more representative of an actual nuclear detonation because fireballs are never perfectly spherical. This is

especially true for tower and surface interacting detonations.

## 1.5 Nuclear Yield Estimation

There are several standard ways to calculate the yield of a nuclear detonation using prompt output of the device. One technique in determining nuclear yield is using an analytical solution, such as Taylor's equation (Equation 1) or an empirical scaling law such as the time to minimum optical output [6]. In general, a scaling law measures a key feature's magnitude over time, the timing of a key feature, or the maximum or minimum observation of a physical component.

An empirical scaling law can be an effective and consistent way to determine device yield. However, in order for a scaling law to be developed, historical precedence must be observed and the event of interest must be similar to the events used to derive the scaling law. In other words, a scaling law determined through observation of free air burst is not necessarily applicable to tower shots and vice versa. This is a fundamental limitation that becomes increasingly troublesome when investigating diagnostic methods for determining nuclear yield following a hypothetical detonation in a complex environment.

Scaling laws derived from an analytical solution are severely limited because in constructing a closed form solution a number of assumptions are made. These assumptions many times are appropriate for some event scenarios, such as a free air detonation, but are not appropriate for complex ones, such as a detonation on a barge. In order to better understand these more complex environments modern computation fireball codes have been developed [7, 8, 9, 10]

These modern multidimensional codes represent an effective way to analyze nuclear fireballs in complex environments. However, reliable and trustworthy 3D nuclear fireball data sets are necessary for validation. Multidimensional fireball codes require

multidimensional fireball data. Prior to the digitization of fireball data, this type of validation was limited.

## 1.6 Dissertation Outline

The focus of this dissertation is to provide the first multidimensional fireball data analysis from digitized atmospheric nuclear testing film. The objective is to demonstrate the ability to treat fireball films like detectors and to provide the initial steps in expanding the dimensionality of fireball analysis. In order to better understand the analysis done in other chapters, Chapter II of this dissertation provides an introduction to the digitized nuclear testing films. Chapter III demonstrates the methodology and provides results for the first 2-dimensional (2D) temperature calculation using digitized film. Chapter's II and III provide the foundation for the argument that the scanned nuclear testing films can be treated like detectors for use in thermal analysis.

The temperature of a nuclear fireball influences not only the optical output, but also the rate at which the fireball expands. However, the calculations provided in Chapter III only determine the apparent temperature. The apparent temperature is the temperature of which the fireball would be if it was a Lambertian surface. Because a nuclear fireball is not a Lambertian surface, but a radiating gas, Chapter IV demonstrates how limb-darkening coefficients can be used to determine the temperature of the nuclear fireball as a function of optical path length into the fireball. This temperature profile is much more representative of the actual physical phenomenon being observed.

Chapter V of this dissertation demonstrates how these same limb-darkening coefficients can then be used to produce a 3D reconstruction of a nuclear fireball using a single image. Chapter V also introduces the theory of 3D reconstructions using multiple view geometry and highlights the issues and limitations of current computer

vision algorithms in performing accurate reconstructions of nuclear fireballs. Chapter VI further summarizes research results and provides an outline for proposed future research.

The methodology presented in this dissertation is intended to be used to advance scientific understanding towards the capabilities and limitations of DoD mission areas. It is envisioned that the methodology outlined in this dissertation will aid in advancing nuclear diagnostic capabilities as well as the assist in the validation of multidimensional nuclear effect codes.

## II. Introduction To Digitized Nuclear Testing Films

### 2.1 Introduction

Atmospheric nuclear testing films represent an invaluable scientific resource to the nuclear weapon effects community. By scanning these nuclear testing films, digital image processing techniques can be used to perform modern analysis on a historical data set. For many applications, an understanding of how to treat film like a detector is required.

This chapter provides an introduction to the historical nuclear testing films as well as an introduction to the film scanning process. This chapter discusses how to convert digitized pixel intensity into optical density and the issues and uncertainties of that process. The film scanning process discussed in this chapter was the process used for all films analyzed in the remainder of this dissertation.

### 2.2 Historical Nuclear Testing Films

There are several thousand films spanning over 200 atmospheric nuclear tests. The films were captured using a variety of different cameras by Edgerton, Germeshausen, and Grier (EG&G) in the 1950's and 1960's using 8 mm, 16 mm, and 35 mm film [11]. The resulting footage captured the early fireball growth, the early plume rise, and the late plume following detonation. The films used a wide variety of different emulsions, the most common being Microfile (MF). MF was a film originally developed by Kodak for the nuclear testing program [12]. MF was used predominately because of its ability to retain its chemical properties in high radiation environments and its high resolution due to the granularity of MF film [12].

Each nuclear test had dozens of cameras record different time periods of nuclear phenomenon ranging from the first few microseconds using rapatronic plates, to min-

utes of data recorded by cameras with 15 second exposure times. The cameras were configured at specific sites, located on one side a truck or trailer and triggered using a variety of different timing mechanisms [13, 14]. An example of the layout of one of these camera arrays is shown in Figure 1.

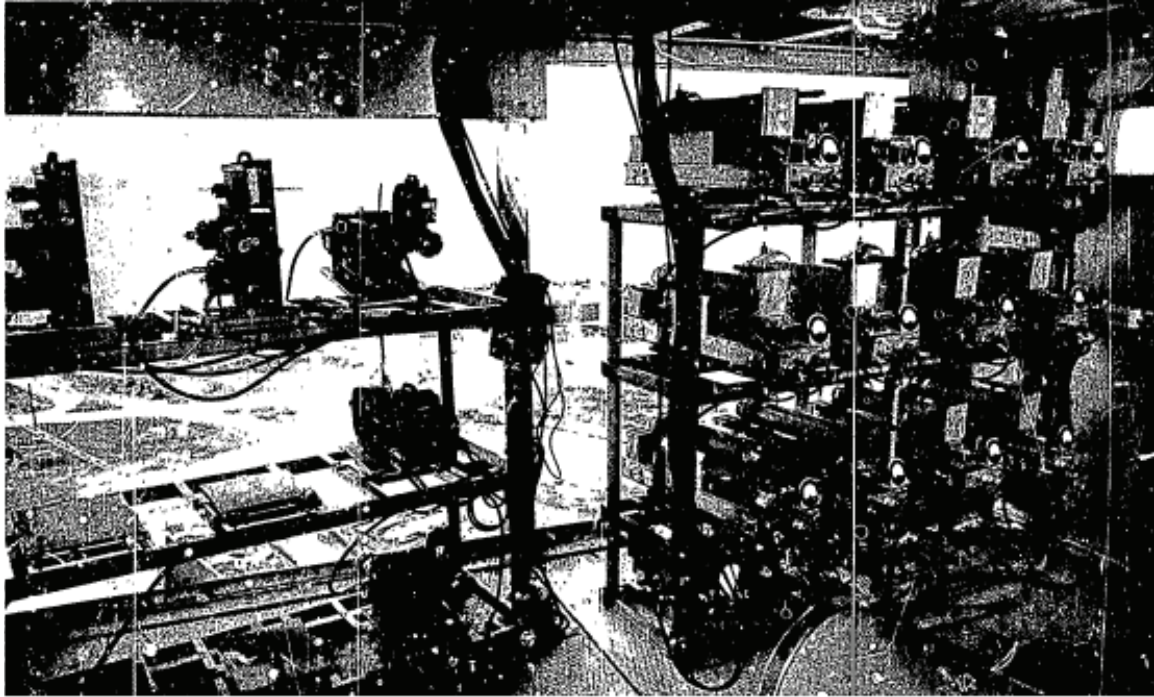


Figure 1. A typical arrangement of camera trucks used to capture scientific testing data for an atmospheric nuclear detonation.

### 2.3 Introduction to Scanned Nuclear Testing Films

LLNL has digitally scanned some of the United States atmospheric nuclear testing films with the objective of making a digital copy of the original film. Each scan records the optical density at every location on the frame. The primary objective of the LLNL film scanning research is to provide benchmark data for widespread use within the nuclear weapon effects community.

LLNL uses a Goldeneye film scanner developed by Image Systems AB and Digital Vision (Figure 2) [11]. This scanner consists of a 4096 pixel vertical sensor. Each



Figure 2. The Golden-Eye scanner used by LLNL to digitize nuclear testing films [11].

frame of the film is scanned independently, providing a series of 16 bit .tif or .png images. This 16 bit number has a direct relationship to the optical density recorded by the original films. One can convert between the two using the following relationship

$$D = \frac{V}{V_{max}} D_{max} \quad (4)$$

where  $D$  is the optical density detected by the pixel,  $V$  is the 16-bit value in the scanned file,  $D_{max}$  is the maximum optical density that can be represented by the image, and  $V_{max}$  is the maximum value a pixel can have in the file ( $2^{16}$  for 16 bit).

The nuclear test films were run through a sequence of diagnostics to verify the Goldeneye film scanner's ability to accurately capture the optical densities of films. Figure 3 shows the results of analyzing the accuracy of translating optical density readings in the MF film scanning process. The technical film scanning process properly records optical density from films with an uncertainty of approximately 2%.

In order to use film like a detector, optical density must be converted to physical units such as irradiance ( $W/m^2$ ), using what is referred to as a Hurter-Drifffield (HD). The HD curve is a function of silver halide activation which in turn is dependent on photon irradiance. The HD curve is also dependent upon the film development process. For nuclear testing films, HD curves were determined from recorded step wedges. Typically a 21 step wedge is used in optical density increments of 0.15 [15], typically starting with an optical density near 0 up to an optical density slightly above 3. An example of a step wedge, registered across several frames to appear as if in one image is shown in Figure 4.

The HD curve can be determined by plotting the change in pixel intensity across this step wedge as shown in Figure 5. Figure 5 shows the intensity value of a single vertical line of pixels taken from Figure 4. The HD curve for this film can be determined by plotting the change in pixel intensity at each of 0.15 optical density

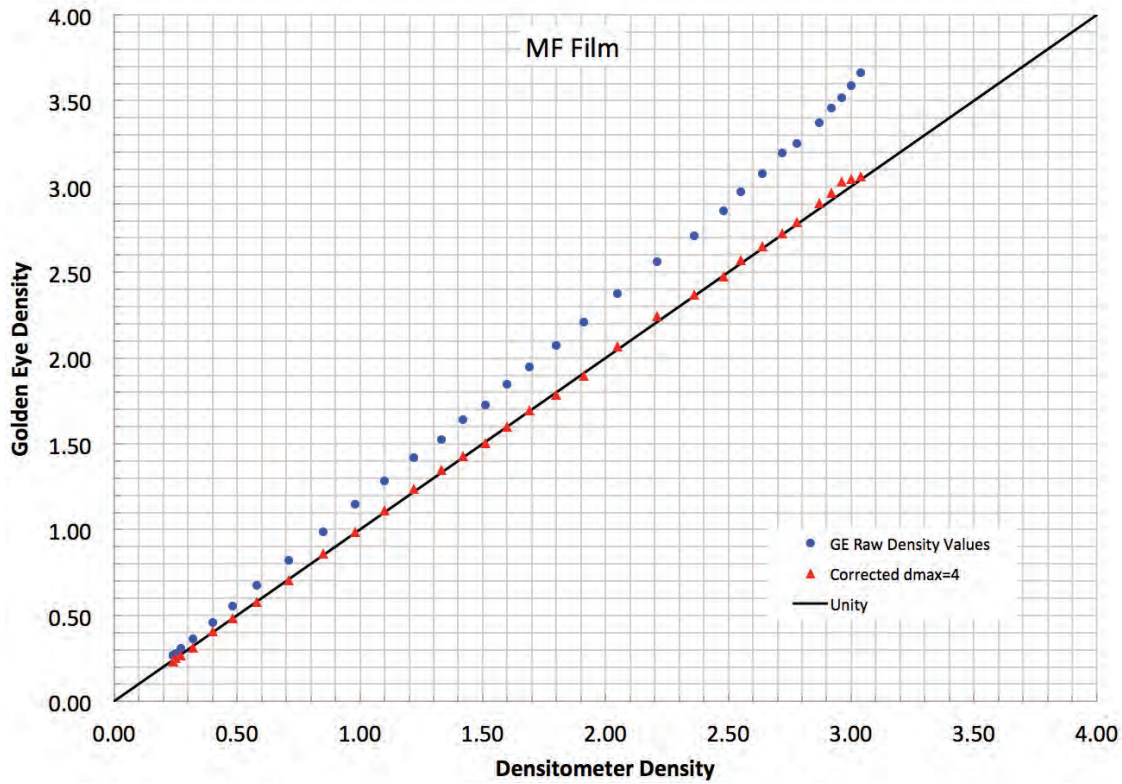


Figure 3. Golden-Eye scanner capability to reproduce the physical optical density measurements for MF film [11]. The blue dots are the original conversion of digital counts to optical densities prior to calibration. The red triangles show the ability of the Golden-Eye to accurately record digital counts to their equivalent optical density following a calibration.

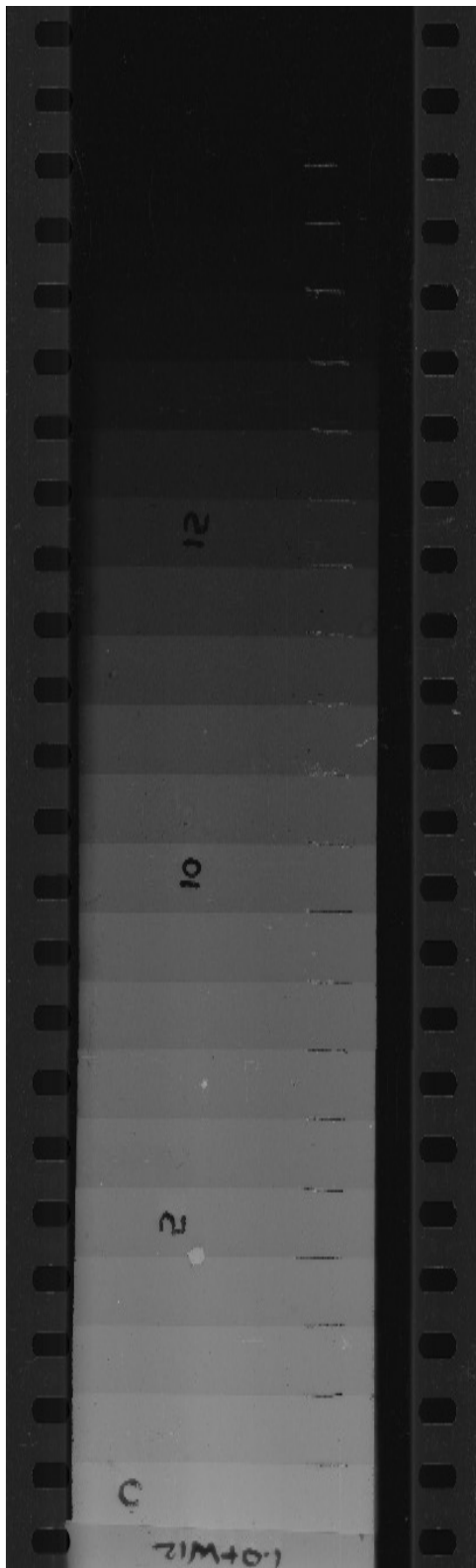
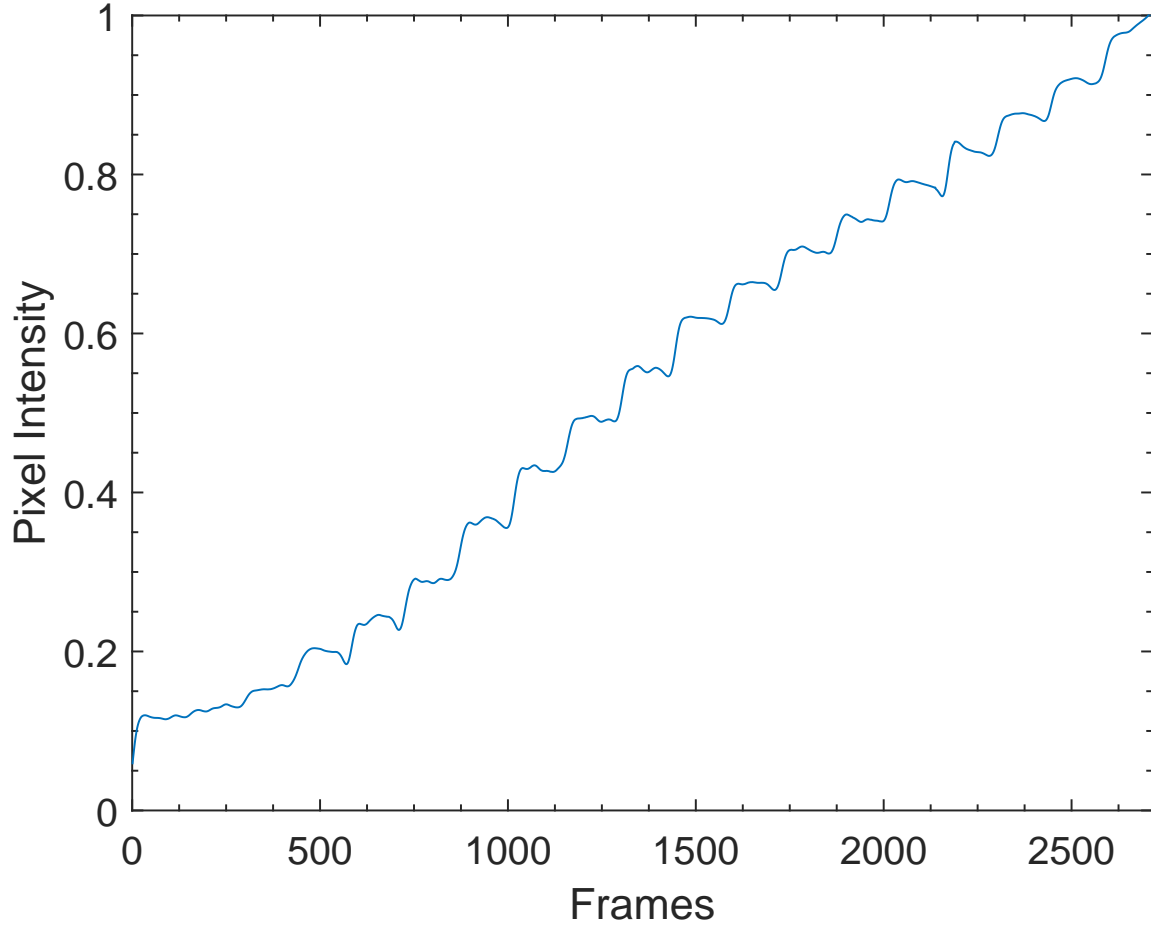


Figure 4. A 21 step wedge as it appears in MF film. This image was stitched together to appear as one although the full sequence spread through several scanned frames.

increments with an assumption made about the irradiance at an optical densities of zero. Figure 6 is the resulting HD curve derived for the step wedge shown in Figure 4.



**Figure 5.** Scanned intensity of a step wedge frame sequence.

The technical validity of the film data is of primary concern, in particular, the quality of the film scan and integrity of the original optical density values. The majority of recordings were acrylate or polyethylene based black and white films, which have an expected lifespan of 100-500 years according to ANSI Standard IT9.11-1992. Colored films from this time frame only had a life expectancy of a few years, resulting in the loss of valuable technical information. The original purpose of the films was technical analysis of different time periods in the evolution of the nuclear

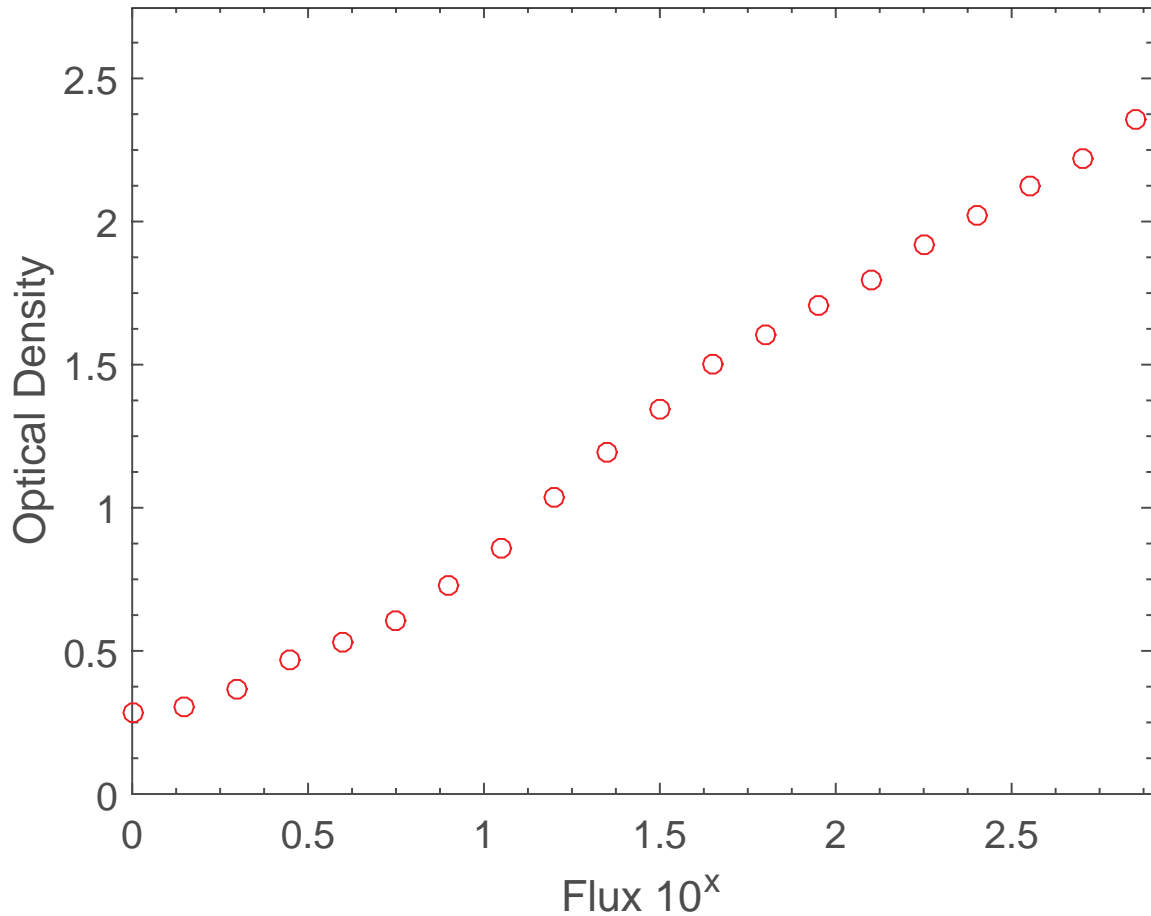


**Figure 6.** Example of an MF HD curve derived from a step wedge.

detonation. The data capturing methods (such as using radiation resistant MF film) were designed specifically for technical evaluation. If an accurate digital replica could be made from the original film, then more modern methods could be used to analyze the films.

Time alignment between frames of various cameras is also important in order to treat film like a detector. Because the frame rate of mechanical reels varies through the film recording process, timing marks were imprinted on the film using a very accurate timing circuit that flashed at set intervals. An example of these circuit flashes as they appear on the films is shown in Figure 7.

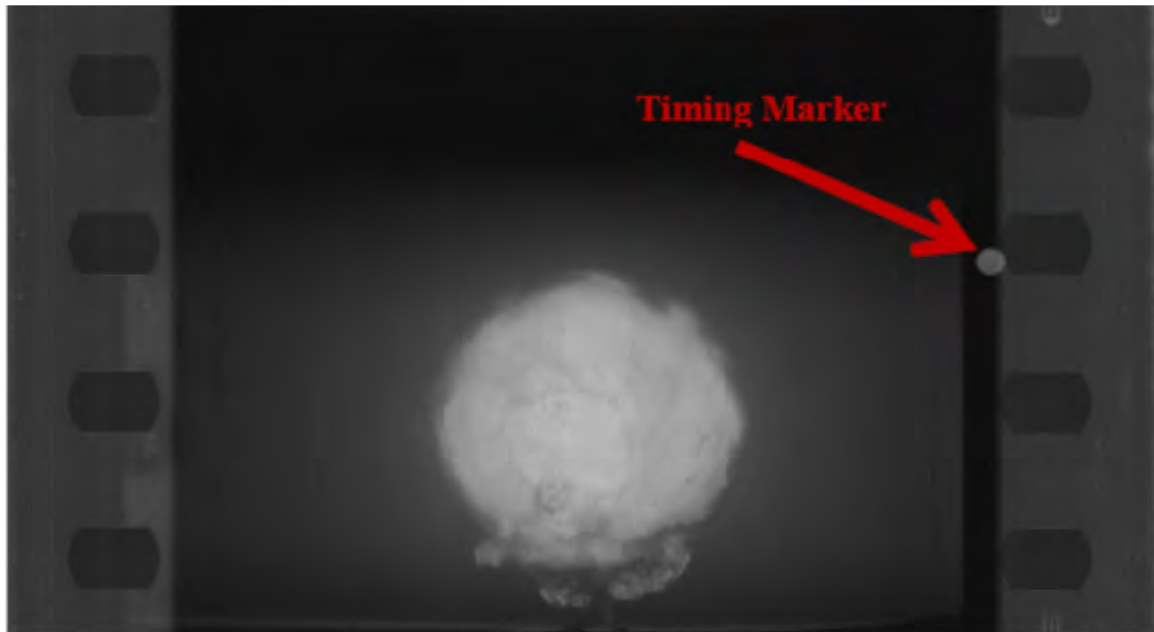


**Figure 7.** An example of a circular timing mark on a digitized early fireball film [6].

These timing marks can be used as accurate time stamps for conversion between frames and true time. The interpolation between timing mark points within the film sequence and the dynamic frame rate determines the true timing scale. With a true time standard, multiple cameras can be synchronized and frames that overlap in time can be compared to one another. However, because an exact time zero cannot be established from this simple analysis, one cannot know the true time from detonation

more accurately than half a frame. This is because the frame that observes the initial detonation, the frame of first light, has an exposure time of one over the frame rate. Figure 8 depicts the transition from frames just prior to and immediately following the frame of first light.

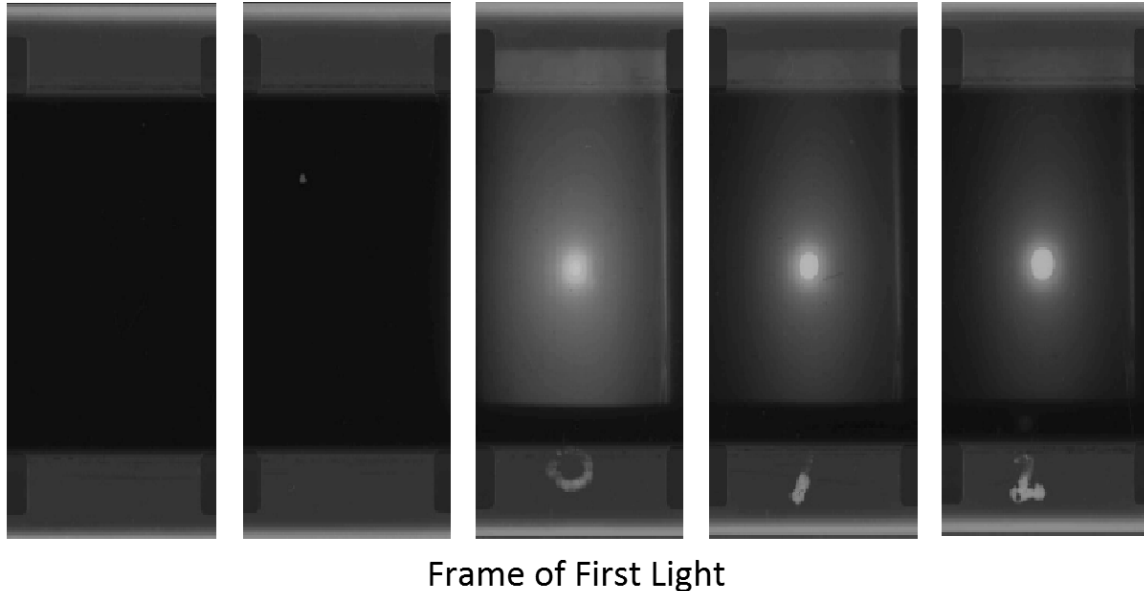


**Figure 8.** The frame of first light and the transition of recorded testing film just prior to detonation to those early frames of fireball radiance. As shown, there is a half a frame uncertainty in time for the exact moment of detonation [11].

## 2.4 Historical Nuclear Film Preparation

The integrity of the film after years of storage is a primary concern of this project. There is a combination of different chemical and physical interactions that can be detrimental to film integrity. These interactions that effect film integrity include scratching on the original films, emulsion deterioration, shrinkage, buckling, fluting, twisting and curling, spoking and embossing, chemical decomposition, and vinegar syndrome.

The original films were coated by EG&G with lacquer in order to prevent them from getting scratched, dirty, or compromised. In most cases, after the films were an-

alyzed, the lacquer was removed. In some of the films the lacquer was never removed. An example of this shown in Figure 9. Even though the films were lacquered, in many cases the films still were scratched. There are many films that show scratches throughout the films as shown in Figure 10.

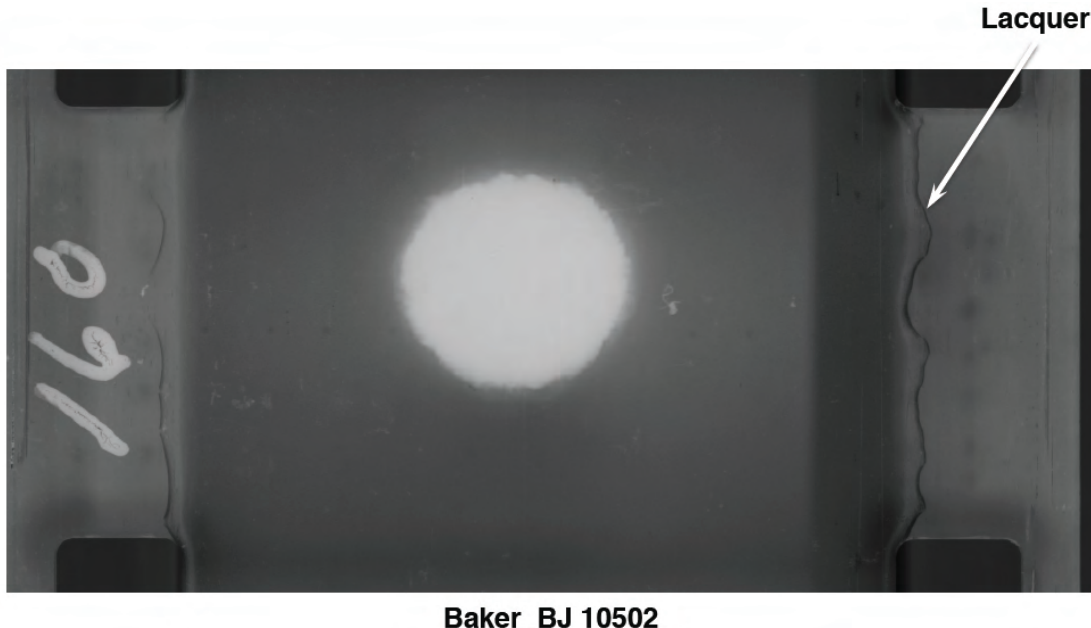


**Figure 9.** A frame of Baker, Buster Jangle with the effects of lacquer still present on the film [11].

Film shrinkage is a large concern for all measurements involving a projective transformation from film coordinates (pixels) to real world coordinates. This can be especially troublesome for structure from motion algorithms that attempt to reconstruct the event in real world coordinates. Many of the EG&G films have shrunk as much as 2.0 percent. In order to project to real world coordinates properly, this shrinkage must be equal in both directions of the film. It can also be taken into account with a modified camera calibration that incorporates a skew coefficient that may have changed over time.

LLNL follows a multitude of steps in order to treat the films prior to film scanning. These steps are [11]:

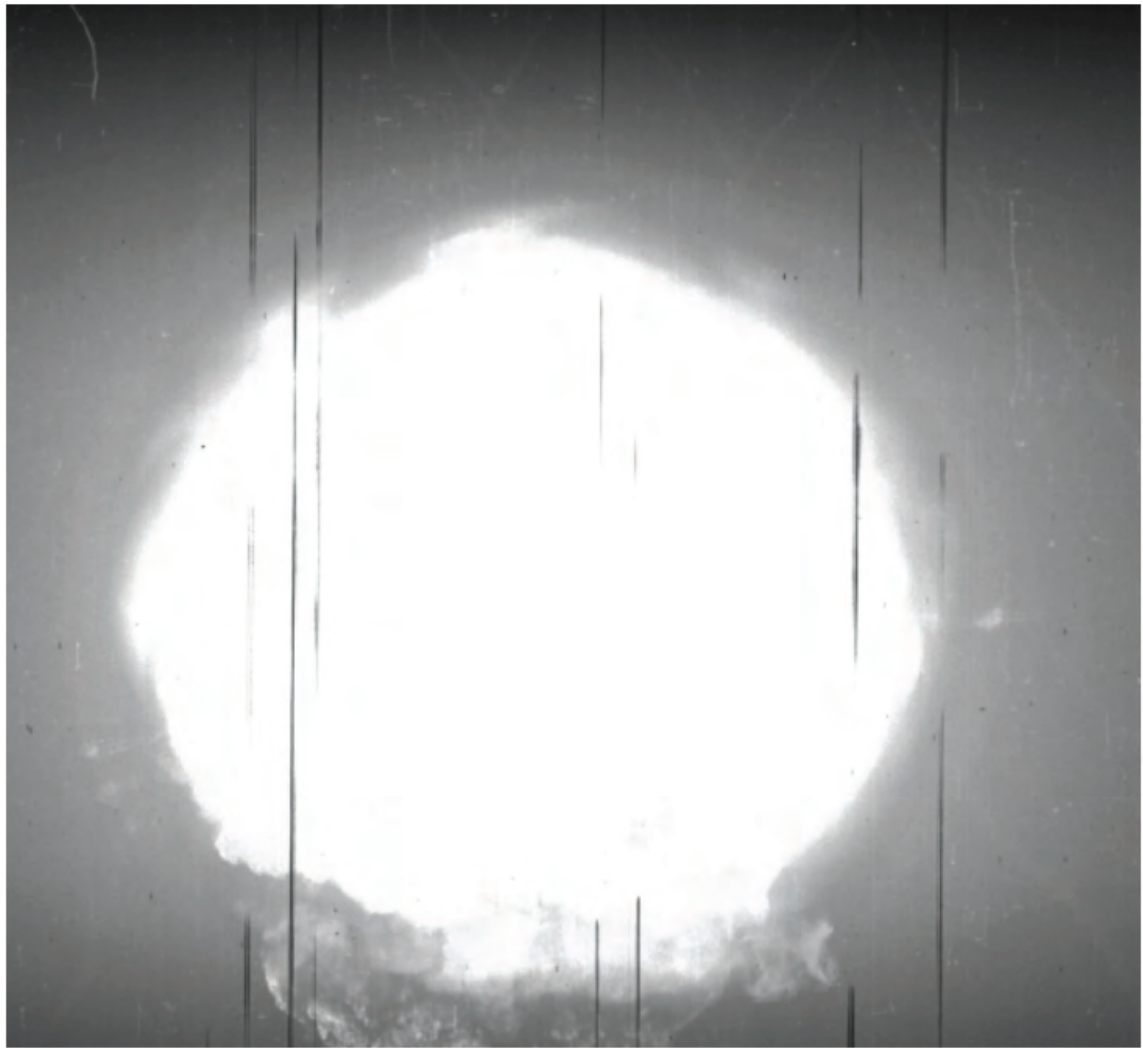


Figure 10. An example of digitized film with scratches [11].

1. Verify that the EG&G perforation number agrees with the information on the film canister
2. Remove any masking tape that may be present
3. Remove EG&G labels that are dried up and falling off
4. Remove small pieces of tape that block the perforations
5. Remove masking tape and/or duct tape splices
6. Redo any tape splices at the head or tail providing data frames and ensure perforation numbers are not lost
7. Look for other splices on the data frames and repair as necessary
8. Look for cracks in the film and repair as necessary
9. Look for broken perforation holes and repair as necessary
10. Splice 7-feet of leader onto the head of film
11. Retain EG&G header labels if possible
12. Splice 7-feet of leader onto the tail end of the film
13. Rewind the film with the base side outward
14. Use the slit in film core to rewind film
15. Replace old cores with new cores as necessary
16. Prior to cleaning any film, the film will be inspected to determine if it is still lacquered.

## 2.5 Film and Rapatronic Plate Dimensions

The nuclear testing films were primarily comprised of 16mm, 35mm and 70mm films, however, not all data was captured by film. Rapatronic plates were used to

captured the earliest times (microseconds) following the nuclear detonation. These plates were used to capture the very earliest of times and were used to derive yields based upon fireball analysis. The rapatronic plates have nominal dimensions of 3.25 by 4.25 inches, but they are not precisely standardized. For consistency, LLNL cropped the area of the flatbed scanner used to scan the rapatronic plates to be precisely  $8.255 \times 10.795$  mm. Rapatronic images correspond to 4 microsecond exposure time, an example of which is shown in Figure 11.

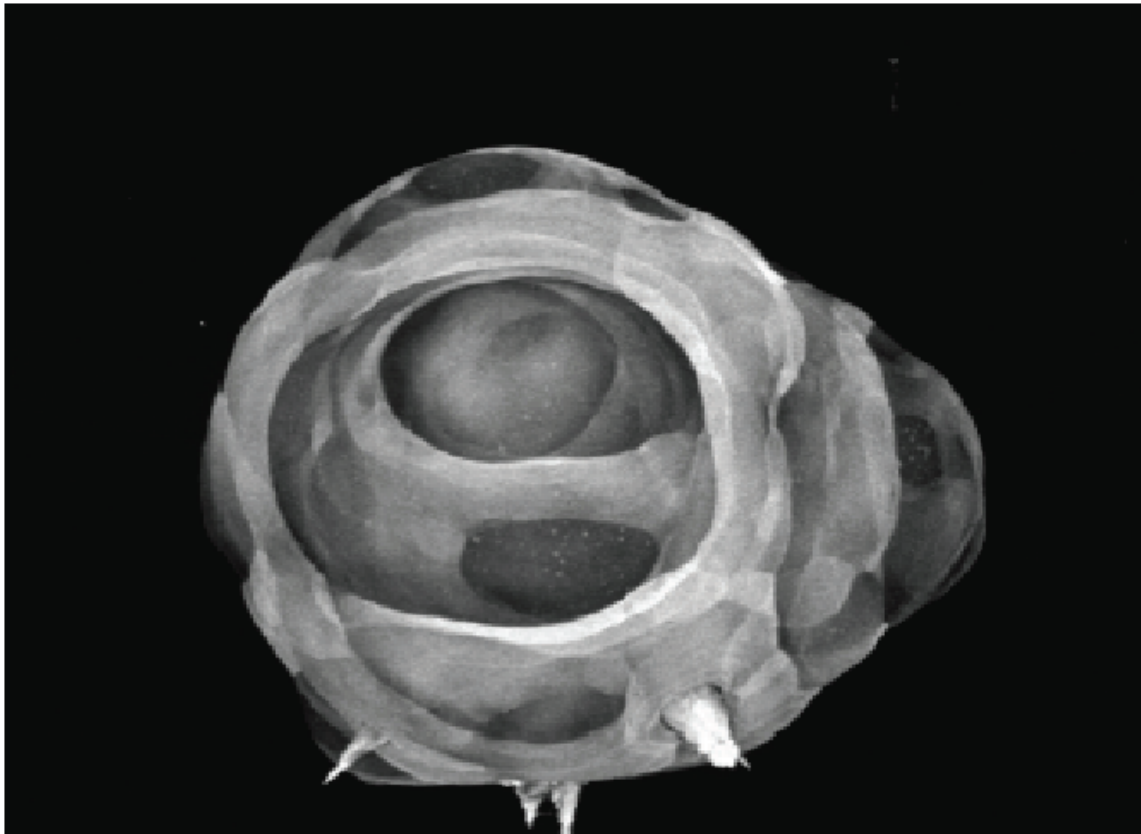


**Figure 11.** Digitized image of rapatronic plate data [11].

Although this work focused predominately on 16 mm fireball films, a number of film types contain data that capture different aspects of the fireball development. In particular the rapatronic plate data overlaps with the fireball film data in observed time, but with a more precise timing resolution.

## 2.6 Digitized Nuclear Testing Film Intensity Variation

Performing two scans of the same nuclear testing film does not result in identical digital copies. Throughout the course of this research, the same film from test shot Easy in Tumbler-Snapper was scanned five separate times in order to improve the understanding of how optical density values vary by scan. Figure 12 shows a comparison of three scans, each separated by less than 30 minutes between scans. This initial comparison looked at the differences in intensity values between each scan relative to another. Scan A compared to scan B, scan A compared to scan C, and scan B compared to scan C. The images were not registered and all pixels within the image were included for analysis. An average pixel intensity difference was determined by the absolute difference of one frame of one scan to that from the other scan. The average pixel intensity difference (as a percent) was determined by taking the average pixel intensity across the original frame.

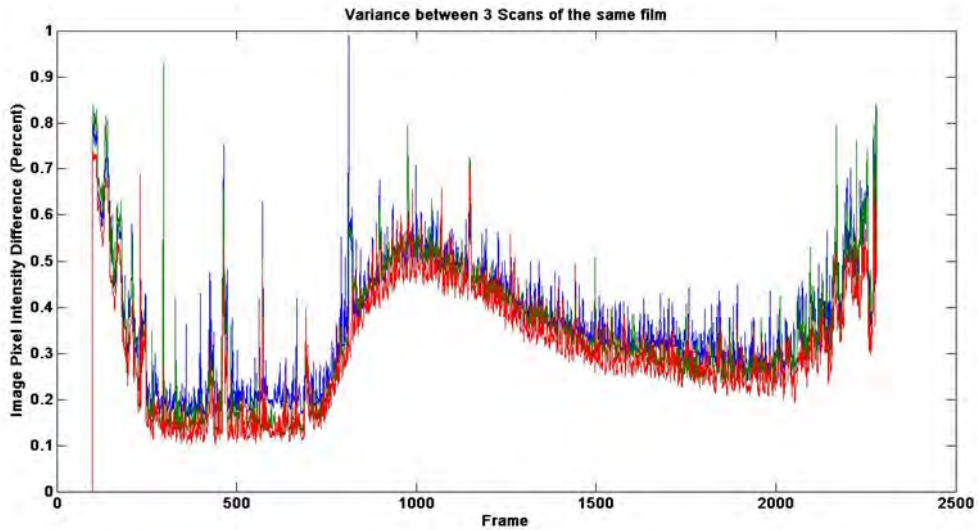


**Figure 12.** This figure shows the pixel intensity difference (percent) for three different scans (red, green, and blue lines) of the same nuclear testing film scanned within minutes of each other.

Figure 12 shows good agreement between the three difference scans. There was

agreement on average amongst the film within 0.5% of the average pixel intensity value across the frame. The average difference in scans changes as the nuclear fireball appears within the frame. As the average pixel intensity of the overall film increases, so does the possibility for a difference scan-to-scan.

What this calculation doesn't address is the average change for the pixel values of interest, or those pixel values that reside in the fireball region. There also appears to be certain frames with significant increases in the differences in pixel intensity readings. These instances were a combination of a physical change in the film itself scan after scan and slight changes in image registration. An example of a physical change from one frame to another is shown in Figure 13.

Figure 13 shows the scan of two identical frames taken 30 minutes apart. The top two images are the two different scans. As shown, a piece of tape smear is present on the top image and not on the middle image. The bottom image highlights the difference between the scans. For this particular frame, it appears as if the initial scan cleaned that portion of the frame, removing it.

Another major difference scan-to-scan was an occasional inconsistency of registration. To better account for registration inconsistencies additional analysis was conducted by first registering each frame from one scan to another. Registration was conducted using Scale Invariant Feature Transform (SIFT) (Section 5.1). Registering the images using SIFT insures that the differences in intensity from one scan to another are not due to a registration issue. Registering the two images also provides the information necessary to quantify the extent to which frames are not aligned scan-to-scan.

Thermal analysis covered in this dissertation was conducted in the region of each frame that defined the fireball. All other regions of each frame were masked out, ensuring that analysis only included the fireball region. To better understanding the

intensity difference scan-to-scan, focusing only on pixels in the fireball region, four scans were compared to each other. The four scans were:

1. The original scan.
2. A scan conducted immediately after the original scan (same day, same bulb).
3. A scan conducted 6 months later using an identical scanner with a different bulb type at it's end of life (6 months apart, aged bulb).
4. A scan conducted 6 months later using an identical scanner with a different bulb type at it's first scan (6 months apart, new bulb).

An example of a difference image between two scans concentrating only on the fireball region is shown in Figure 14. As shown in Figure 14 the difference scan-to-scan appears random, producing an image characteristic of speckled noise. The results of applying this differencing technique, comparing the original scan to three additional scans is shown in Figure 15.

As shown in Figure 15, the variation within the fireball region is on average 0.03 or 3% of the average pixel intensity scan-to-scan. Both scans, conducted 6 months after the original scan, used a different bulb type. Changing the bulb type was shown to have a much more significant effect on the recorded pixel intensities than simply replacing an aged bulb with a new one. Any changes in the scanner or scanning technique should ensure that the conversion between pixel intensity and optical density matches a calibration standard, i.e. Figure 3 should be reproduced.

All work performed for this dissertation used scans conducted within weeks of each other using an identical bulb. Using the results shown in Figure 15 the expected uncertainty in pixel intensity due to differences in scans is approximately 1% on average.

## 2.7 Summary

This chapter provided an introduction to the historical nuclear testing films as well as an introduction to the film scanning process. The film scanning process is conducted by LLNL using a Goldeneye film scanner. Although many issues can be present after the 50+ years these films have been in storage, LLNL has demonstrated the ability to accurately convert digital pixel intensity into optical density.

The film scanning process also has been shown to reliably reproduce pixel intensity values of the same film scanned multiple times. The difference of scans has been shown to be within approximately 1% for scans conducted using an identical bulb type and within 3% for scans using a different bulb type, but identical scanning setup. This chapter provides the introduction of the process, issues, and uncertainties associated with attempting to treat the scanned nuclear testing films like a detector.

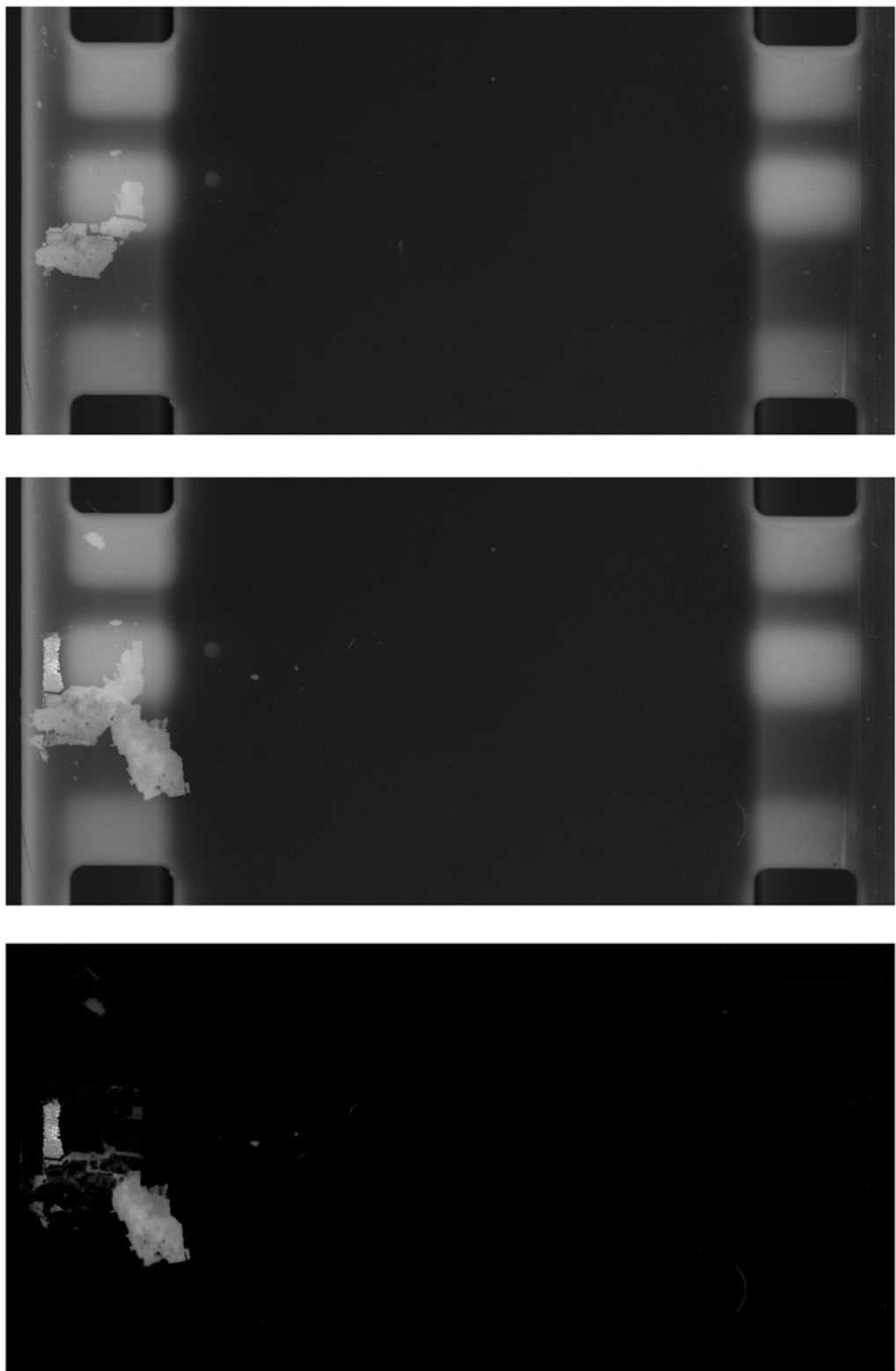


**Figure 13.** Example of two identical frames (top and middle) scanned within 30 minutes of each other. The bottom frame shows the difference in intensity between the two frames.

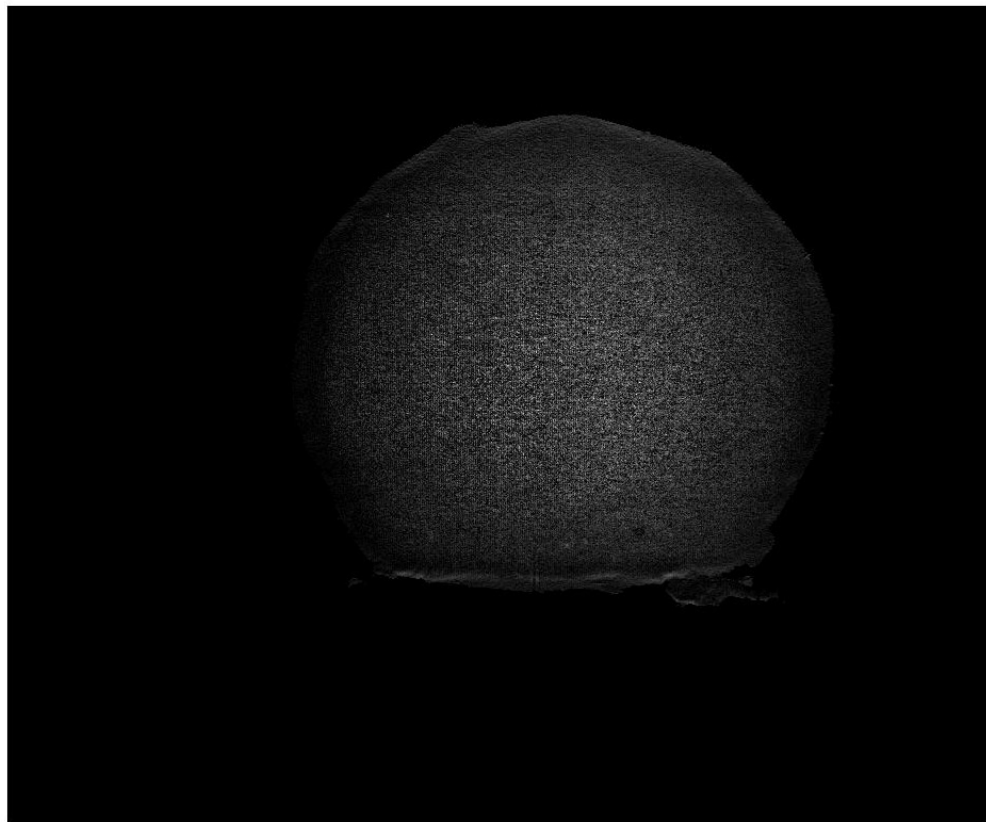
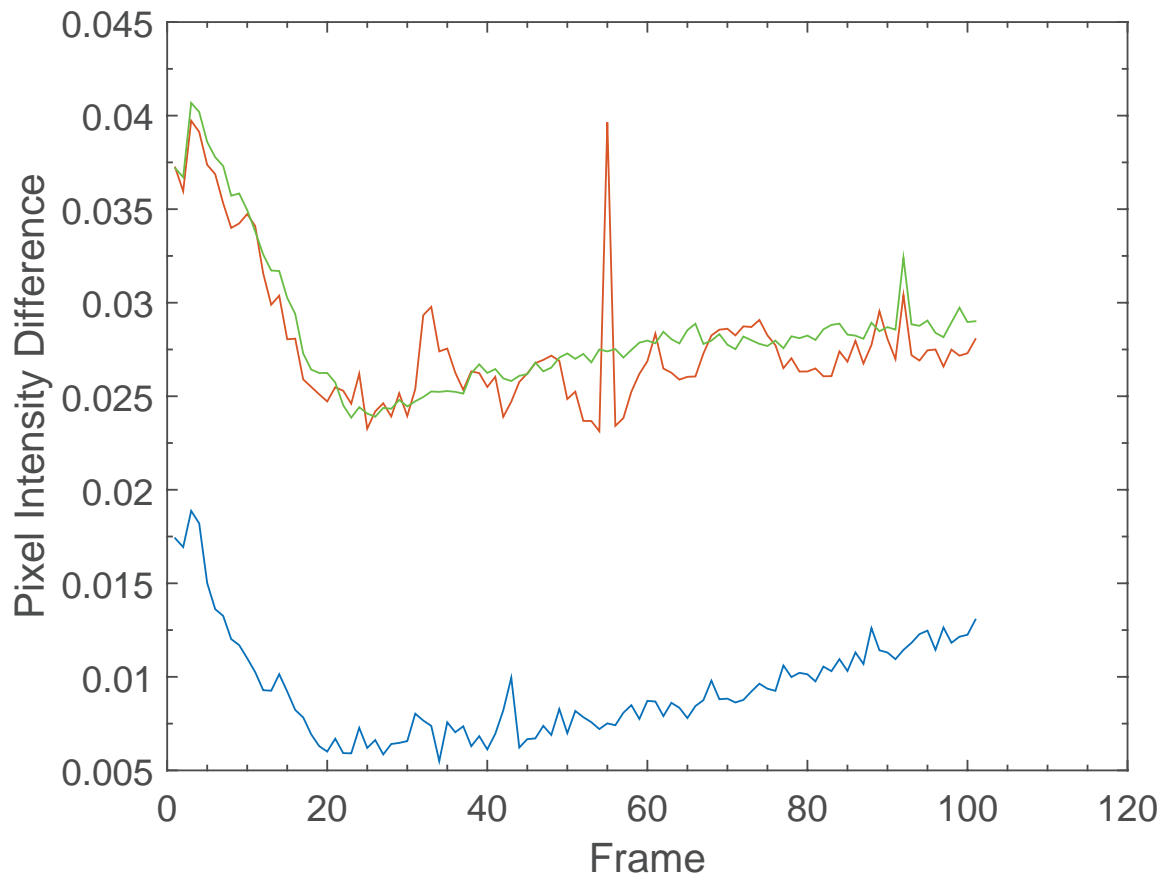


Figure 14. Difference image between two scans, an original and one taken 6 months later.



**Figure 15.** Differences between four separate scans conducted: 30 minutes apart (blue), 6 months apart using an aged bulb (red), and 6 months apart using a newly replaced bulb (green).

### III. 2D Temperature of Nuclear Fireballs

#### 3.1 2D Temperature Introduction

This section outlines the methodology for determining the first 2D apparent temperature of nuclear fireballs using digitized film. Increasing the dimensionality of nuclear fireball data is important for understanding the non-symmetric structure and external interactions of the fireball. Regions of the fireball at higher temperatures expand at a faster rate than cooler regions. Understanding the temperature distribution of both the surface and internal fireball regions can lead to a better understanding of nuclear weapon effects. This is especially true for events that are not spherical in nature and hence have a much wider distribution of fireball temperatures across the surface.

Temperature calculations using digitized film are also important due to the sparse nature of temperature data points collected by calorimeters at the time. This is demonstrated by Figure 16, which shows the results of calorimeters analyzing event Tesla during operation Teapot. A total of seven data points are collected over the course of 0.25 seconds. The data sample rate of film allows for thousands of data points to be collected during this same time interval. This increased time resolution enables improved determination of fireball attributes such as the time and temperature at temperature minimum and maximum, quantities that are used in a variety of nuclear weapon effects codes and models.

The 2D temperature calculation first converted digitized optical densities of the film into an equivalent irradiance interacting with the film. The irradiance of the fireball was then determined by accounting for atmospheric transmission, source output, and geometry. The power temperature was then calculated on a per pixel basis. Events Wasp Prime and Tesla of Operation Teapot were analyzed using this technique.

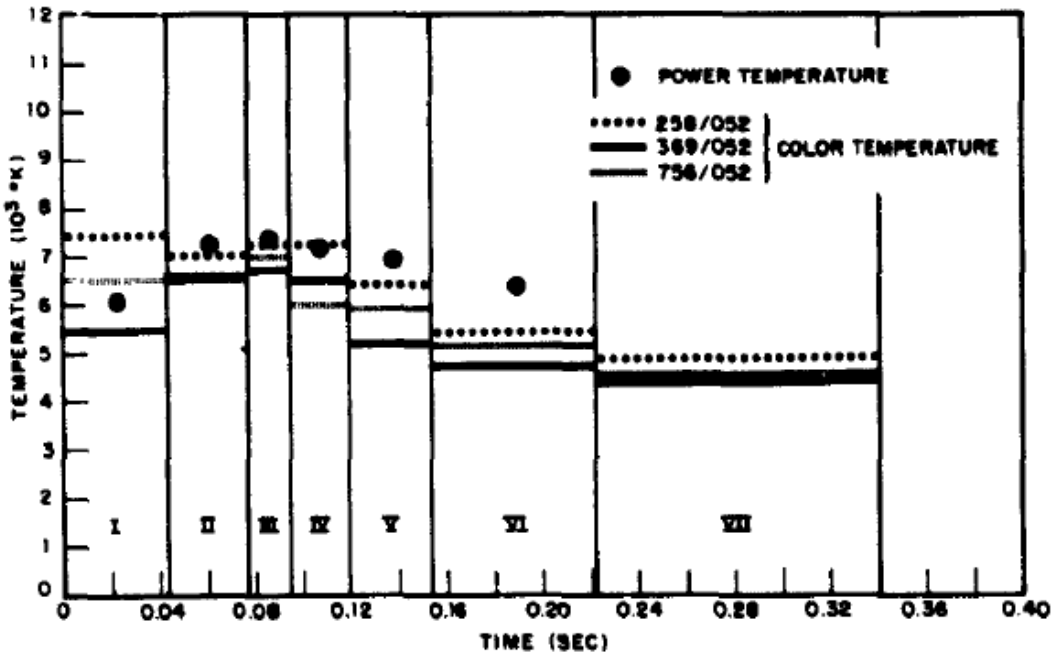


Figure 16. Historical power and color temperature for event Tesla [16].

The film 2D temperature results for each detonation agreed within the uncertainties of the historical calorimeter data. The results were also validated by comparison to a thermal heat flux solution that utilized historical thermal yield values to normalize radiant flux. Additionally, Digital Imaging and Remote Sensing Image Generation (DIRSIG) was used to demonstrate that the 2D temperature calculation was self consistent.

It is important to note that the apparent temperature of a nuclear fireball is dependent upon the wavelength response of the detector and it's look angle to the source. This is because a nuclear fireball is a radiating gas, without a true rigid surface. For example, a detector sensitive to infrared would be capable of observing photons from much deeper into the fireball than a detector sensitive to ultraviolet. The infrared detector would likely therefore record a different apparent temperature. This makes an absolute 2D temperature calculation misleading, in that in order to fully incorporate these effects a 3D temperature calculation is required. In order to

account for this a temperature profile calculation is performed using limb-darkening coefficients in Section 4.2.

### 3.2 Research Methodology

#### Conversion From Digital Counts to Energy.

For thermal analysis, film optical densities are converted to physical units using a HD curve, as discussed in Section 2.3 [17]. An example of an HD curve derived from MF nuclear fireball films is shown in Figure 6. Only the shape of this HD curve is known and not the exact irradiance values themselves. Each step wedge was produced by exposing the film prior to development to known increments of irradiance. However, unless explicitly recorded, the value of the first step wedge relative to a specific irradiance on the film is not known. An assumption to that first irradiance value must be made in order to properly convert from optical density to physical units.

Normally, each film receives four step wedge exposures (two pre-shot and two post-shot) [15]. However, not all nuclear fireball films have these step wedges still intact, i.e. step wedges are no longer present. For many of the films analyzed, the step wedges were removed and therefore analysis requiring an irradiance calculation must use some other approach. For films without step wedges an approximation based on the response of identical film types was developed by Dr. Greg Spriggs at LLNL. For the MF films analyzed in this research effort, a sixth degree polynomial fit was used as the HD curve:

$$\frac{D}{\gamma} = -.00108x^6 + .0017x^5 - .0834x^4 + .071x^3 + .4035x^2 - .0047x + .218, \quad (5)$$

where  $D$  is the optical density of the pixel,  $\gamma$  is the original recorded linear portion of the HD curve value located on the film data sheet, and  $x$  is the energy density of the film in units of  $10^x (\frac{erg}{cm^2})$ . This equation assumes an initial value at  $x = 0$  of  $1 \frac{erg}{cm^2}$ . This assumption appears valid for some films, and has precedence in historical step wedge notes, but is not in general assumed to be exact for every film. Validation steps as outlined in Section 3.4 address the accuracy of this assumption. The approximate energy value at  $x = 0$  has to be determined in order for this methodology to be appropriate.

### **Real World Time Alignment.**

Due to the mechanical nature of film recordings and the technology available at the time, nuclear testing films used highly calibrated timing circuits that flashed timing marks onto films at a precise rate. The high-speed mechanical cameras used during the United States atmospheric nuclear tests had a nominal frame rate of up to 2,500 fps [18]; however, the frame rate could differ by as much as 50% of this nominal value [6, 19]. Timing marks are used to determine accurate frame rates and derived true time within a film series. Timing mark analysis is conducted for each film in order to time align multiple cameras.

### **Power Temperature Derivation.**

For the purposes of this report power temperature is defined as the temperature at which a Planck radiator most accurately matches the radiance observed by film data with an assumed emissivity of 1. The radiance ( $L (\frac{erg}{s-cm^2-str})$ ) of a Planck radiator is given by

$$L = \int_{\lambda_1}^{\lambda_2} \frac{2hc^2}{\lambda^5} \frac{1}{e^{\frac{hc}{\lambda kT}} - 1} d\lambda, \quad (6)$$

where  $h$  is Planck's constant,  $\lambda$  is the wavelength,  $c$  is the speed of light in a vacuum,  $k$  is the Boltzmann constant,  $T$  is the temperature, and  $\lambda_1$  and  $\lambda_2$  are the bounds determined by the wavelength response of the filters, lens, and film type [20].

The irradiance ( $E$  ( $\frac{\text{erg}}{\text{s} \cdot \text{cm}^2}$ )) of the fireball is measured directly from the detector (film) using

$$E = \frac{10^x}{t_{int}}, \quad (7)$$

where  $x$  is the exponent determined from the HD curve (Equation 5),  $t_{int}$  is the integration time of the frame determined by the time separating each frame and accounting for the shutter (prism) angle. The units were chosen for direct comparison to historical documentation, which deal exclusively with energy flux in terms of  $\frac{\text{erg}}{\text{cm}^2}$ . The total power at the detector (film) is determined by multiplying the irradiance by the pixel area ( $A_p$ ),

$$\phi = EA_p. \quad (8)$$

Radiance of the nuclear fireball was then calculated using [21]

$$L = \frac{d^2\phi}{\tau_{atm}R(\lambda)A_{source}A_{lens}}, \quad (9)$$

where  $d$  is the distance from the camera to the source,  $\phi$  is the power on the film,  $A_{source}$  and  $A_{lens}$  are the area of the lens and the area of the source,  $\tau_{atm}$  is the average transmission values of the atmosphere and  $R(\lambda)$  is the relative wavelength response of the filters, lens, and film type [16]. For events Wasp Prime and Tesla a band pass between 520 nm to 700 nm ( $\lambda_1$  and  $\lambda_2$ ) is used based upon the known wavelength response of the W-12 filter (Figure 17) and the MF film [20, 22]. Within this wavelength band the atmospheric transmissions for each of the camera positions

was determined using Moderate Resolution Atmospheric Transmission (MODTRAN) [23] by assuming standard atmospheric temperature and pressure in a dry climate and in the frequency range of interest. This atmospheric transmission changes with distance from detector to source, but in general ranges from 0.9 for camera trailers located to within 3-4 km to 0.6 for camera trailers located at approximately 20 km.

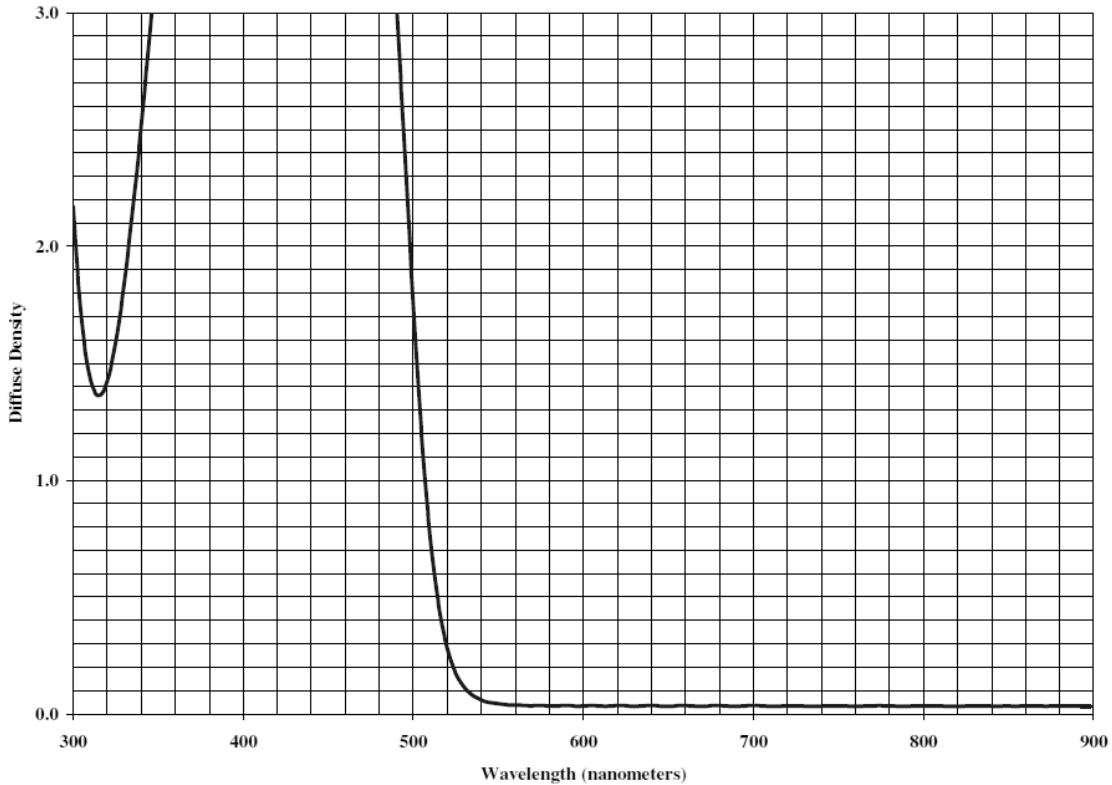


**Figure 17. W-12 yellow filter used on most early time fireball films.**

The Ektar lens responses are assumed to have a flat transmittance across this band pass of 0.75 for all camera configurations [20]. A mechanical rotating prism was used as the camera shutter, and has an assumed transmittance of 0.80 [24]. The prism transmittance value was an approximation that was not quoted within known testing documentation. The product of the rotating prism, lens, and filter transmittance determines  $R(\lambda)$ .

Power temperature was determined by solving for radiance by using Equation 9

and then solving for  $T$  numerically using Equation 6. This was done for every pixel in the fireball region. The region of the film deemed the fireball region is determined by setting a threshold on digital counts within each frame. Each frame is analyzed with an adjusted threshold value to differentiate fireball from non-fireball areas. An example of this threshold is shown in Figure 18.



**Figure 18.** Example of applying an intensity threshold to an image to define the fireball region of a nuclear detonation.

This technique is used to mask the fireball region in order to convert this 2D solution to an average 1D solution for comparison to historical results. In order to determine an appropriate 1D solution, multiple films should be used for analysis. For a single test shot multiple cameras observed the nuclear fireball with nearly identical configurations. In some cases as many as six identical cameras observed the event with the only distinguishable difference in the cameras being the aperture. Having a varying aperture ensures that certain films will be at lower optical density values even during the time at temperature maximum ( $T_{max}$ ). The conversion to  $\frac{\text{watts}}{\text{m}^2}$  from optical density has an increased level of uncertainty at higher optical density levels, and therefore the films with the highest optical densities have the highest uncertainties.

To determine an appropriate weighted mean for each frame an original averaging method is used that weights films according to their average optical density. Films with lower optical density are weighted more highly using a non-linearity factor. The non-linearity factor,  $F$ , is quantitatively defined as an average for the fireball region with an optical density above 2.5 as

$$F = 250 \frac{D}{\gamma} - 625, \quad (10)$$

for a non-linearity factor value of zero at 2.5 optical density and non-linearity factor value of 100 at 2.9 optical density, assuming a  $\gamma$  of 1. Equation 10 is used to weight films with lower average optical densities higher. An optical density value of 2.5 is used as an estimate of where the uncertainty in optical density results in a significant increase in the uncertainty of irradiance. The weighting factor is then taken as the difference between the maximum time aligned saturated camera frame and the camera frame of interest. The sum of the weighting factors is then normalized to 1 using

$$\sum_{camera=1}^{Total cameras} F_{camera} = 1, \quad (11)$$

where the summation runs for the total number of cameras being analyzed and  $F_{camera}$  is the non-linearity factor of a single camera. The weight of each camera was determined from the weighting factor, and is allowed to vary from frame to frame. Figure 19 shows the normalized weighting value for event Wasp Prime for each camera used in analysis of this dissertation.

As shown in Figure 19, at time at temperature minimum ( $T_{min}$ ) each camera is weighted equally because optical density is at a minimum, none of the films have high optical density values, and all of them have equal non-linearity factors. At later times, such as at  $T_{max}$ , certain cameras are weighted more heavily because at these

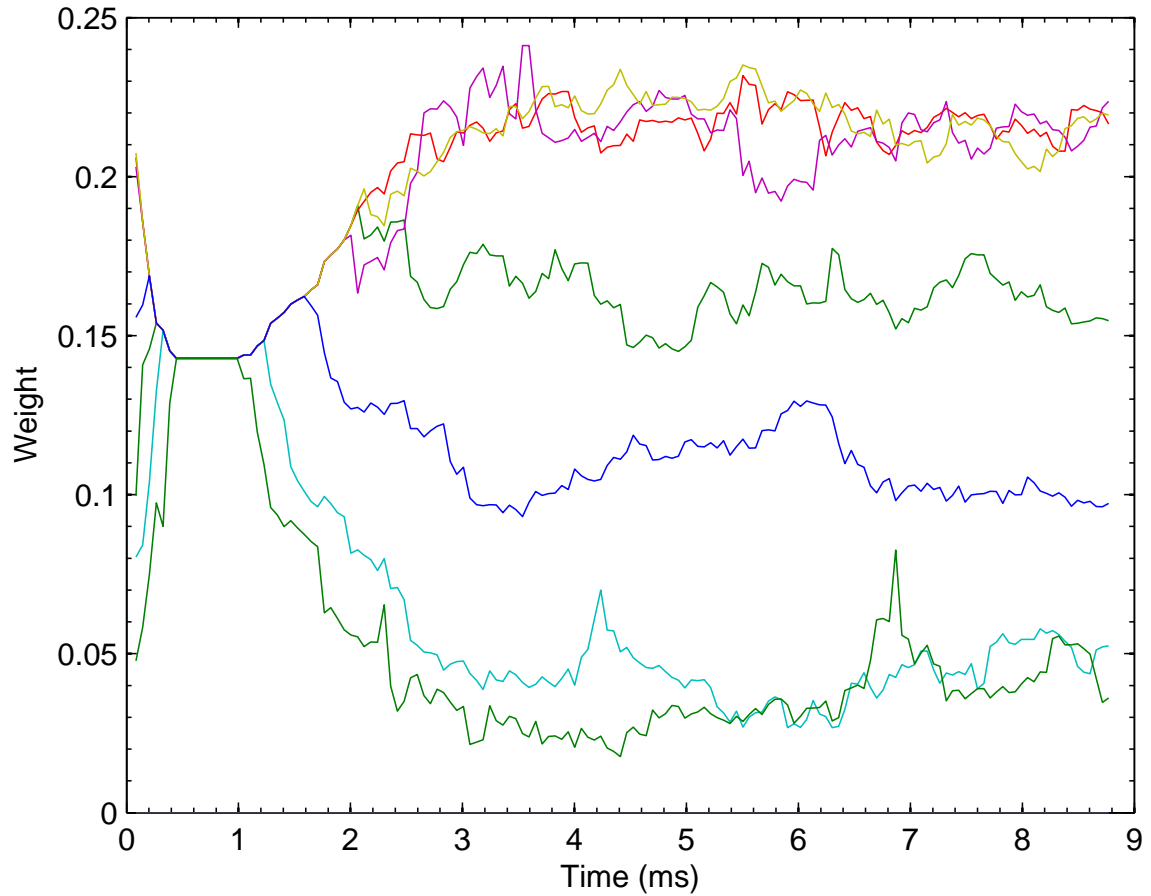


**Figure 19. Weighting function for each of the seven cameras used for analysis.**

higher irradiance levels several of the films have relatively high optical density values. These films have the lowest number of pixels near the top of the HD curve at the high irradiance levels, and hence have the lowest uncertainty in specific intensity.

Another issue in data analysis is over exposure in the film base. Although many times this data will be discarded in a weighted mean based upon the non-linearity factor, there are times when the fireball region itself does not have a high optical density, but the rest of the frame does. This over developed data is suspect and should not be included in thermal analysis. A film is defined as over developed by sampling non-fireball frames or regions to determine if background levels greatly exceed nominal values (0.75 optical density). Over development of particular films

likely was a result of non-standardized film development procedures employed in the rush to get certain films developed soon after the atmospheric tests.

### 3.3 Results

#### Power Temperature Results.

Using the process outlined in the preceding section, 2D temperature was determined for test shots Wasp Prime and Tesla [25]. A mean temperature was then determined as a function of time for each film by averaging all of the films together using the weighting function described in Section 3.2. Figures 20 and 21 show the mean temperatures from film compared to the recorded calorimeter temperatures [16]. 2D temperature plots for  $T_{min}$  and  $T_{max}$  for tests Tesla and Wasp Prime are shown in Figures 22-25.

Uncertainty was determined from the historical calorimeter temperatures to be  $\pm$  15 percent based upon variances in temperature for the same test shot [16]. Uncertainty of the digitized films was estimated to be  $\pm$  15 percent based upon possible changes in the assumed initial value of the HD curve. As shown in Figures 20 and 21, temperature determined using the digitized films agrees within uncertainty to that of the historical calorimeter data as well as demonstrates the behavior of theoretical predictions [26, 2, 3]. In particular, the sharp decrease from initial  $T_{max}$ , presence of a  $T_{min}$  between 3000-5000 K, and a relatively long rise and fall of the second  $T_{max}$ , matches well with these predictions.

#### Thermal Yield Calculation.

Thermal yield values were determined using this 2D temperature solution. The thermal yield of the event was determined using [27]

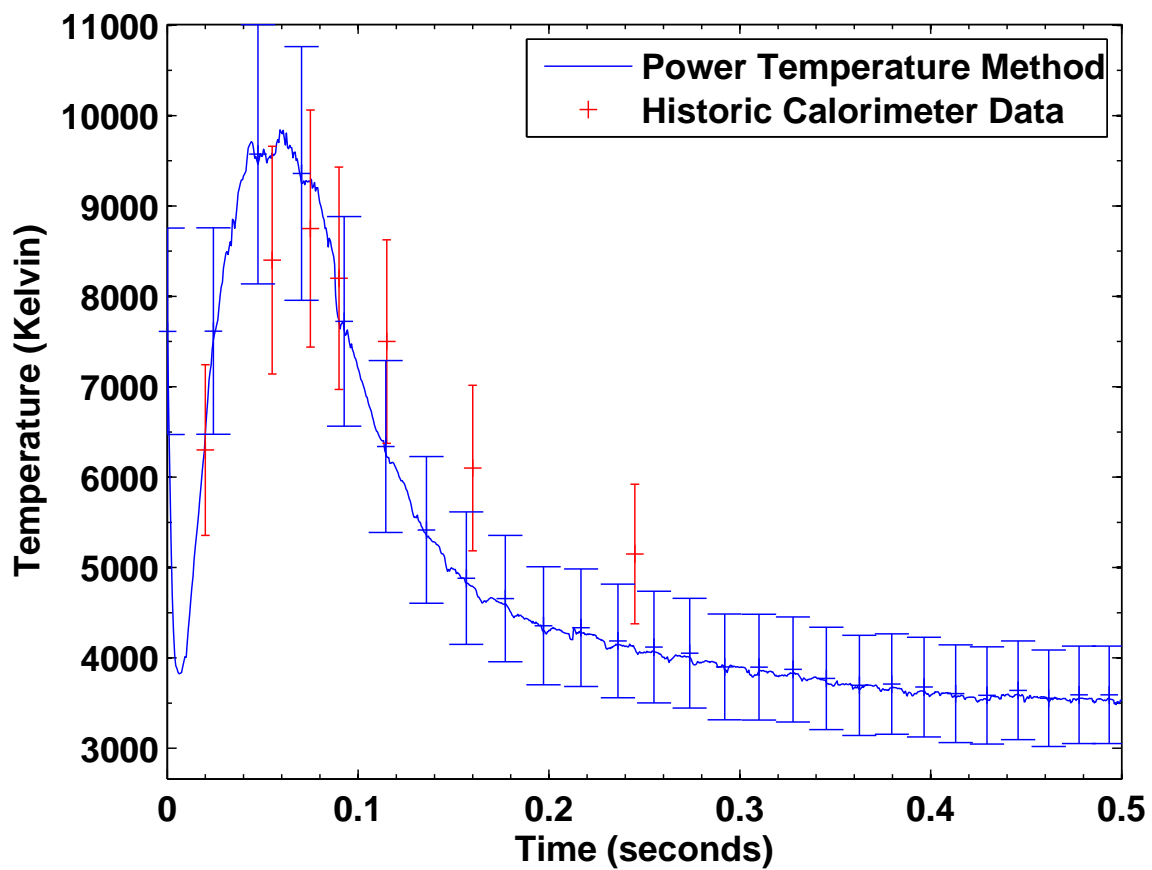


Figure 20. Power temperature for event Wasp Prime.

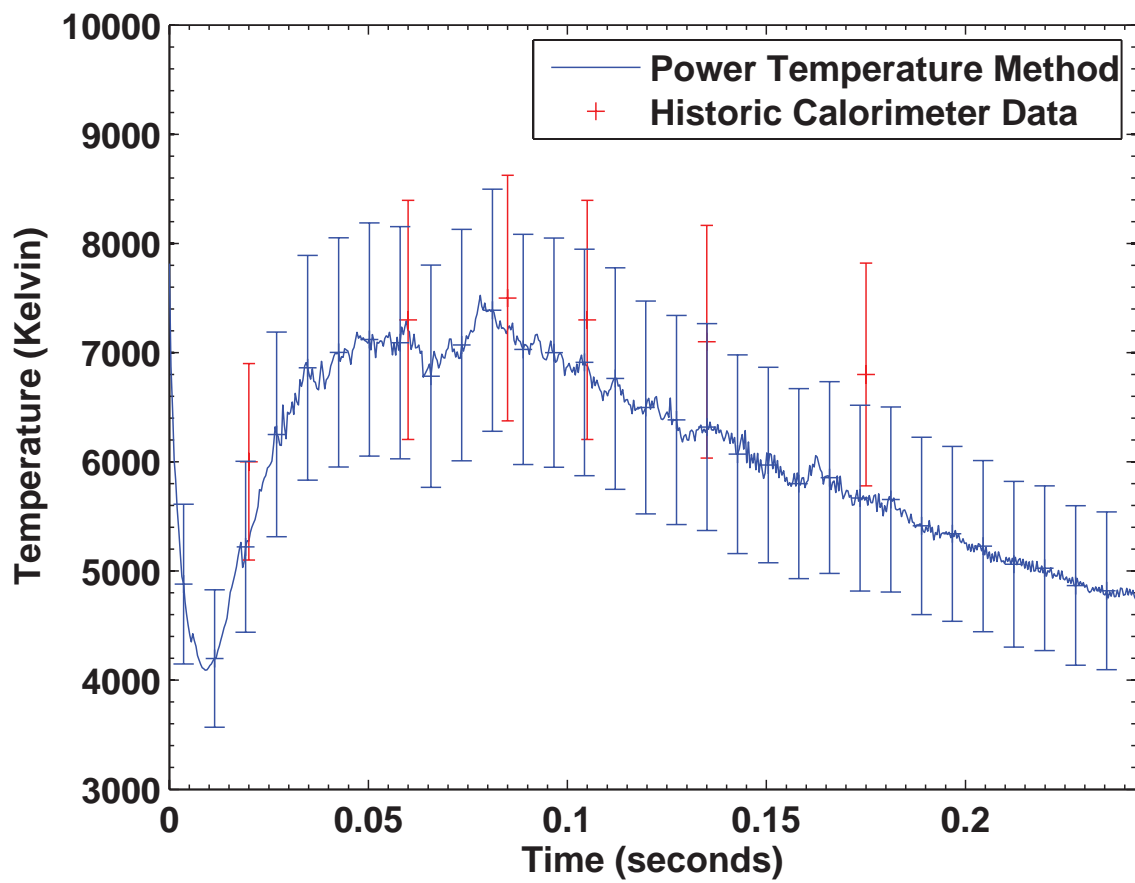


Figure 21. Power temperature for event Tesla.

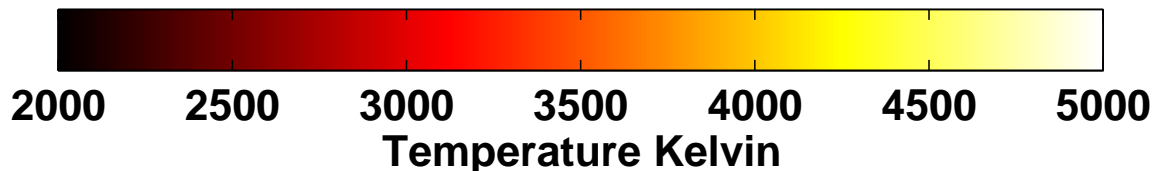
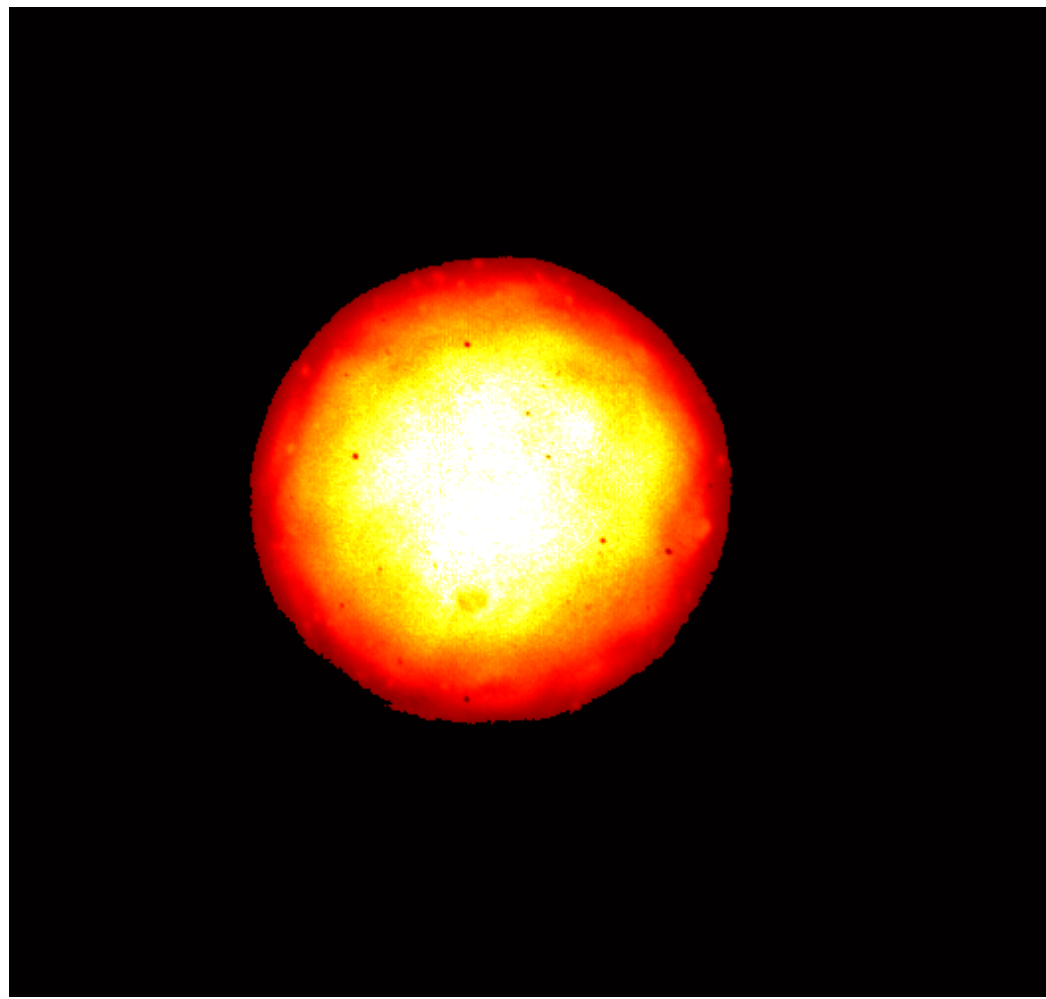


Figure 22. Wasp Prime temperature at  $T_{min}$ .

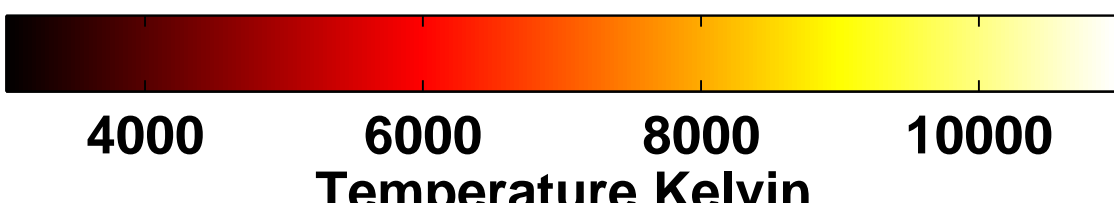
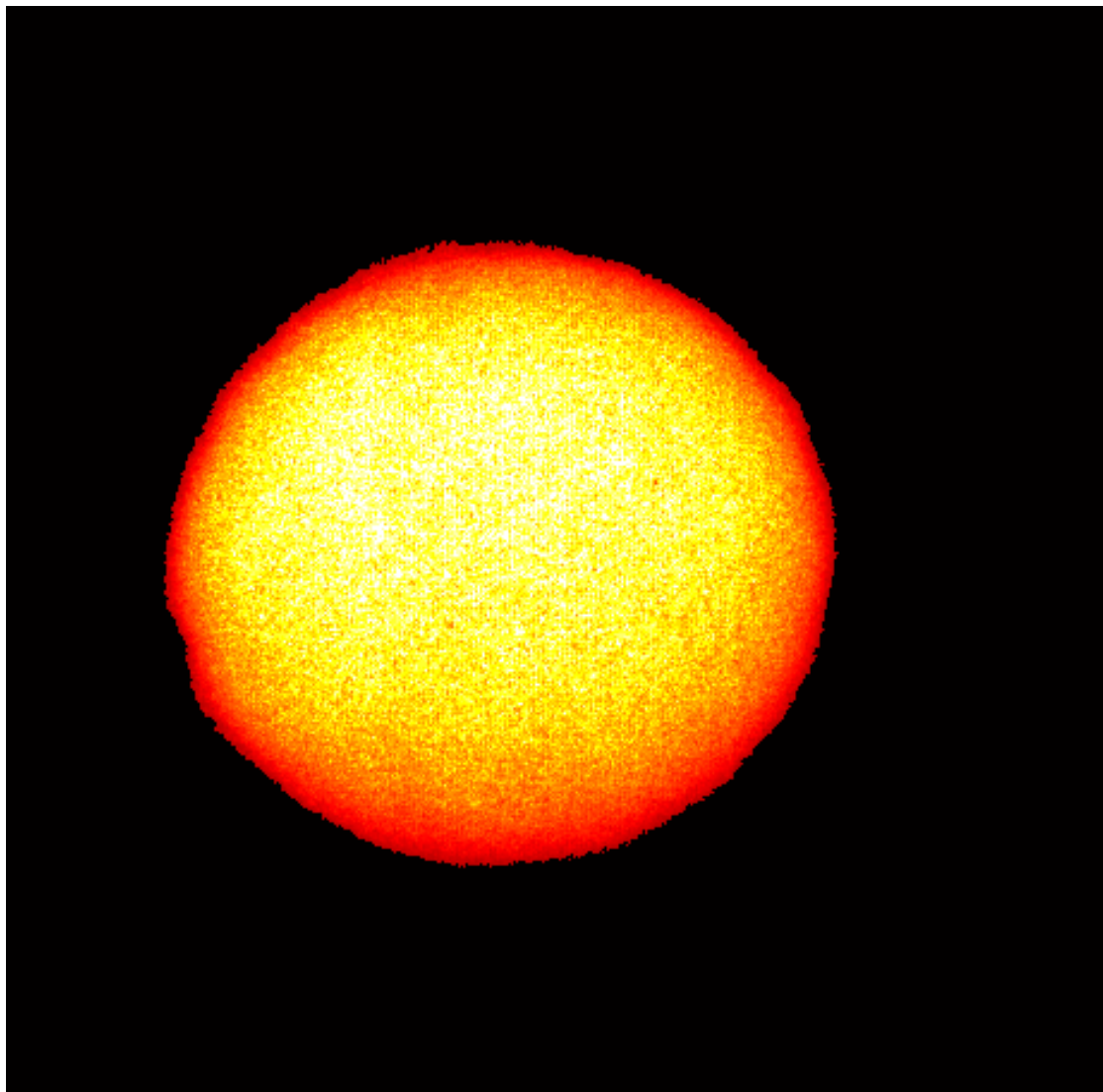


Figure 23. Wasp Prime temperature at  $T_{max}$ .

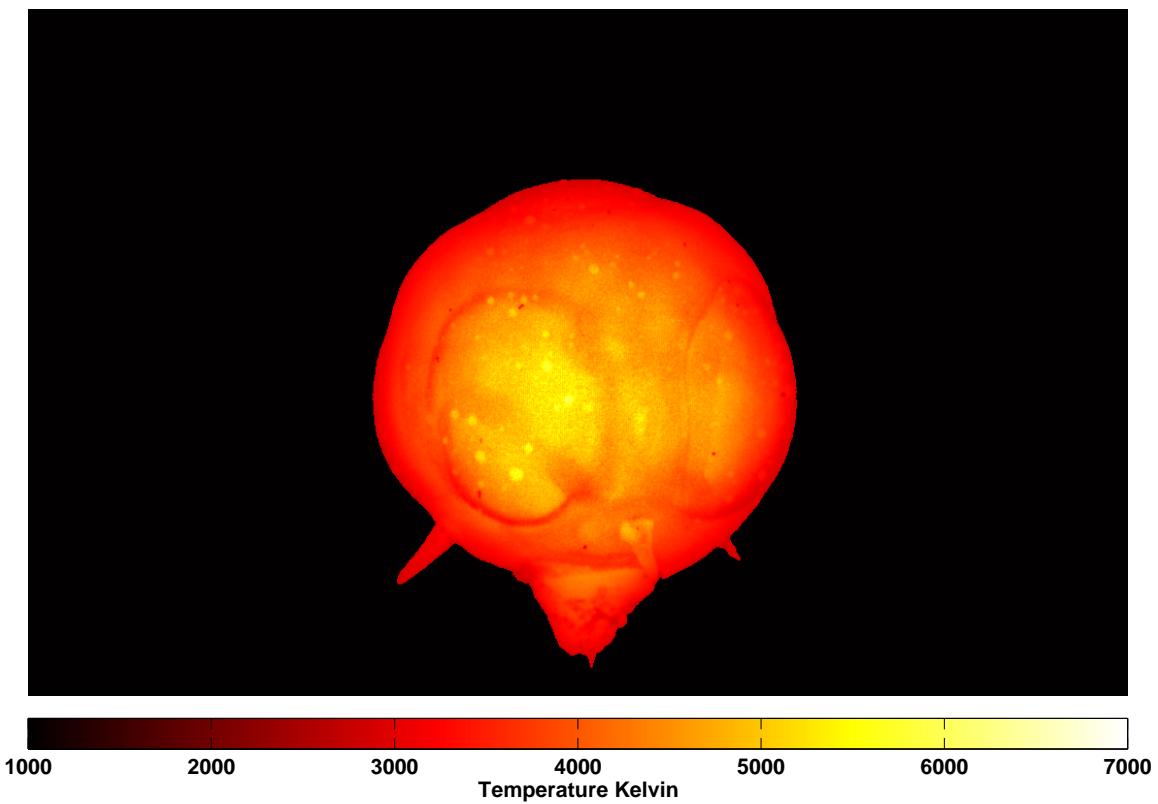


Figure 24. Tesla temperature at  $T_{min}$ .

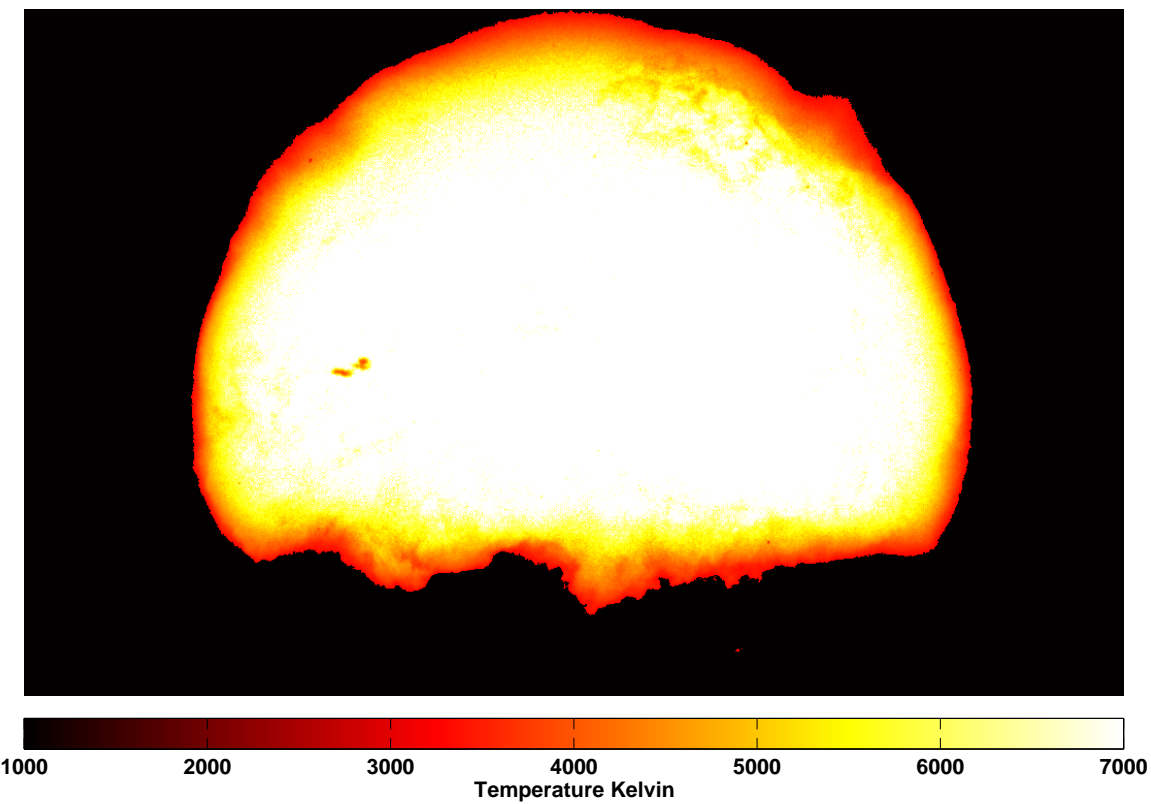


Figure 25. Tesla temperature at  $T_{max}$ .

$$Yield_{Thermal} = \int_0^{\infty} \sigma T^4 4\pi R^2 dt, \quad (12)$$

where  $\sigma$  is the Stefan-Boltzmann constant and  $R$  is the radius determined from the films by assuming the fireball cross sectional area was equal to the total masked pixels averaged across all films. The total radiance across the entire film sequence was expanded at later times assuming that the log linear radiant flux decay was constant after about 0.5 seconds to extend out to 20 seconds, thus ensuring nearly all thermal energy is accounted for.

Utilizing this approach, Wasp Prime was determined to have a thermal yield of  $1.4 \text{ kt} \pm 0.5 \text{ kt}$ . The historical quoted value of the thermal yield of Wasp Prime is  $1.6 \text{ kt}$  [16]. Tesla was determined to have a thermal yield of  $2.6 \text{ kt} \pm 0.75 \text{ kt}$ . The historical quoted thermal yield of Tesla is  $2.5 \text{ kt}$  [16]. Both results agree with historical values and provide further supporting evidence that temperature calculations determined by the 2D power method are consistent with historical data.

### 3.4 Validation and Verification of Results

#### Verification of Results Using DIRSIG.

The 2D temperature algorithm was verified to be self consistent by analyzing results from the Monte Carlo multi-bounce photon model known as the Digital Imaging and Remote Sensing Image Generation Model (DIRSIG) [28]. Photon paths are transmitted from modeled sources, through a generated scene, with atmospheric transmission modeled in MODTRAN [29]. The model accounts for the physical processes which take place during the transport from the source to an electro-optical sensor. This sensor can be modified by the user to emulate detectors used in the real world, such as historical cameras used for atmospheric nuclear testing [30].

A Nevada National Security Site scene was generated within DIRSIG by using elevation data from the US Geological Survey National Elevation Datasheet. This data was sampled over a 5 km by 5 km area of land at the Nevada National Security Site, Site 7, which was the location of the Operation Teapot event Wasp Prime. This surface was then overlaid with a texture map from Google Earth high resolution imagery [30]. This imagery was also used to segment the terrain into similar color sections. These color sections were then used to apply similar material definitions for reflectivity. The reflectance data for these materials was obtained from NASA's Airborne Visual/Infrared Imaging Spectrometer[30]. The results of this scene generation (Figure 26) is a generated image simulating what a modeled historical camera would view (on a logarithmic brightness scale) for one frame at its historical location for Wasp Prime.

Self-consistency was demonstrated by placing the radius from a single camera and power temperature from a single pixel into the DIRSIG model to produce images at every corresponding frame of the film. These images were then analyzed using the power temperature procedure to determine a new temperature solved at each pixel location. The results of this consistency check are shown in Figure 27. The temperature determined from the film analysis results for this camera agrees within uncertainty with the DIRSIG model. The DIRSIG and film data appear to track as a percentage of error relatively consistently throughout the film sequence. There are a few data points near temperature minimum that have better agreement. This is primarily caused by a minimum in uncertainty from DIRSIG at these times. Provided a constant amount of tracked photons, a lower temperature results in better statistics and thus better agreement.

The main purpose of performing this self-consistency check was to ensure that the simple radiometric calculation outlined in Section 3.2 was consistent with a 3D

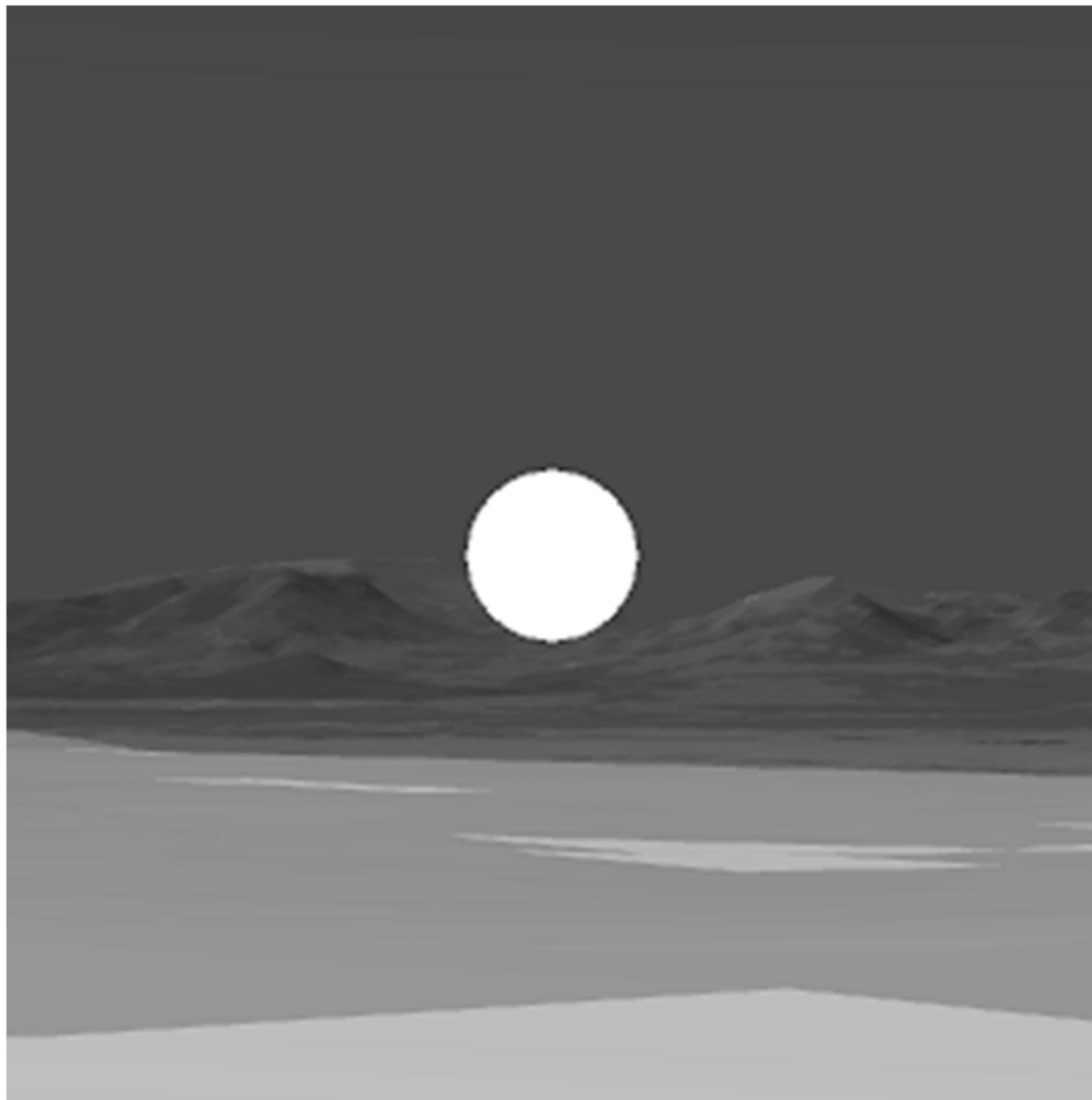


**Figure 26.** Screen capture of Wasp Prime detonation at site 7 Nevada National Security Site as viewed from a historical camera trailer location [30].

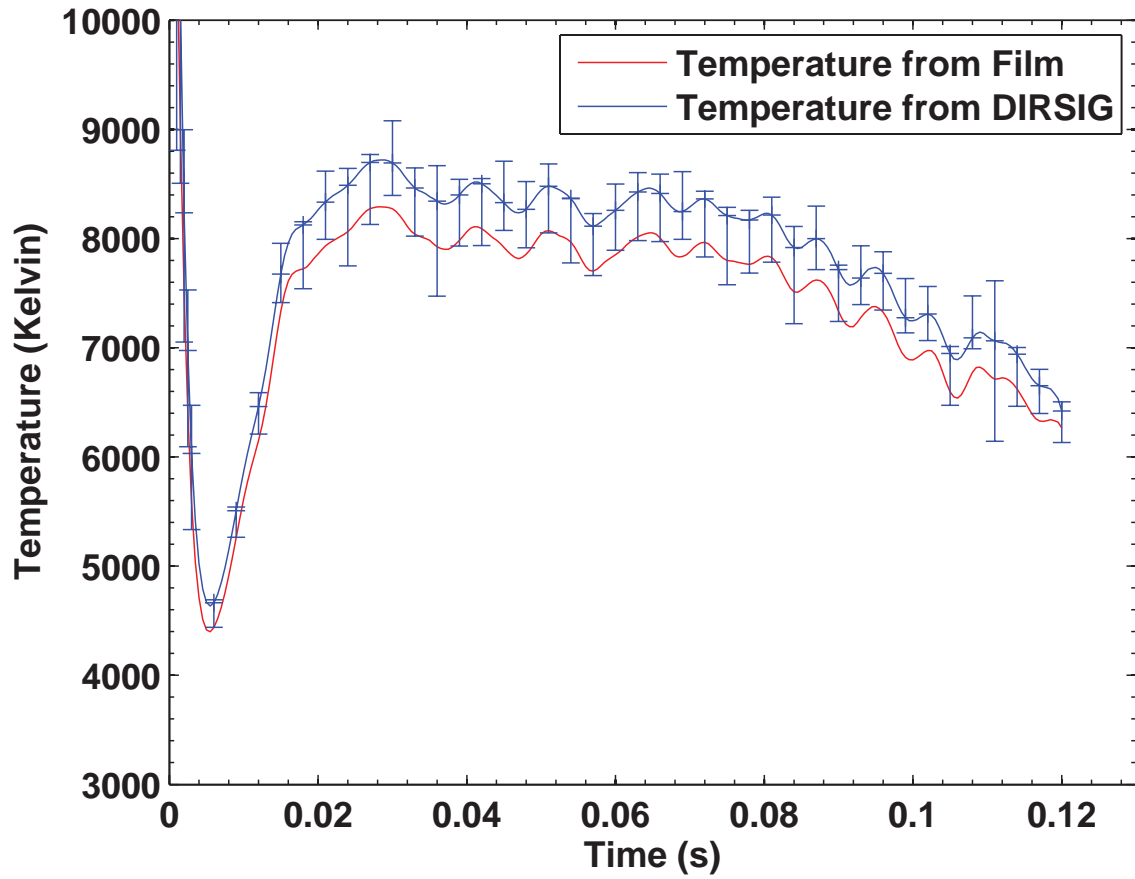


Figure 27. Temperature determined from Wasp Prime single camera and single pixel. The temperature from DIRSIG was determined by generating an image from input in DIRSIG model and re-running the power temperature calculation [30].

multi-bounce Monte Carlo program. A photon traveling from the nuclear fireball to a detector has many possible paths it can follow. Section 3.2 assumes that all photons follow direct paths. This DIRSIG analysis demonstrates that this simplified approach is justified, and consistent with DIRSIG results. However, this analysis does not validate the calculated power temperatures discussed in Section 3.3, which are addressed in the next section.

### Validation of Results Using Heat Flux Method.

Temperature results were also validated based upon a 1D comparison to the heat flux temperature method. The heat flux method determines temperature by measuring the energy transfer of one surface (nuclear fireball) to another (air). The effective time dependent fireball surface temperature can then be determined using [31]

$$T = \left( \frac{Q}{\epsilon \sigma A} + T_{air}^4 \right)^{\frac{1}{4}}, \quad (13)$$

where  $Q$  is the radiant flux (watts),  $\epsilon$  is the emissivity of the radiating body (assumed to be 1 for an effective power temperature),  $\sigma$  is the Stefan-Boltzmann constant, and  $T_{air}$  is the ambient air temperature. The total radiance across the entire film sequence is expanded at later times assuming that the radiance decay slope is constant after about 0.5 seconds to extend out to 20 seconds, thus ensuring nearly all thermal energy is accounted for. This total radiance is then divided by the historical thermal yield value to get a normalized radiant flux value at each data point. Temperature is then solved using this radiant flux value via Equation 13. The radiant flux can be determined by first determining the total radiance within the camera response bandwidth using Equation 5. This calculated radiance can then be scaled appropriately using temperature to determine the total radiance across all wavelengths.

Figure 28 shows the comparison of the heat flux method to that of the mean 2D

power temperature method for event Wasp Prime, demonstrating that the heat flux method and power temperature method are in close agreement.

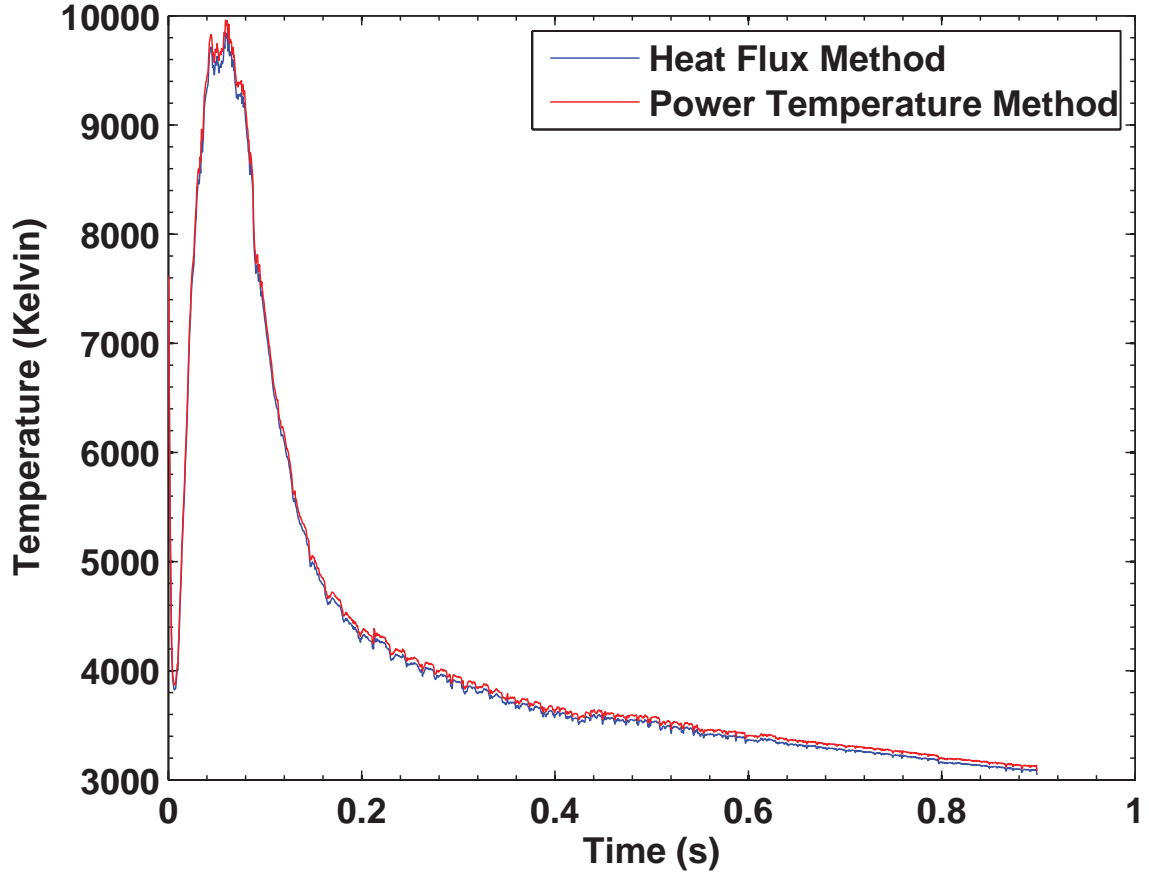


Figure 28. Heat flux method and Power temperature method for Wasp Prime.

### Limitations of Results.

Validation and verification analysis demonstrated that the power temperature derived for the two nuclear testing films investigated in this article are reliable to within  $\pm 15\%$ . The primary limitation in this approach is the inability to derive an original temperature value without a historical reference. Equation 5 was used to derive irradiance values from optical density, however, the energy flux received by the first step in the step wedge is unknown. For this work it was assumed to be  $1 \frac{\text{erg}}{\text{cm}^2}$ . This value was later verified through agreement with the heat flux method,

which relies upon an accurate historical assessment of thermal yield. If this data point was actually  $0.5 \frac{\text{erg}}{\text{cm}^2}$  a significant variance (50 %) between the power and heat flux temperature techniques would exist. Even a slight modification such as using an energy flux of  $0.9 \frac{\text{erg}}{\text{cm}^2}$  results in noticeable differences between the two techniques that should in theory agree exactly. Because of this, the quoted uncertainty of  $\pm 15\%$  was approximated as the maximum possible variance before the validation would fail.

### 3.5 Discussion

Although limitations exist, multidimensional thermal analysis of nuclear events using digitized scientific films has shown the ability to reproduce 2D temperature distributions. This 2D power temperature calculation has been shown to be accurate within  $\pm 15$  percent. Temperature derived from the digitized film agrees with the temperature derived from historical data within these uncertainties. Temperature results were verified to be self consistent using DIRSIG and validated through comparison with a 1D heat flux solution. Temperature results were then used to derive a thermal yield value, which agreed within  $\pm 10\%$  of the historically accepted values. These uncertainties are quoted at higher values than historical data, predominately because historical analysis did not account for differences in measurement due to multidimensional effects. For example, one technique used to calculate temperature at the time was to use what was referred to as color temperature, where data was collected by two different calorimeters with different color filters. The ratio of the irradiance between these two filters was then used to calculate temperature, this was referred to as the color temperature method. For a Lambertian source (Section 4.1), this technique is valid. Results for Wasp Prime that compare the power temperature to color temperature are shown in Figure 29.

As shown in Figure 29, the color temperature and power temperature do not agree.

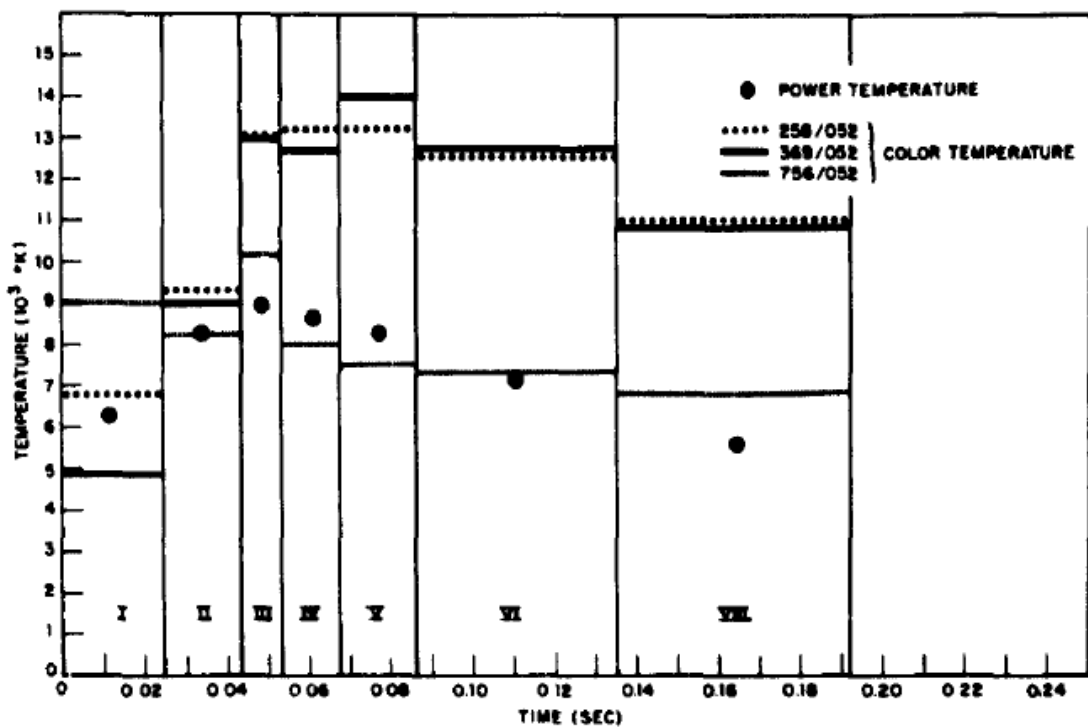


Figure 29. Historical results of Wasp Prime temperature data[16].

The suspected reason is that the different color filters used for analysis actually are viewing photons coming from different regions in the fireball, thus skewing the comparison. Because a nuclear fireball is a radiating gas it is not Lambertian, therefore performing a color temperature calculation in this manner is not appropriate. This complication is further discussed in Chapters IV and V.

## IV. Limb-Darkening Analysis of Nuclear Detonations

### 4.1 Limb-Darkening Laws

#### Introduction.

Limb-darkening is the term that refers to the decrease in apparent irradiance and temperature near the outer regions of an imaged source, generally a star. Limb-darkening effects are important when performing thermal analysis of nuclear fireballs. For example, any temperature analysis using the pixel intensity will be greatly influenced by limb-darkening, because like the sun, a nuclear fireball is not a Lambertian source.

A Lambertian source, an ideal blackbody emitter, is defined as a source that adheres to Lambert's emission law, which states that the radiant intensity observed is directly proportional to the cosine of the angle between the observer's line of sight and the surface normal. As a consequence of Lambert's Law, if such a surface is viewed from any angle, the source has a constant apparent radiance or brightness. Although the radiant power from a source region follows a cosine roll-off, the projected area is increased by an amount that compensates. Therefore, for a Lambertian source, the observed brightness is independent of look angle. As can be seen in the Figure 30, there is not a constant apparent radiance for a nuclear detonation, but an intensity roll-off or limb-darkening. This effect will cause all thermal analysis results to skew to lower values than what they would be otherwise without limb-darkening.

Radiation received from a sensor can be approximated as the total amount of all emission along one optical path length. Along the edges of an image, this optical path length does not reach as far into the source as it does at low look angles, as shown in Figure 31.

From a small look angle, photons from more interior regions of the sun can reach

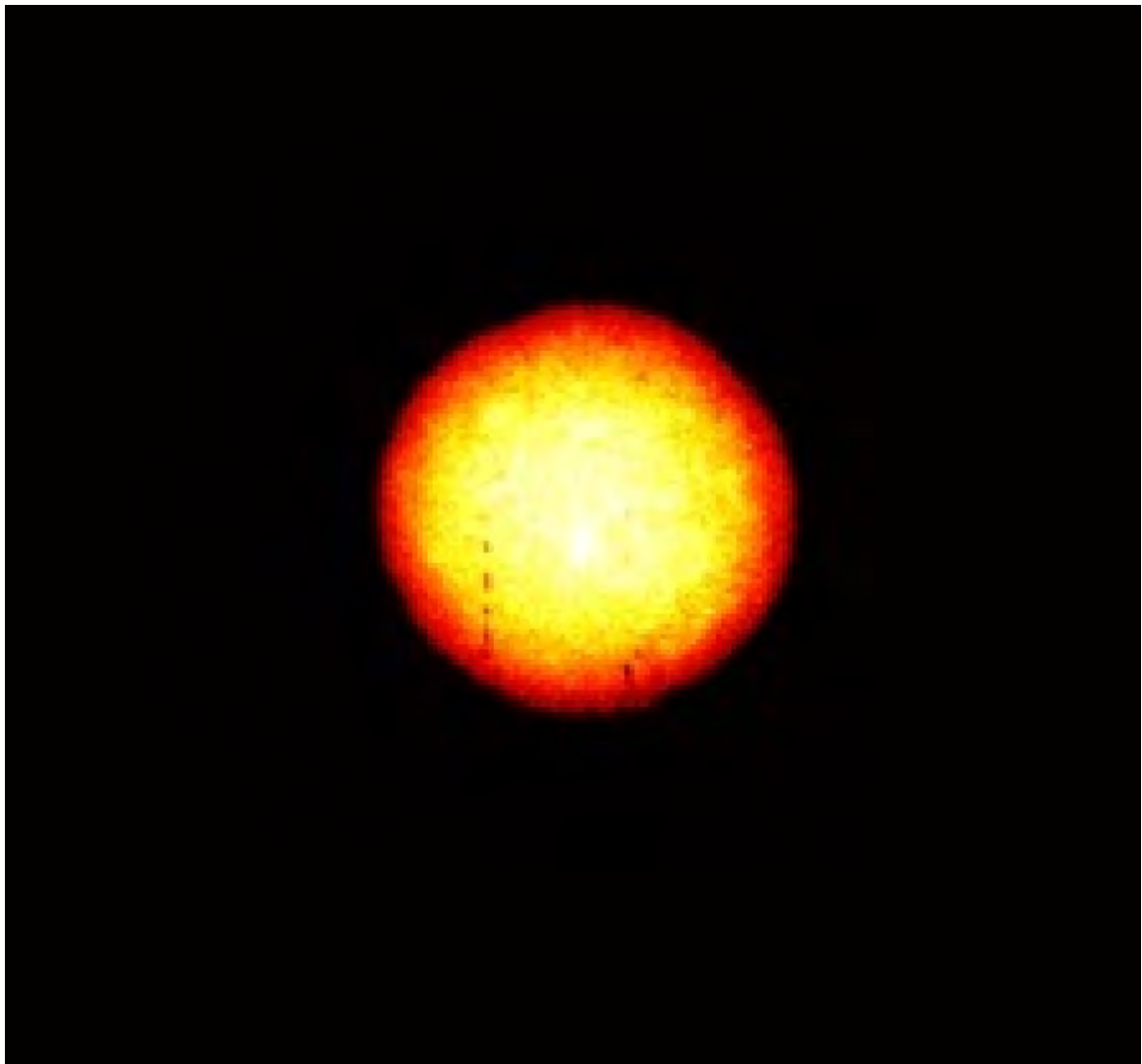


Figure 30. Non-Lambertian limb-darkening effects for event Wasp Prime. The outer edges appear cooler (red) while the center appears hotter (white). A Lambertian source would appear uniform in brightness to an observer.

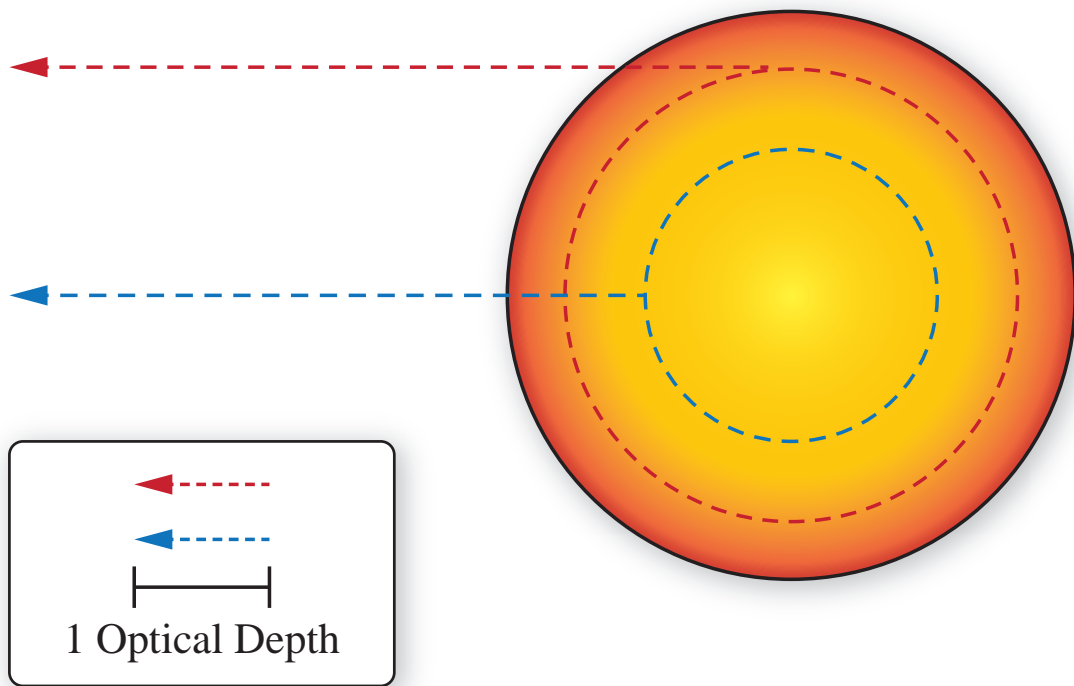


Figure 31. This figure highlights the physical reason behind observed limb-darkening. For a constant optical depth, photons from the center of a radiating object come from a deeper region of the fireball. Photons from outer regions cannot escape unless they are closer to the surface. The photons from the interior region come from a point that is hotter and likely more dense. The outer region is nominally not as hot and has lower density. For a captured image of this source, the outer regions of the spherical object would appear less intense, or demonstrate limb-darkening.

the observer. For a constant mean free path and a fixed observer, higher look angles (edges of image), will not allow photons from that interior region to escape. The photons that do escape are from a more external region. For stars this external region is considered to be as less dense and as having a lower temperature. This reduction in density and temperature results in an observed limb-darkening effect. This limb-darkening effect can also be observed for nuclear fireballs [3]. Figure 30 highlights this effect using an artificial color scale for Wasp Prime.

As can be seen in Figure 30, the outer edges of the fireball are red, signifying lower intensity regions. The inner regions of the fireball are bright yellow or white, signifying a higher intensity. The intensity roll-off is source and frequency dependent, and can be expressed as

$$\frac{I(\theta)}{I(1)} = \sum_{k=0}^N a_k \cos^k(\theta), \quad (14)$$

where  $I$  is an array of the pixel intensity values of the image and the sum of all  $a_k = 1$ . The geometry detailing the relationship of  $\theta$  is shown in Figure 32. Due to the non-Lambertian nature of a nuclear explosion, much of the temperature results derived from historical measurements is fundamentally flawed in many cases and this helps explain the lack of consistency across reported measurements [16, 32, 33, 34, 35, 36]. This is particularly true for color temperature results where data was collected by two different calorimeters with different color filters. The ratio of the irradiance between these two filters was then used to calculate color temperature. The fundamental issue is that using two different filters ensures that the two detectors are averaging their irradiance across different optical depths within the fireball. Because of this, the two detectors would record a different power temperature and therefore have obfuscated irradiance ratios.

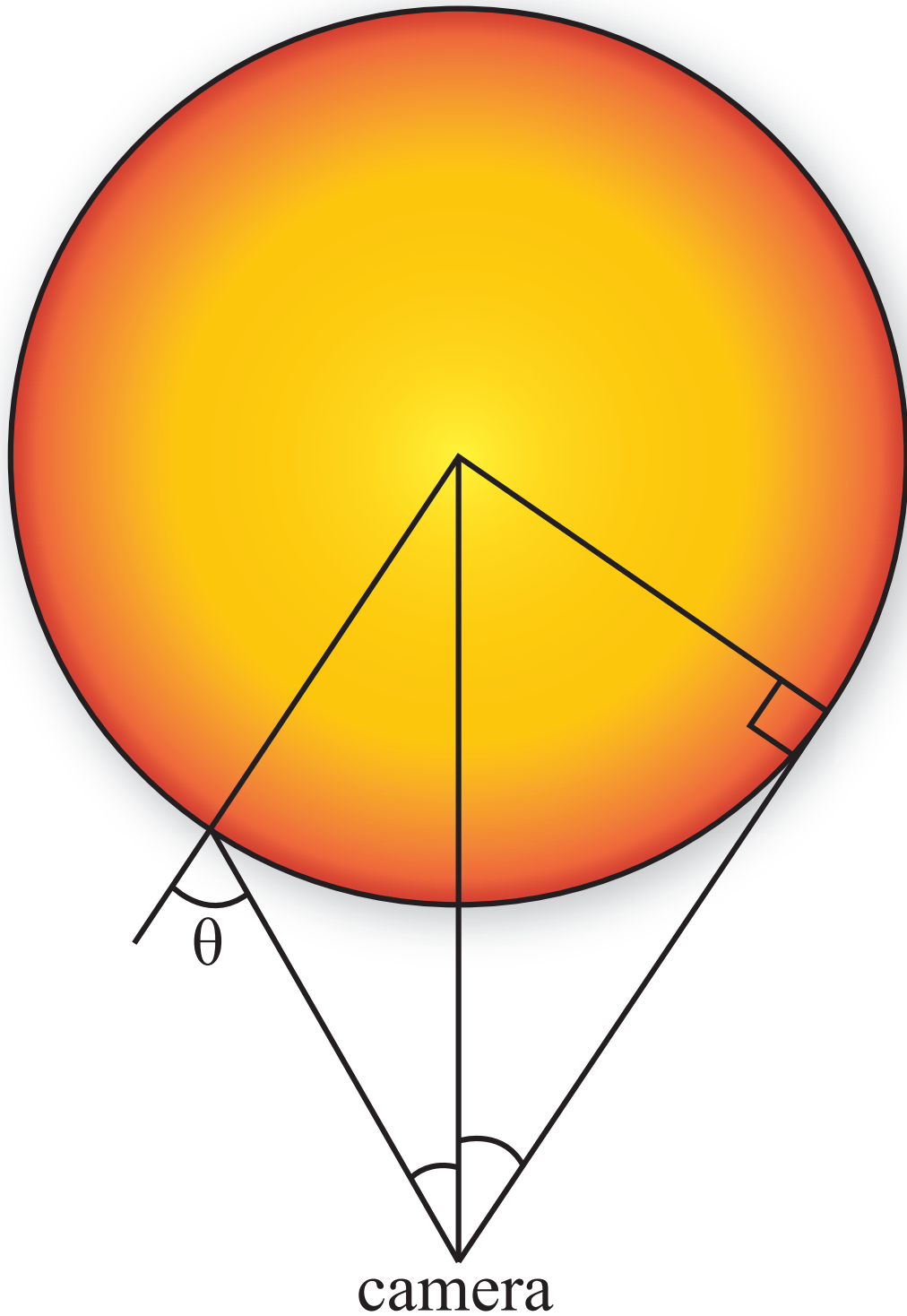


Figure 32. The coordinate system used when determining limb-darkening coefficients.

## Limb-Darkening Laws Overview.

There are several limb-darkening laws discussed in literature, seven of which were chosen for this research [37, 38, 39, 40, 41, 42, 43]. These seven different limb-darkening laws were considered based upon a variety of current literature, which use all or a combination of these laws for analysis of stars [44, 45, 46].

The limb-darkening laws used for this analysis are

$$\frac{I(\mu)}{I(1)} = 1 - a(1 - \mu) \quad (15)$$

$$\frac{I(\mu)}{I(1)} = 1 - b(1 - \mu) - c(1 - \mu)^2 \quad (16)$$

$$\frac{I(\mu)}{I(1)} = 1 - d(1 - \mu) - f(1 - \mu^{\frac{1}{2}}) \quad (17)$$

$$\frac{I(\mu)}{I(1)} = 1 - g(1 - \mu) - h(\mu \ln \mu) \quad (18)$$

$$\frac{I(\mu)}{I(1)} = 1 - j(1 - \mu) - \frac{k}{1 - e^{\mu}} \quad (19)$$

$$\frac{I(\mu)}{I(1)} = 1 - l(1 - \mu) - m(1 - \mu^{\frac{3}{2}}) - n(1 - \mu^2) \quad (20)$$

$$\frac{I(\mu)}{I(1)} = 1 - p(1 - \mu^{\frac{1}{2}}) - q(1 - \mu) - r(1 - \mu^{\frac{3}{2}}) - s(1 - \mu^2), \quad (21)$$

where  $I(1)$  represents the specific intensity at the center of the fireball,  $\mu = \cos\theta$ ,  $\theta$  is the angle shown in Figure 32, and  $a, b, c, d, f, g, h, j, k, l, m, n, p, q, r$ , and  $s$  are the limb-darkening coefficients.

Equation 15 is the linear limb-darkening law first proposed by Russell and Shapley in 1912 [37]. This is the only limb-darkening law considered with only one coefficient. Nonlinear laws tend to reproduce the intensity profile of stellar objects better than a linear limb-darkening law. Equations 16-18 are the quadratic [38], square-root [39], and logarithmic [42] limb-darkening laws. Equation 20 and 21 are the three-parameter and four-parameter limb-darkening laws [40, 41]. The four-parameter law is merely an extension of the three-parameter law by adding an additional parameter.

One way to compare limb-darkening laws is to investigate the resultant temperature or intensity profiles. The specific intensity of an emitting body can be determined by [47]

$$\frac{I(\mu)}{I(1)} = \frac{1}{\mu} \int_0^\infty S(\tau) e^{-\tau/\mu} d\tau = \frac{1}{\mu} L[S(\tau)], \quad (22)$$

where  $\tau$  is the optical path length and  $L[S(\tau)]$  is the Lorentz transformation of the source function. The source function can be approximated as

$$S(\tau) = I(1) \left( a_o + a_{\frac{1}{2}} \sqrt{\tau} + a_1 \tau + a_{\frac{3}{2}} \tau^{\frac{3}{2}} + a_2 \tau^2 + a_{\ln} \tau \ln(\tau) + a_3 \tau^3 \right). \quad (23)$$

This particular source function was chosen because it can be directly related to the limb-darkening laws (Equations 15-21). It is a modification to the Maclaurin series source function, but with additional coefficients that allow for analytical solutions to intensity profiles. The normalized specific intensity that corresponds to this source function is

$$\begin{aligned} \frac{I(\mu)}{I(1)} = a_o + a_{\frac{1}{2}} \frac{\sqrt{\pi}}{2} \mu^{\frac{1}{2}} + a_1 \mu + \frac{3}{4} a_{\frac{3}{2}} \sqrt{\pi} \mu^{\frac{3}{2}} \\ + 2a_2 \mu^2 + a_{\ln} \mu (1 - \gamma + \ln(\mu)) + 6a_3 \mu^3. \end{aligned} \quad (24)$$

This normalized specific intensity can then be compared to the limb-darkening laws (Equations 15-21) in order to relate limb-darkening coefficients to a specific intensity source function. Table 2 shows this mapping of variables. An effective temperature profile can then be determined using the known specific intensity at the center of the nuclear fireball and assuming a Plank frequency distribution.

**Table 2. Temperature Profile for Various Limb-Darkening Laws**

Eq No.	$a_o$	$a_{\frac{1}{2}}$	$a_1$	$a_{\frac{3}{2}}$	$a_2$	$a_{ln}$	$a_3$
Eq 15	1-a	0	a	0	0	0	0
Eq 16	1-c-b	0	$2c+b$	0	$-\frac{1}{2}c$	0	0
Eq 17	1-d-f	$\frac{2}{\sqrt{\pi}}f$	d	0	0	0	0
Eq 18	1-g	0	$g-h+h\gamma$	0	0	h	0
Eq 19	$1-j+\frac{k}{2}$	$j+\frac{k}{2}$	0	0	0	0	$-\frac{1}{6}k$
Eq 20	1-l-m-n	0	1	$\frac{4m}{3\sqrt{\pi}}$	$\frac{1}{2}n$	0	0
Eq 21	1-p-q-r-s	$\frac{2p}{\sqrt{\pi}}$	q	$\frac{4r}{3\sqrt{\pi}}$	$\frac{s}{2}$	0	0

### Film Analysis.

A total of seven films were analyzed for event Wasp Prime. Wasp Prime, a free air detonation, was chosen for analysis because surface interacting events, for which films are also available, produce significant deformations in the fireball that make limb-darkening analysis more difficult. The film data sheets provided the distance to detonation, weather conditions, film type, lens type, aperture size, types of optical filters used, and shutter angles [48]. For all films analyzed a W-12 (yellow) filter was used (Figure 17)[22]. The wavelength bandwidth of the entire camera system was determined to be 520-700 nm, by combining the wavelength response of the W-12 filter which is unresponsive to wavelengths below 520 nm and the response of the film which is unresponsive to wavelengths above 700 nm. Timing marks were used to determine accurate frame rates as well as true time for each camera within a film series in order to time align multiple cameras.

Once time aligned, the intensity of the nuclear fireball was determined following the method described in Section 3.1 of this report. A pixel intensity threshold was established for each frame of the film in order to define the area of the image classified as the fireball. The centroid of this area of the image was then determined and defined as the center of the fireball. Figure 33 shows the results of determining the centroid of a particular frame. The intensity of each pixel in the image was then determined as a function of  $\theta$ , the angle between the line of sight of the detector to the center of the fireball and the direction of the emergent flux.

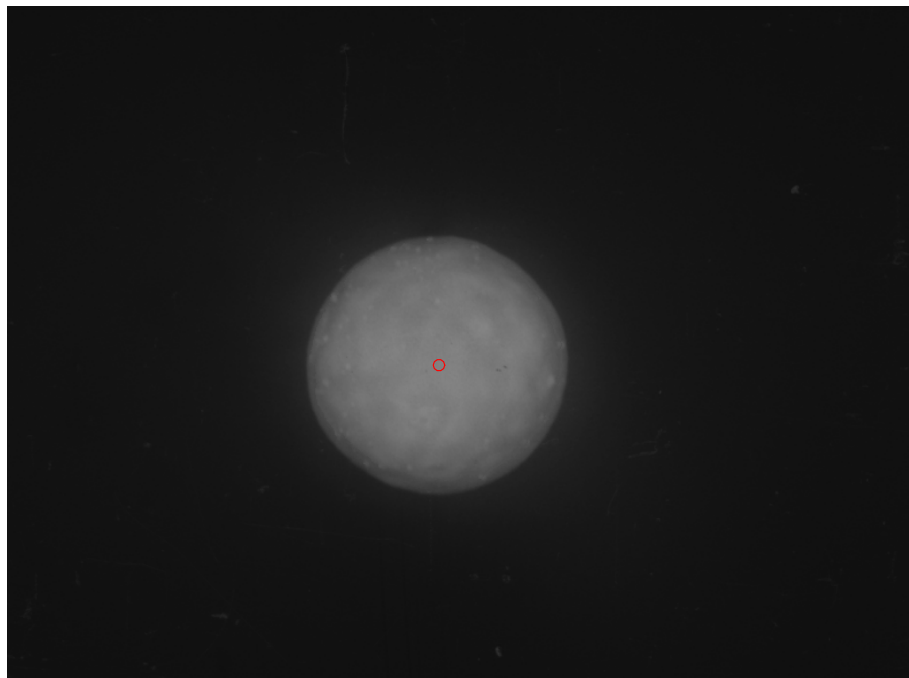


**Figure 33. The centroid of Wasp Prime (red circle).**

Random Sample Consensus (RANSAC), was then used to determine the best fit to seven different limb-darkening laws [49]. For RANSAC analysis 10 basis points were selected with a distance threshold of 0.20. This value was determined from analysis of varying distance thresholds. A value of 0.25 included nearly all points, include those

likely to be outliers, and a value of 0.15 often times resulted in unphysical solutions. The limb-darkening coefficients for each limb-darkening law, Equations 15-21, were chosen as the best fit line to the remaining inlier data points.

Once limb-darkening coefficients were determined, a weighting function based upon film optical density was used to determine an average coefficient value across multiple cameras. As the optical density increases, the uncertainty in energy flux also increases. Because of this relationship, films with lower optical density readings should have larger weights, as their uncertainty is smallest. Additional information on the weighting function is also discussed in Section 3.2, with results for Wasp Prime shown in Figure 19.

A second order polynomial fit to the coefficients was determined for two time periods of the film separated by approximately 1.8 ms following detonation. This separation was considered necessary because limb-darkening coefficients for Wasp Prime showed different behavior before and after this point in time following the detonation. The physical reasoning for this varying behavior is explained in more detail in Section 4.2. The uncertainty in the limb-darkening calculation was based upon the standard deviation from this best fit line of these second order polynomial curves and the weighted coefficient results.

## RANSAC.

The structure of a nuclear detonation, even for a free air detonation, is not entirely spherical. This is also true for a star, but to a lesser degree. In the case of a nuclear detonation this is predominately due to asymmetries caused by bomb debris and interaction with surrounding material like a tower detonation or varying atmospheric density. The temperature distribution of the surface of a nuclear fireball has significantly more variance than the temperature distribution of the surface of the

sun. This is highlighted in the Figure 34 which shows the specific intensity of each fireball pixel as a function of  $\theta$  for a single Wasp Prime frame. Of particular note is the wide variation in data, caused by fluctuations in temperature.

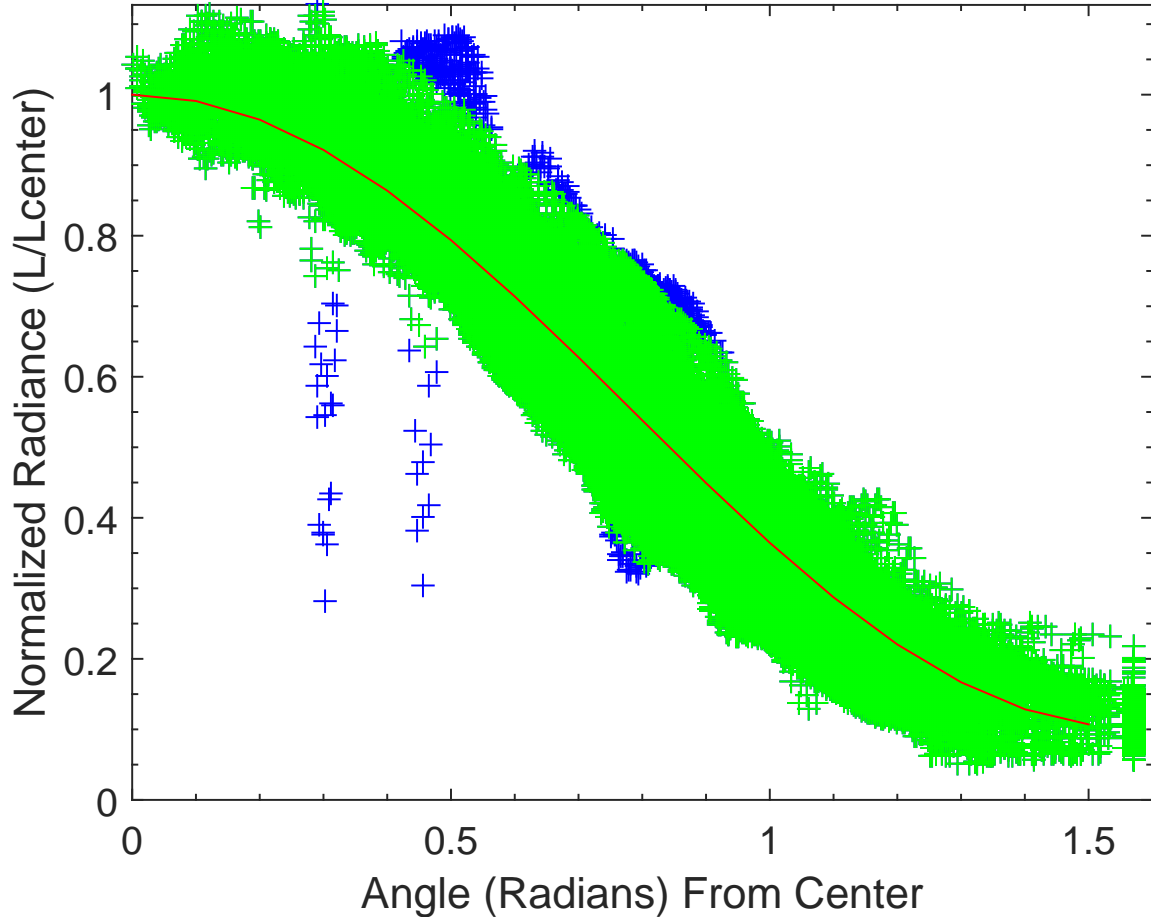


**Figure 34.** RANSAC applied to limb-darkening analysis. Blue data points are outliers and green data points are inliers.

Due to these large fluctuations in intensity, RANSAC was used to discard outlier data [49]. RANSAC uses an iterative Monte Carlo method to determine the best functional fit for noisy data. The RANSAC algorithm first selects a specified amount of sample data. For this research, a non-linear least squares routine was used to determine a least squares best fit using this randomly sampled data. Inliers and outliers were then defined as such by use of a specified distance threshold between the derived function and the full data set. Those points that meet the distance threshold

criteria are considered inliers and the remainder outliers. The inliers form what is referred to as the consensus set. The model then iterates a fixed number of times, 10,000 times for this research. A model can be accepted and continued with further refinement using the updated consensus set or be rejected because too few points were formed as part of the consensus set. This process continues for a defined number of iterations resulting in the model that best corresponds to the data with omitted noise. RANSACs most common applications are found in computer vision [50, 51, 52, 53], although it was used in this research to delineate outlier data caused by non-spherical fireball asymmetries and hot and cold spots. Figure 34 demonstrates the results of using RANSAC to perform a limb-darkening calculation on nuclear fireball data.

## 4.2 Results

### Limb-Darkening Coefficients.

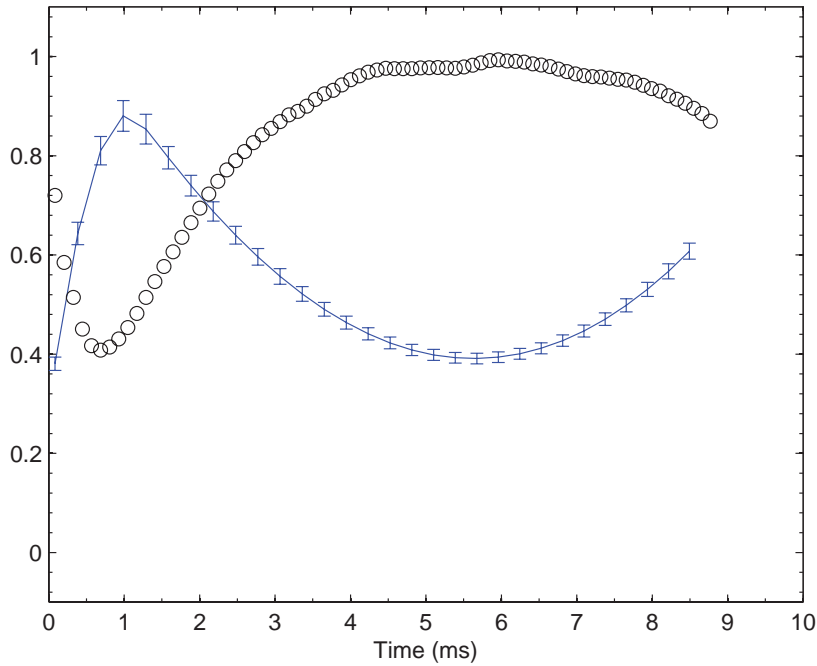


**Figure 35.** Example results of Wasp Prime limb-darkening coefficients for Equation 15. The blue line is coefficient (a) and the black circles are the normalized effective temperature of Wasp Prime.

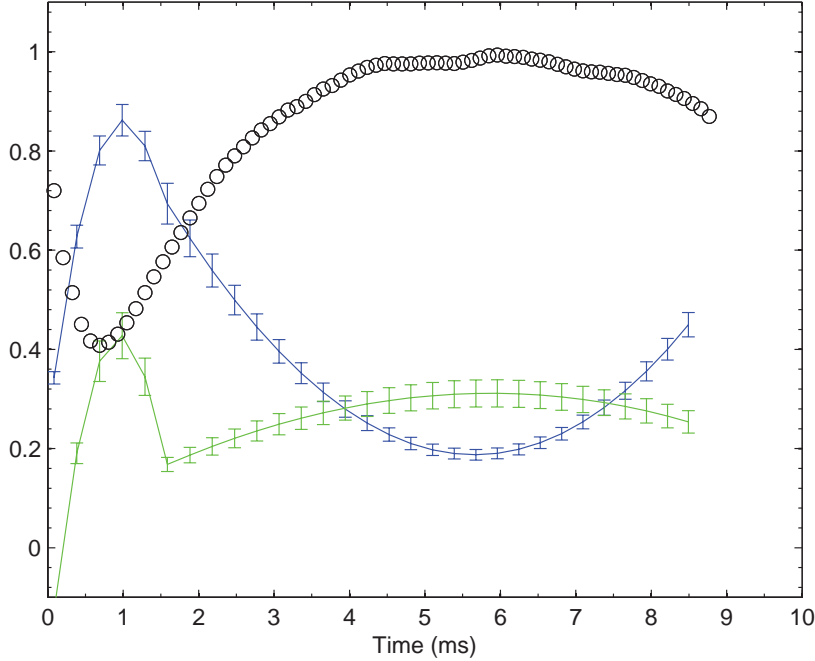


**Figure 36.** Example results of Wasp Prime limb-darkening coefficients for Equation 16. The blue line is coefficient (b), the green line is coefficient (c), and black circles are the normalized effective temperature of Wasp Prime.

Figures 35-41 are the compiled limb-darkening law results, which correspond to Equations 15-21. The black data points correspond to the normalized temperature of Wasp Prime. The colored data points correspond to their respective limb-darkening coefficients.

RANSAC analysis demonstrated that on average 90% of data points were constructed as inliers. Uncertainty was determined as one standard deviation from a best fit second order polynomial to the data set. The uncertainty in limb-darkening coefficients was observed to be highest near  $T_{min}$ , in this regime the number of inliers was drastically reduced for many of the frames down to approximately 50-70%. One explanation for this uncertainty in the data is the transition from frames observing the outer shock heated air to frames observing the optically thick inner fireball. This transition, when the shock heated air cools to a temperature at which it becomes transparent and an observer only views the inner fireball in the visual spectrum, is

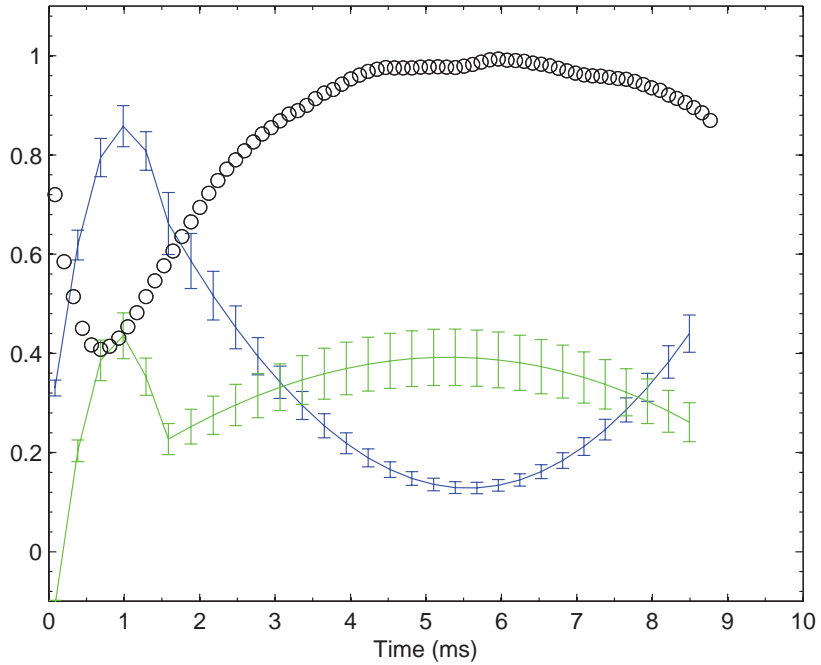


**Figure 37.** Example results of Wasp Prime limb-darkening coefficients for Equation 17. The blue line is coefficient (d), the green line is coefficient (f), and black circles are the normalized effective temperature of Wasp Prime.

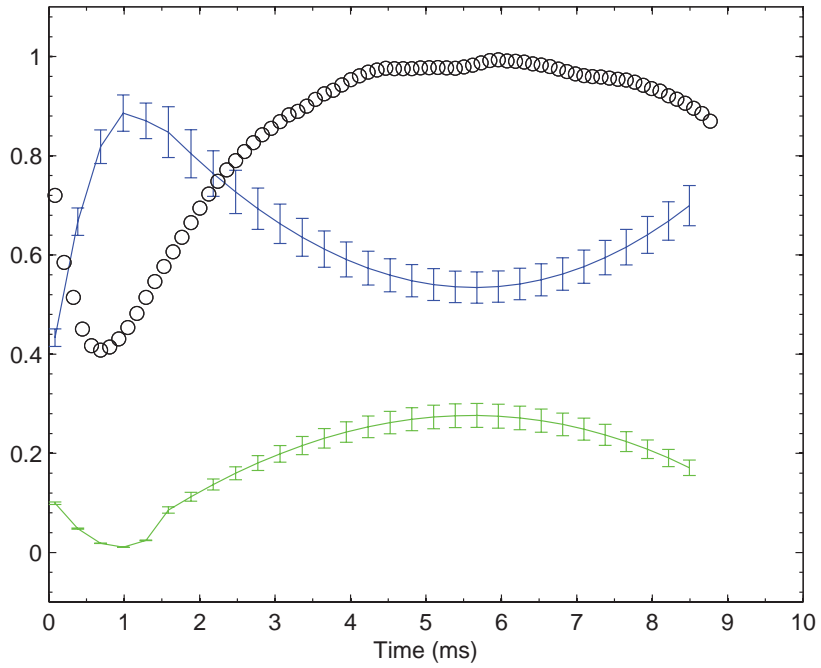


**Figure 38.** Example results of Wasp Prime limb-darkening coefficients for Equation 18. The blue line is coefficient (g), the green line is coefficient (h), and black circles are the normalized effective temperature of Wasp Prime.

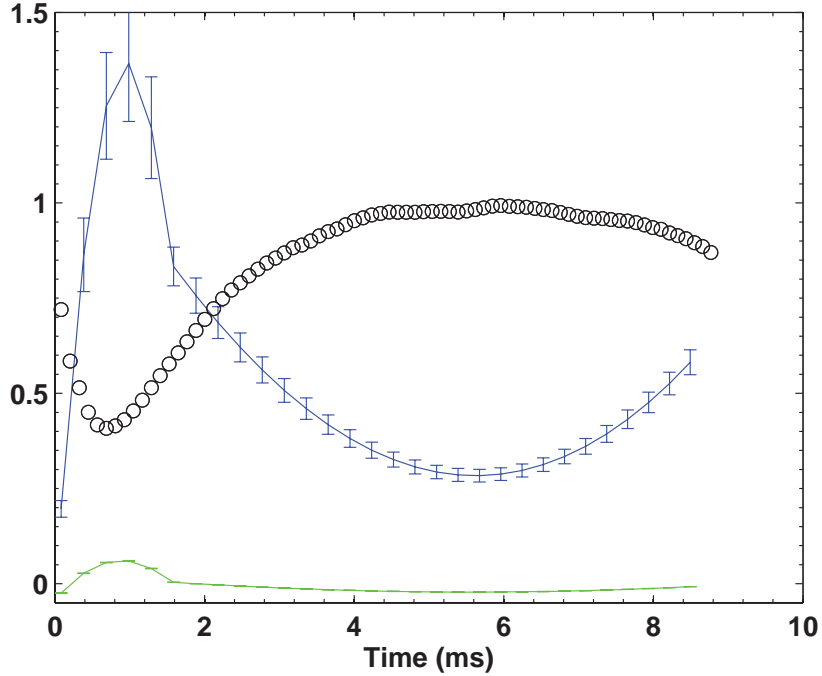


**Figure 39.** Example results of Wasp Prime limb-darkening coefficients for Equation 19. The blue line is coefficient (j), the green line is coefficient (k), and black circles are the normalized effective temperature of Wasp Prime.

known to occur near  $T_{min}$  and is commonly referred to as breakaway [26, 2].

Limb-darkening coefficients should be identical for bodies of identical temperature and composition. The apparent temperature of a fireball transitions through multiple increases and decreases, and therefore should have identical resultant coefficients at the same temperature which may occur at different times. However, the results show varying limb-darkening coefficients following the initial temperature maximum (first few frames) and points in later time of equal temperature. Because this is a free air detonation it is not likely that composition varied drastically from standard atmospheric values after the first few frames.

Hence, these two different regimes of fireball growth require limb-darkening coefficients to be bundled separately, one prior to breakaway and one after. This is the physical explanation for separating the best fit to limb-darkening coefficients into two separate time sequences, separated at 1.8 seconds for Wasp Prime.

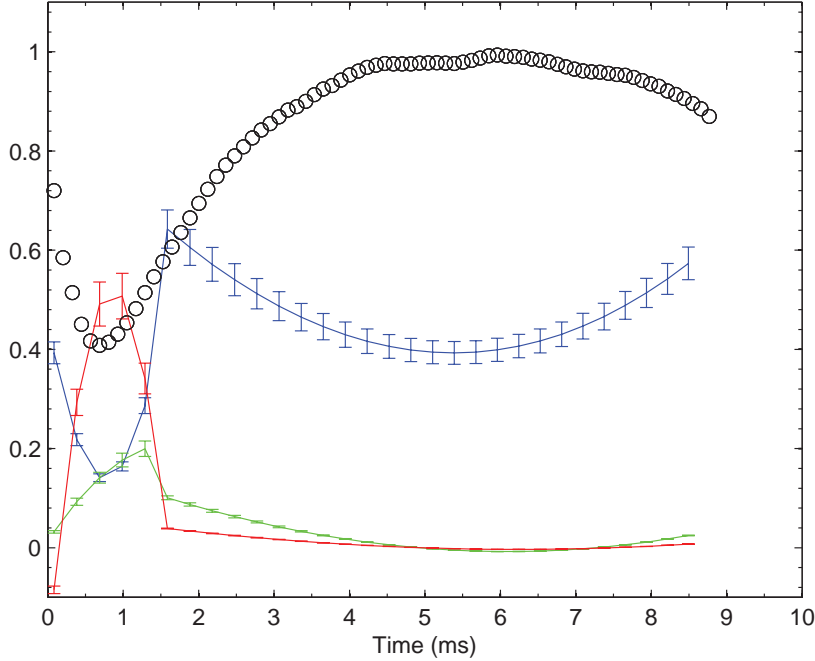


**Figure 40.** Example results of Wasp Prime limb-darkening coefficients for Equation 20. The blue line is coefficient (l), the green line is coefficient (m), the red line is coefficient (n), and black circles are the normalized effective temperature of Wasp Prime.

Also of interest are the results from Equations 19, 20, and 21, that show that following RANSAC analysis two of the coefficients are nearly zero at different time periods. When these higher order coefficients are equal to zero, Equations 19, 20, and 21 become equivalent to Equations 15 and 17.

### Limb-Darkening Coefficients Validation and Verification.

In order to verify limb-darkening coefficient results, the determined coefficients (Figures 35-41) were used to recalculate the expected radiance. This radiance value was then compared to the calculated radiance value as outlined in Section 3.2 for the seven films analyzed for this work. Figure 42 shows the comparison of the radiance derived from limb-darkening results to a radiance determined from a single frame at  $T_{min}$ . Figure 43 shows the same comparison, but for  $T_{max}$ .

Both Figures 42 and 43 were produced by first finding the centroid of the original

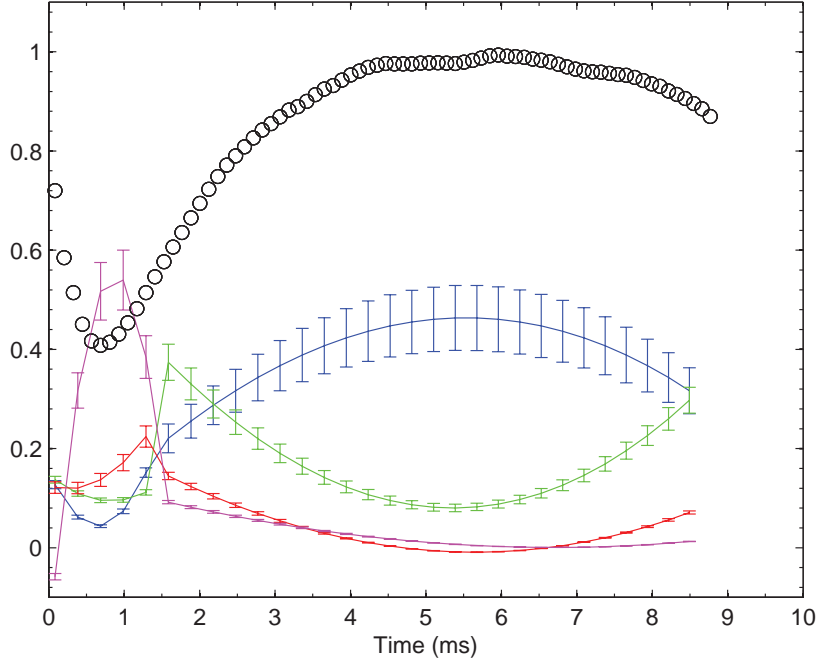


**Figure 41.** Example results of Wasp Prime limb-darkening coefficients for Equation 21. The blue line is coefficient (p), the green line is coefficient (q), the purple line is coefficient (r), the red line is coefficient (s), and black circles are the normalized effective temperature of Wasp Prime.

image and taking a threshold, as shown in Figure 18. The radius of the limb-darkening derived results were taken as the square root of the number of unmasked pixels divided by  $\pi$ . False color was added on a 0 – 1 (white-black) scale with 1 (white) being the normalized radiance found at the center of the fireball and 0 (black) being ambient air. Limb-darkening coefficients were taken from Equation 15.

Figures 44 and 45 are the difference images between the top and bottom portions of Figures 42 and 43. In Figures 44 and 45 white color indicates a larger intensity recorded in the actual image and black a lower intensity. The orange colored background shows a constant color value indicating a difference of some background pixel intensity of the real image compared to a zero intensity on the limb-darkening derived image. As shown in Figure 44 there is significant structure within the nuclear fireball. There are hot and cold spots likely caused by debris interacting with the nuclear fireball. Figure 45 shows that free air nuclear fireball has asymmetries likely due to

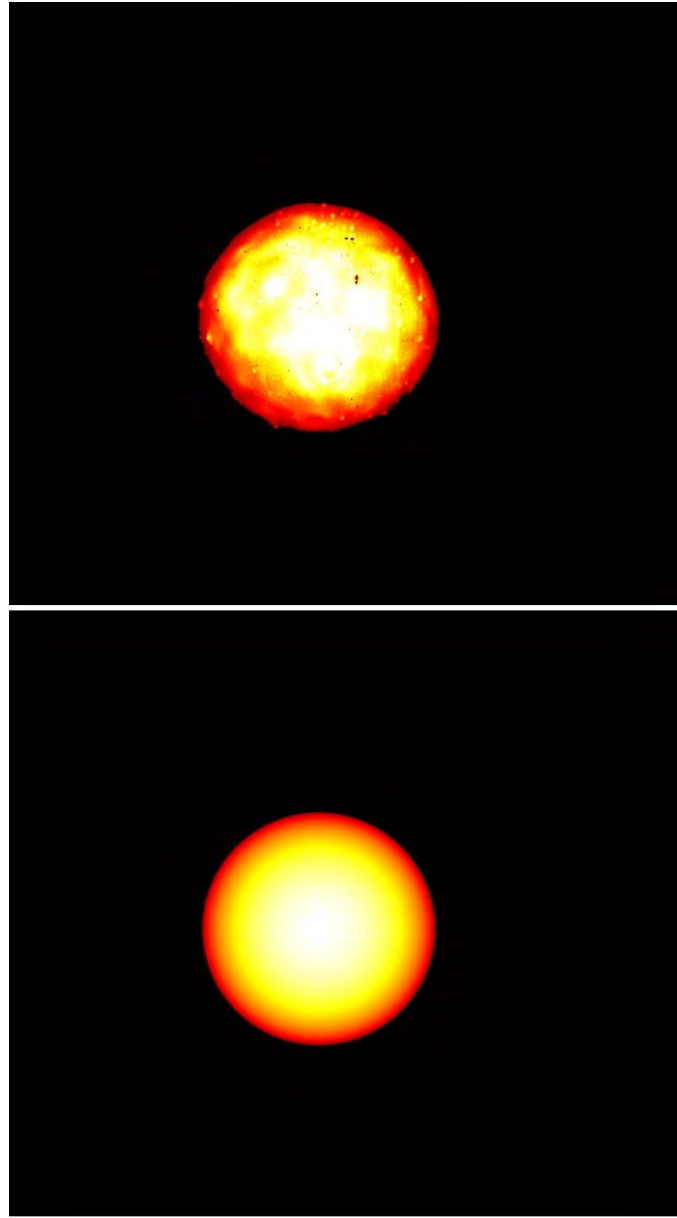


**Figure 42.** An example at  $T_{min}$  between the determined limb-darkening coefficients and the radiance values derived from film. The top image is the calculated radiance values of a single frame at  $T_{min}$ . The bottom image is the results of determining the radiance from derived limb-darkening coefficients. False color was added on a 0–1 (white-black) scale with 1 (white) being the normalized radiance found at the center of the fireball and 0 (black) being ambient air.

either variation in atmospheric density at different altitudes or interaction with the shock front which has reflected off the surface and returned.

This process of comparing the radiance determined using limb-darkening coeffi-

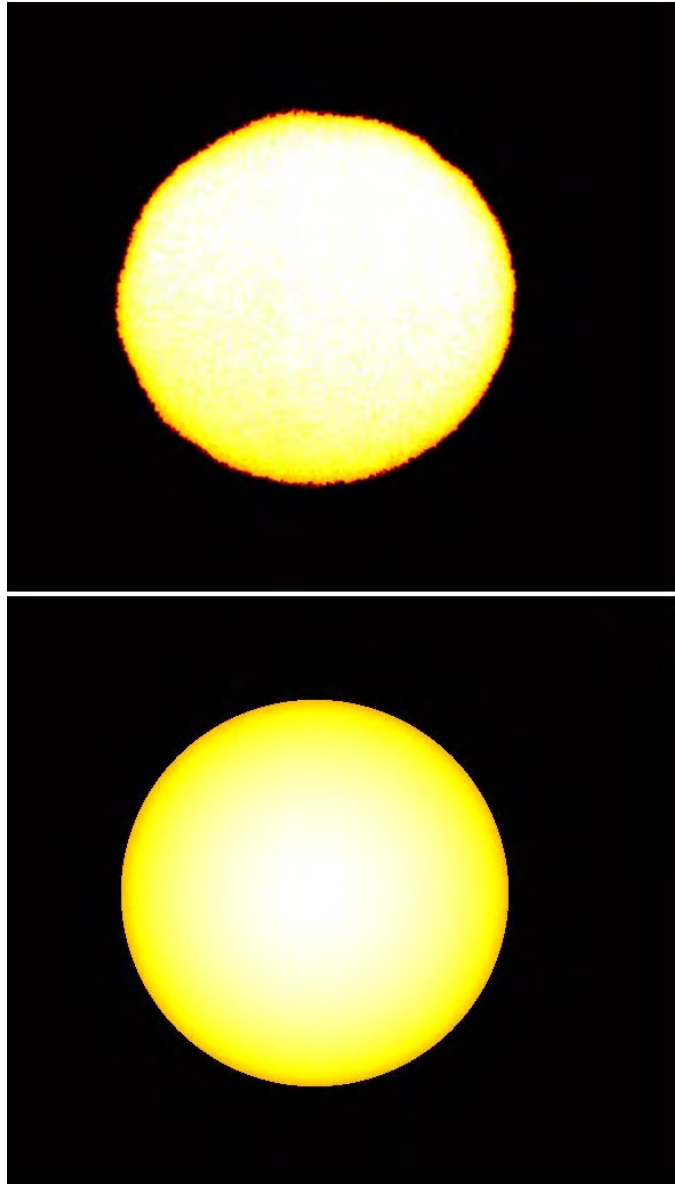


**Figure 43.** An example at  $T_{max}$  between the determined limb-darkening coefficients and the radiance values derived from film. The top image is the calculated radiance values of a single frame at  $T_{max}$ . The bottom image is the results of determining the radiance from derived limb-darkening coefficients. False color was added on a 0–1 (white-black) scale with 1 (white) being the normalized radiance found at the center of the fireball and 0 (black) being ambient air.

lients to the radiance observed in the films was then conducted for all the frames that were used in the analysis. Tables 3 and 4 show the results of this comparison isolating each unique film (Table 3) and each equation (Table 4).

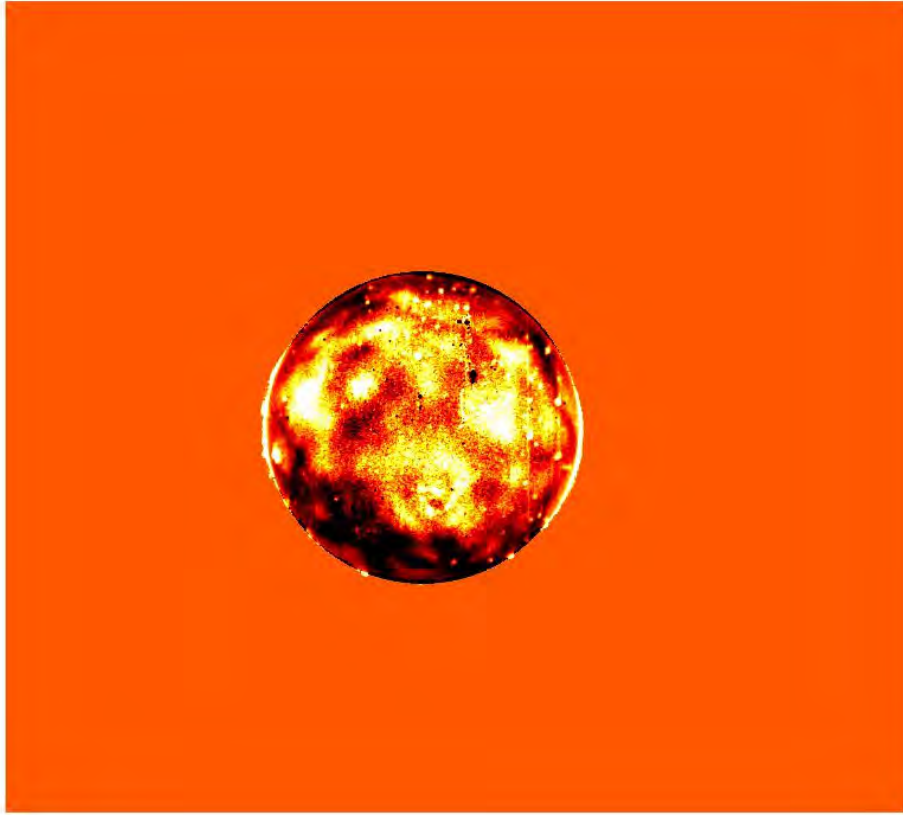


**Figure 44.** An example difference image at  $T_{min}$  between the determined limb-darkening coefficients and the radiance values derived from film. The image is colored according to the calculated residual with the maximum variation (white) set to 0.07 and the minimum (black) set to -0.07, where 1 is equal to the normalized radiance at the center of the fireball.

Table 3 shows the average residual over all frames for every film analyzed. Results show that the derived limb-darkening radiance agrees within  $0.11 I_o$  to the radiance derived from film analysis, where  $I_o$  is the radiance at the center of the fireball. With Film 4 having the best agreement with a residual of  $0.08 I_o$  and Film 5 having the worse agreement at  $0.107 I_o$ . It is important to note that the radiance derived from limb-darkening analysis is not expected to agree exactly with the radiance determined from the film. This is because the shape of the fireball derived from limb-darkening analysis is assumed to be perfectly circular, when in fact the fireball is more of an

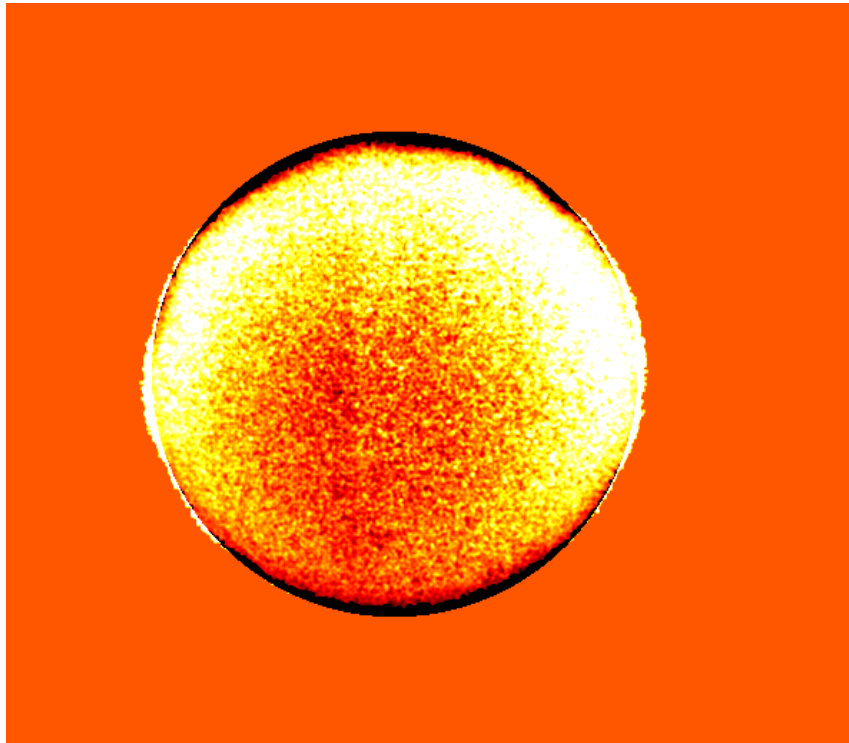


**Figure 45.** An example difference image at  $T_{max}$  between the determined limb-darkening coefficients and the radiance values derived from film. The image is colored according to the calculated residual with the maximum variation (white) set to 0.07 and the minimum (black) set to -0.07, where 1 is equal to the normalized radiance at the center of the fireball.

ellipsoid for event Wasp Prime. Additionally, there are a number of asymmetries predominately caused by bomb debris which make the radiance within the fireball non-uniform.

Table 4 shows the average residual over all frames for every equation that was used to investigate limb-darkening. The results show that the derived limb-darkening radiance agrees within  $0.125 I_o$  to the radiance derived from film analysis. With Equation 19 having the best agreement with a residual of  $0.066 I_o$  and Equation 21 having the worse agreement at  $0.124 I_o$ .

**Table 3. Limb-Darkening Results Compared to Film: Per Film**

Film	Residual
Film 1	0.105
Film 2	0.094
Film 3	0.082
Film 4	0.080
Film 5	0.107
Film 6	0.093
Film 7	0.094

**Table 4. Limb-Darkening Results Compared to Film: Per Equation**

Equation	Residual
Equation 15	0.080
Equation 16	0.088
Equation 17	0.103
Equation 18	0.097
Equation 19	0.066
Equation 20	0.084
Equation 21	0.124

### Limb-Darkening Law Consistency.

If valid, the coefficients derived from limb-darkening analysis should produce the same physical environment, i.e the same specific intensity results. An example of an intensity profile for a single snapshot in time is shown in Figure 46. In Figure 46, five of the seven limb-darkening laws have good agreement out to 10 optical path lengths for this single snapshot in time, with the two exceptions being Equations 16 and 18. Equation 18 shows a much sharper rise in intensity than other limb-darkening laws, and Equation 16 begins to show unphysical results after about 6 optical path lengths, with an intensity profile that begins to decrease deeper into the fireball.

Normalized specific intensity plots, similar to Figure 46, were derived for every frame from 0.1 ms up to approximately 10 ms of data. The relative deviation across 10 optical path lengths as a function of time was determined with results shown

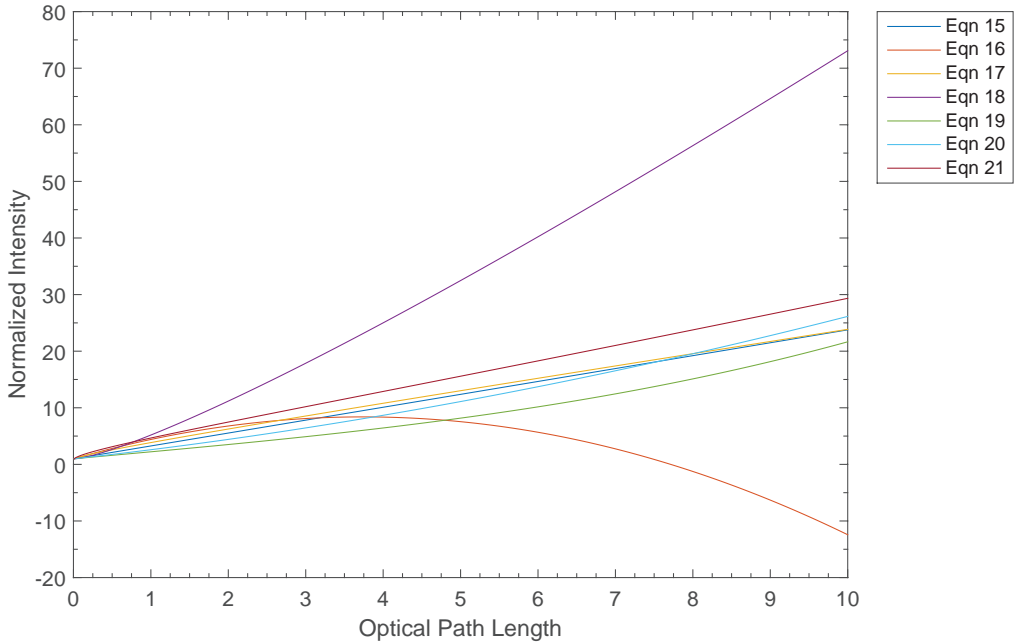


**Figure 46.** Example of the intensity profile out to 10 optical path lengths for the seven limb-darkening laws investigated.

in Figure 47 for each of the seven limb-darkening laws investigated. The relative deviation is taken as the difference from a single limb-darkening law result compared to the average result for every frame across optical path lengths in increments of 0.1 from 0 to 10. This relative deviation was then normalized by dividing by the mean intensity at every point.

As Figure 47 demonstrates, Equations 16 and 18 appear to be outliers within the data set with relative deviations at or above 0.40. Equations 15, 17, 19, 20, and 21 all appear to have good agreement with each other. This can be further highlighted by taking the average deviation between all seven equations as a function of time compared to five equations with Equations 16 and 18 omitted, as shown in Figure 48. It is important to note that when the higher order coefficients of Equations 19, 20, and 21 approach values close to zero, they reduce in form to Equations 15 and 17. Under these circumstances these equations become equivalent and as expected they

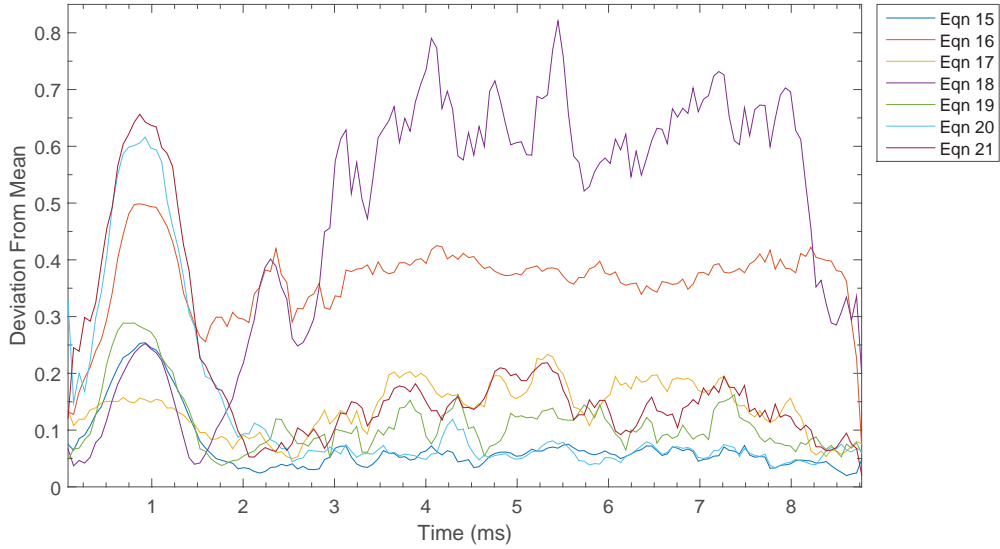


**Figure 47.** The relative deviation of limb-darkening laws out to 10 optical path lengths for the seven limb-darkening laws investigated in this dissertation.

agree.

Figure 47 shows that a much larger discrepancy is present at times of approximately 1 ms. This time corresponds well with  $T_{min}$  for Wasp Prime as shown in Figure 20. At this point in time the relative deviation amongst these limb-darkening laws is highest for every limb-darkening law with the exception of Equation 18. Previous research has shown that the uncertainty in optical intensity near  $T_{min}$  is relatively low [25]. This high level of uncertainty in limb-darkening laws has a likely physical explanation. During this transition point the optical intensity is formed from a source demonstrating two different behaviors near breakaway as discussed previously. There is the outer shock heated optically thin air, but also the optically thick and hotter inner fireball region. In the calculations performed in this report it is likely that RANSAC analysis transitioned between accepting (inlier) and rejecting (outlier) certain data points that pertain to the two different emitting bodies.

Figure 49 shows the relative standard deviation of both the complete set (seven) and reduced set (five) of limb-darkening laws as a function of optical path depth

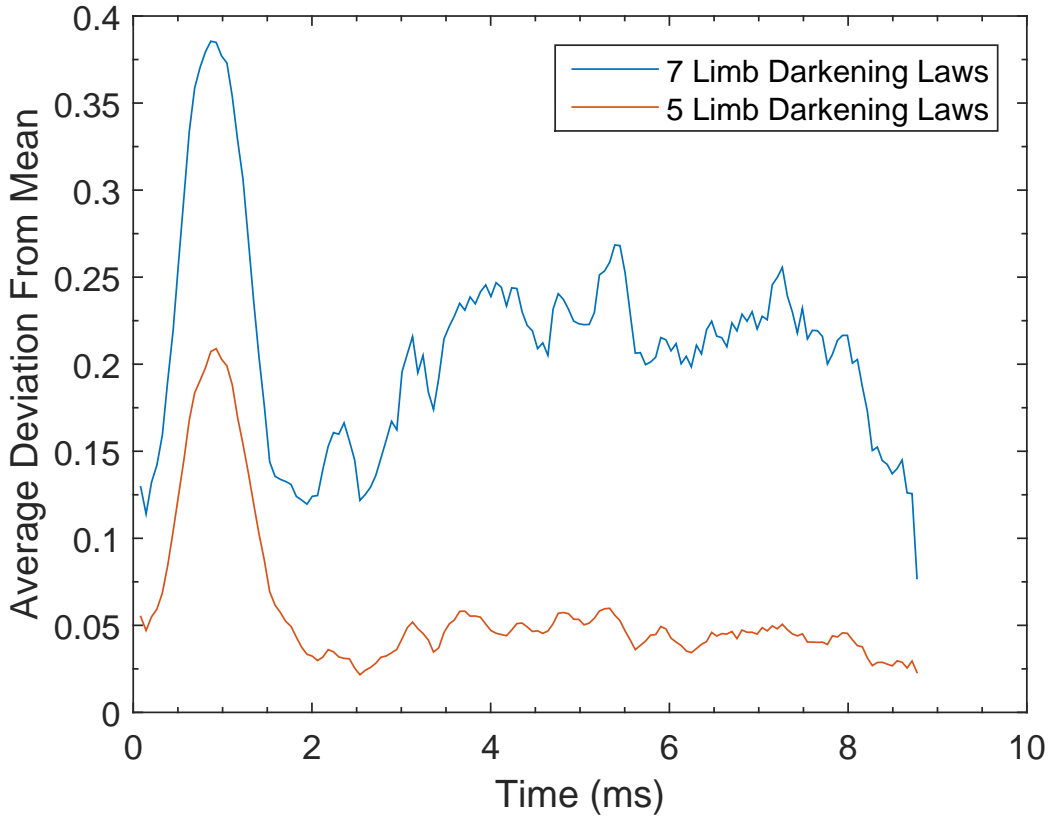


**Figure 48.** The average relative deviation of limb-darkening laws out to 10 optical path lengths for the seven limb-darkening laws compared to that of five of the limb-darkening laws (Equations 16 and 18 omitted).

$(\tau)$ . As shown, the correlation of intensity profiles in both cases agrees well for  $\tau$  less than four, after which both groups begin to diverge. For a  $\tau$  of five and greater, the relative standard deviation of all seven laws is nearly 40%. For the reduced data set, the deviation at five  $\tau$  is less than 15%. From a correlation standpoint these equations agree well with each other in the intensity profile of a nuclear fireball up to a minimum of five optical path lengths.

#### Temperature Profiles from Limb-Darkening Laws.

The temperature profile of a nuclear fireball can in turn be determined using the limb-darkening equations. The radiance as a function of  $\tau$  can be determined by

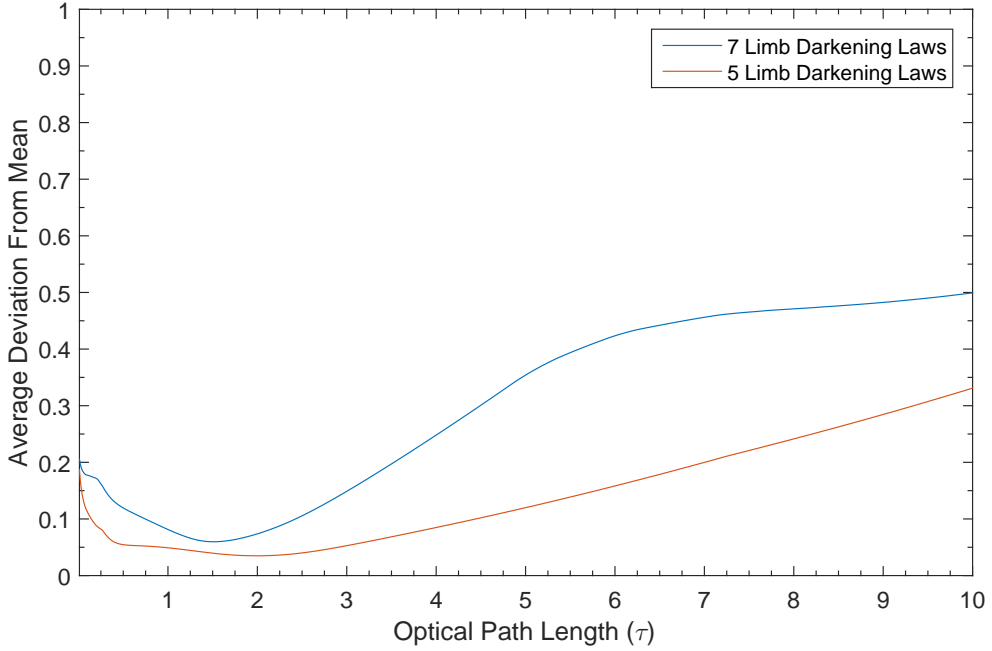


Figure 49. The average relative deviation of limb-darkening laws between 0.1 and 10 ms as a function of optical path length for the seven limb-darkening laws introduced in this report compared to that of five of the limb-darkening laws (Equations 16 and 18 omitted).

$$B^*(\tau) = I(1) * (a_0 + a_{\frac{1}{2}}\tau^{\frac{1}{2}} + a_1\tau + a_{\frac{3}{2}}\tau^{\frac{3}{2}} + a_2\tau^2 + a_{ln}\tau\log(\tau) + a_3\tau^3). \quad (25)$$

Where  $I(1)$  is the calculated apparent radiance at the center of the fireball and  $a_x$  are the determined limb-darkening coefficients.  $B^*$  is also a function of temperature

$$B^* = \int_{\lambda_1}^{\lambda_2} \frac{2hc^2}{\lambda^5} \frac{1}{e^{\frac{hc}{\lambda kT}} - 1} d\lambda, \quad (26)$$

where  $h$  is Planck's constant,  $\lambda$  is the wavelength,  $c$  is the speed of light in a vacuum,  $k$  is the Boltzmann constant,  $T$  is the temperature, and  $\lambda_1$  and  $\lambda_2$  are the bounds determined by the frequency response of the filters, lens, and film type, 520 nm and 700 nm in this case [20]. The temperature that satisfies Equations 26 and 25

is interpreted as the temperature at that specific optical depth. Figures 50 and 51 provide the results of applying each limb-darkening coefficient to Equation 25 and solving for temperature using Equation 26.

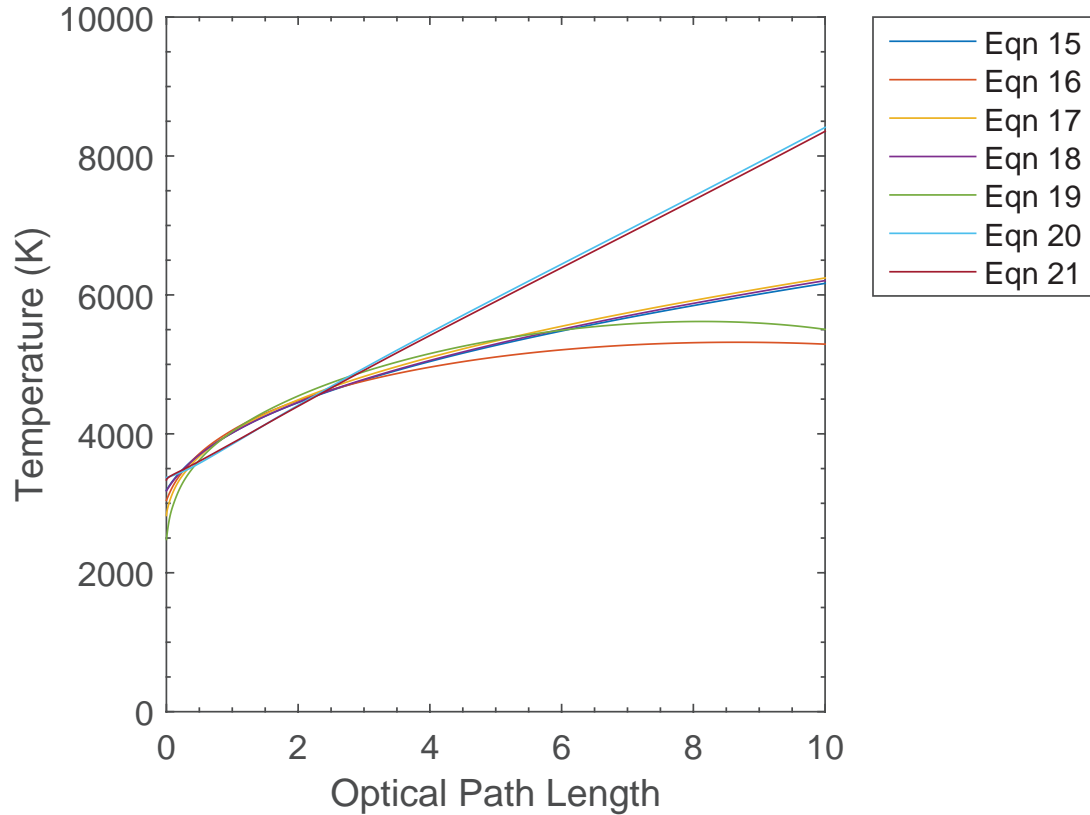


**Figure 50.** Temperature profile of Wasp Prime at temperature minimum for the seven limb-darkening laws investigated in this dissertation.

Figure 50 shows that according to limb-darkening results the surface of the fireball near  $T_{min}$  is approximately 3,000 K with good agreement between all seven limb-darkening laws. At 10 optical path lengths internal to the fireball, limb-darkening results show a temperature that varies with results as high as 8,000 K or as low as 5,000 K. At the second temperature maximum limb-darkening results show a surface temperature near 8,000 K and at 10 optical path lengths a temperature as high as 35,000 K or as low as 18,000 K. Equation 16 is not included in that simple analysis

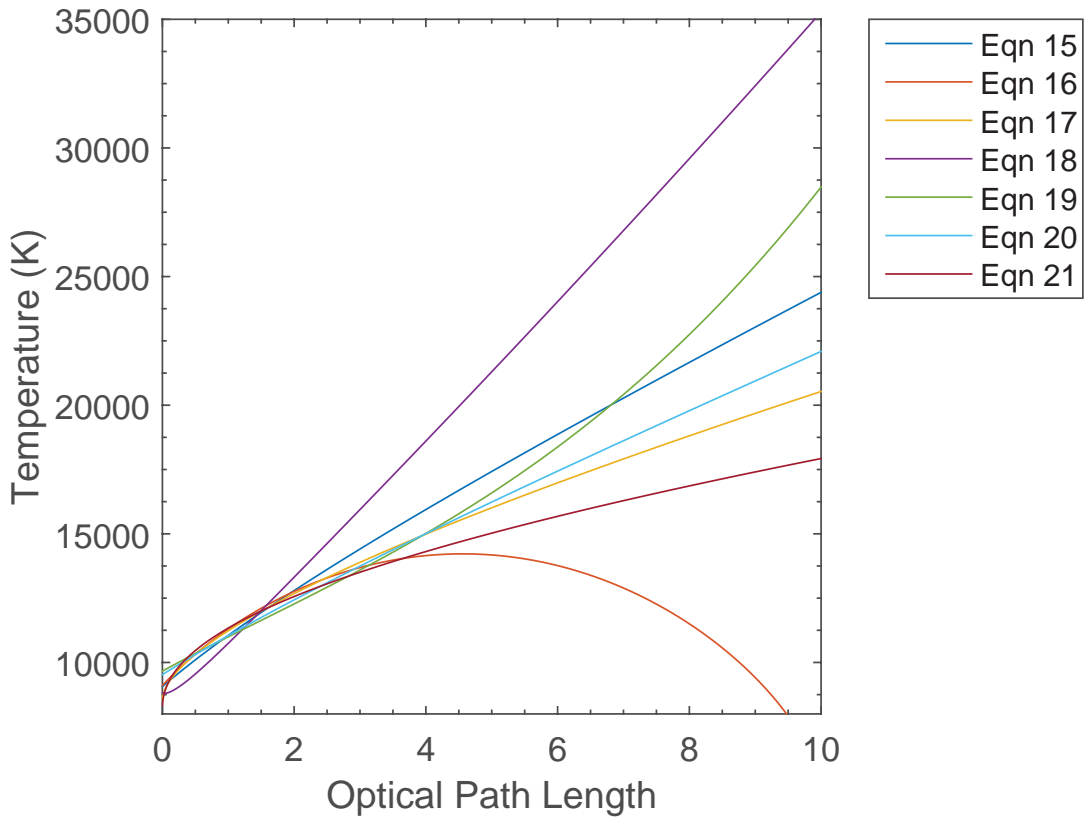


**Figure 51.** Temperature profile of Wasp Prime at temperature maximum for the seven limb-darkening laws investigated in this dissertation.

because at about 5 optical path lengths the fireball temperature is shown to decrease, which is not a physical result.

### 4.3 Discussion

Previous limb-darkening research has focused on interstellar bodies, with predominately hydrogen and helium composition. With the digitization of nuclear effects data, a variety of scientific studies can be performed on the unique environment created by a nuclear detonation. A free air nuclear detonation is comprised predominately of Earth atmosphere. This dissertation outlines the process and provides results for applying seven limb-darkening laws to the observations of a nuclear detonation us-

ing digitized data. The results indicate that five of the seven laws are consistent with each other, agreeing within 15% out to 5 optical path lengths. These same five limb-darkening laws also agree to within approximately 5% of each other for all times between 2 to 10 ms, but show disagreement between 0.1 ms and 2 ms. For Wasp Prime this time period corresponds to  $T_{min}$ , and breakaway has been identified as a possible physical reasoning behind this higher uncertainty at this point in time.

Validation and verification of this technique was performed by comparing a nuclear fireball radiance image derived from limb-darkening coefficients to radiance determined from digitized film corresponding to a time aligned frame. Results showed agreement on average within 0.125  $I_o$  for every film and equation analyzed.

## V. 3D Reconstructions of Nuclear Fireballs

### 5.1 Computer Vision Introduction

#### Multiple View Geometry Reconstruction.

The geometry of interest for computer vision was primarily developed from photographic and artistic studies conducted many years before the advent and widespread use of the computer. The geometry of two camera views is known as epipolar geometry. Epipolar geometry is the primary facilitator for many algorithms involving computer vision, particularly 3D reconstruction.

The basic outline for 3D reconstruction can be simplified as the following series of tasks [53]

1. Collect a series of images of a scene from multiple views (at least two)
2. Find key features within each single image
3. Match image features between image sets
4. Determine relative camera positions based upon base image and linear least squared analysis of key image relationships
5. Compute a 3D point cloud from image relationships
6. Generate a dense point cloud, mesh, and texture

To begin, a multitude of images are collected through either a camera or captured by video. Diversity of perspective is an important aspect, as the best reconstructions require different viewpoints, however, too much diversity of perspective may make developing relationships between images difficult or even impossible.

The next steps in a 3D reconstruction process are feature detection and matching between images. In order for matches to be made between multiple images, knowledge of epipolar geometry is required. Epipolar geometry relates two cameras views of a 3D scene and their projections onto the 2D images formed through the camera. In the simplest approach the camera is modeled as a pinhole.

In practice, the pinhole model is usually chosen with the focus behind the image plane in order to form an erect image. In many approaches, a common reference point for each image is sought through a process known as rectification. Rectification determines a transformation of each image such that pairs of epipolar lines become co-linear and parallel to one of the image axes. Epipolar lines are the lines that intersect a point on the image plane and the epipole, which is defined as the intersection of the camera center between two views. Epipolar geometry is shown in Figure 52 with the epipoles and epipolar lines drawn. Also shown in Figure 52 is the epipolar plane, which is the plane that is formed from intersection of the epipoles, camera center, and matching image points [53].

One can relate a point on one image ( $x$ ) to the epipolar line ( $l'$ ) on the adjoining image by using the fundamental matrix ( $F$ )

$$Fx = l', \quad (27)$$

where  $F$  satisfies

$$x' F x = 0 \quad (28)$$

and where  $x'$  is the point on one image and  $x$  the matching point on another image. Equation 28 is known as the fundamental null hypothesis. Equation 28 shows that in order for  $x$  and  $x'$  to be the same point in real world space, then  $x'$  must lie within

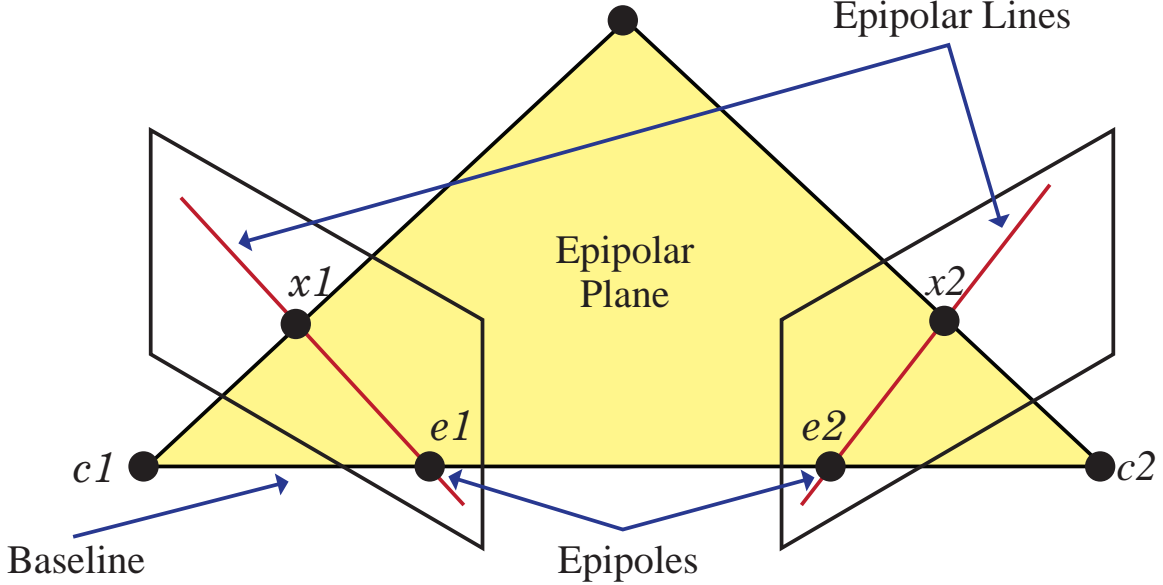


Figure 52. A diagram of epipolar geometry that shows the lines that extend from two cameras centers ( $c_1$  &  $c_2$ ) to a matched point ( $x_1$  &  $x_2$ ) to a real world location. The epipolar line connects the camera planes ( $e_1$  &  $e_2$ ) to the image centers [54].

the epipolar line  $l'$ .

In order to relate a real world point to an image point one must use the  $3 \times 4$  camera projection matrix  $P$

$$x = P X, \quad (29)$$

where  $X$  is the homogeneous representation of 3D points and

$$P = K[RT] = KR[I|C], \quad (30)$$

where  $R$  is the rotation matrix relating the camera orientation to real world orientation,  $K$  is the internal camera calibration matrix,  $I$  is the identity matrix,  $C$  is the camera location, and  $T$  is the translation vector.  $T$  can be determined by

$$T = -RC, \quad (31)$$

where  $C$  is the 3D coordinates of the camera center in real world coordinates. The rotation matrix is constructed by assuming the camera's rotation is determined by two Euler angles: one angle relating the camera easting and another relating the cameras tilt. Both of these angles are found on a typical film data sheet for reconstruction involving nuclear testing data. Additionally  $C$  can be determined by relating the film data sheet information (Nevada Test Site coordinates) to real world coordinates chosen with the origin at detonation center.

The camera calibration  $K$  is a  $3 \times 3$  matrix

$$K = \begin{pmatrix} f_x & s & c_x \\ 0 & f_y & c_y \\ 0 & 0 & 1 \end{pmatrix}, \quad (32)$$

where  $f_x$  and  $f_y$  are equal to the focal length in pixels in the x and y directions respectfully,  $s$  is the image skew, and  $c_x$  and  $c_y$  are the image x and y principal points. The focal length is taken from the camera data sheet for the specific camera. In order to determine  $f_x$  and  $f_y$ ,  $c_y$  and  $c_x$ , the conversion between millimeters and pixels is determined by comparing the known camera dimensions to those measured in terms of pixels. This analysis assumes no radial distortion. The principal point is assumed to be the center point of the exposed region of the film. Image skew is assumed to be 0. Radial distortion is also assumed to be zero.

A linear triangulation solution to this equation exists by utilizing the vector cross product, where  $P^T$  is the transpose of  $P$ , as shown in Equation 33.

$$\begin{pmatrix} 0 & -X_i^T & y_i X_i^T \\ X_i^T & 0 & -x_i X_i^T \\ -y_i X_i^T & x_i X_i^T & 0 \end{pmatrix} \begin{pmatrix} P^{1T} \\ P^{2T} \\ P^{3T} \end{pmatrix} = 0. \quad (33)$$

Equation 33 can be reduced to

$$\begin{pmatrix} 0 & -X_i^T & y_i X_i^T \\ X_i^T & 0 & -x_i X_i^T \end{pmatrix} \begin{pmatrix} P^{1T} \\ P^{2T} \\ P^{3T} \end{pmatrix} = 0. \quad (34)$$

An equation of the form  $AX = 0$  can be solved where  $A$  is equal to the  $3 \times 3$  matrix in Equation 33, with  $x$  minimized in  $Ax = 0$  subject to  $\|x\| = 1$  by taking the singular value decomposition of  $A$  [53]. The  $X$  real world 3D points are then equal to the normalized last column of  $V$ , where  $A = UDV^T$ . This linear triangulation solution is commonly referred to as the direct linear transformation (DLT). The DLT is used in many multiple view geometry solutions as the first estimate prior to a non-linear optimized solution.

### Bundle Adjustment.

If noise is present from image acquisition or key point matching, then  $x = PX$  can not be solved exactly. Assuming the noise is Gaussian, a maximum likelihood method can be used to refine the solution towards a minimization between the projection matrix and real world points relative to image points. This minimization referred to as bundle adjustment solves

$$\min_{\hat{P}, \hat{X}_j} \sum_{ij} d\left(\hat{P}^i \hat{X}_j, X_j^i\right)^2. \quad (35)$$

Bundle adjustment relies heavily upon a good initialization. For this work, the initialization is determined from using information from the camera data sheet.

### Feature Detection.

Many feature detection algorithms have been developed for computer vision applications [55, 56, 57]. The vast majority of them rely upon some form of edge detection

in order to determine at which point in an image a key or interesting feature exists. Edge detectors predominately use either a gradient or Laplacian operator or a differencing method. Edge detectors normally follow a similar routine of smoothing using a convolution, applying edge enhancement filters, applying a threshold, and tracing the threshold edges.

Two of the most widely used feature detection and matching algorithms are Scaled Invariant Feature Transform (SIFT) and Speeded Up Robust Features (SURF). SIFT is a computer vision algorithm developed by Dr. David Lowe in 1999 that does feature detection and matching between two images [56]. The algorithm conducts five key steps: feature detection using a difference of Gaussian edge detection; feature matching and indexing using a k-d tree algorithm; cluster identification by Hough transform voting; model verification by linear least squares comparing multiple solved camera parameters such as the fundamental matrix to actual data; and outlier detection to determine which points to consider for matches between images. Although this algorithm is in a field that is constantly changing, SIFT has continued to be used in feature detection and matching by many researchers in their approaches to solving computer vision problems.

SURF is a scale and rotation-invariant point detector and descriptor [57]. SURF uses a Hessian matrix in what is termed a fast-Hessian detector method for feature identification. SURF then uses a Haar-wavelet response for descriptor information for each feature. These features can then be matched to other images through similarities in their descriptors.

Both SIFT and SURF algorithms demonstrate the ability to match across images captured from cameras located within the same site location. Figure 53 shows this capability, where the teal lines are those inlier matches accepted after running RANSAC against initial matched points.

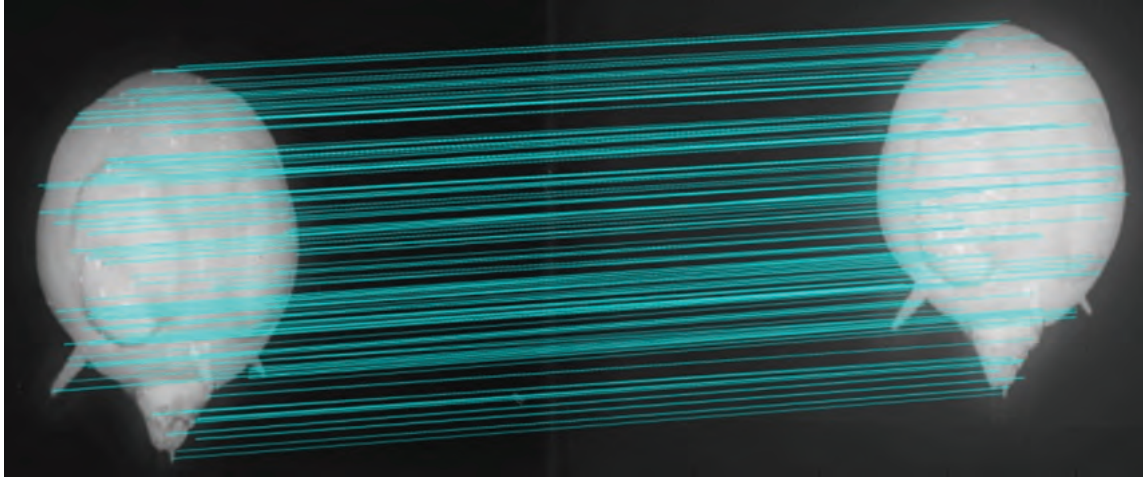


**Figure 53. SIFT for automatic feature correspondences between two time aligned nuclear fireball images at the same camera viewing location**

### 3D Reconstruction Uncertainty.

To quantify error in the reconstruction of a nuclear fireball using multiple view geometry, a 3D reconstruction was accomplished on tower detonations [48]. The locations and sizes of the towers were known, so the reconstruction could be compared to ground truth. Points were manually selected for different floors of each tower. An example of how the towers appear in nuclear testing films is shown in Figure 54.

For reconstructions, points were matched from cameras located at different viewing stations. The determination of the uncertainty of points in 3D space generated from triangulation and bundle adjustment using this ground truth NUDET film data provides the baseline for other 3D reconstruction techniques.

Two reconstructions were generated for each combination of two viewpoints for Teapot tests Tesla, Met, and Turk. One reconstruction used the triangulation method that solved for 3D points using singular value decomposition. The second reconstruction was run through a bundle adjustment algorithm to refine the camera calibration matrix and create a bundle adjusted reconstruction. The ability of the two approaches to accurately match ground truth can then be used to quantify uncertainty.

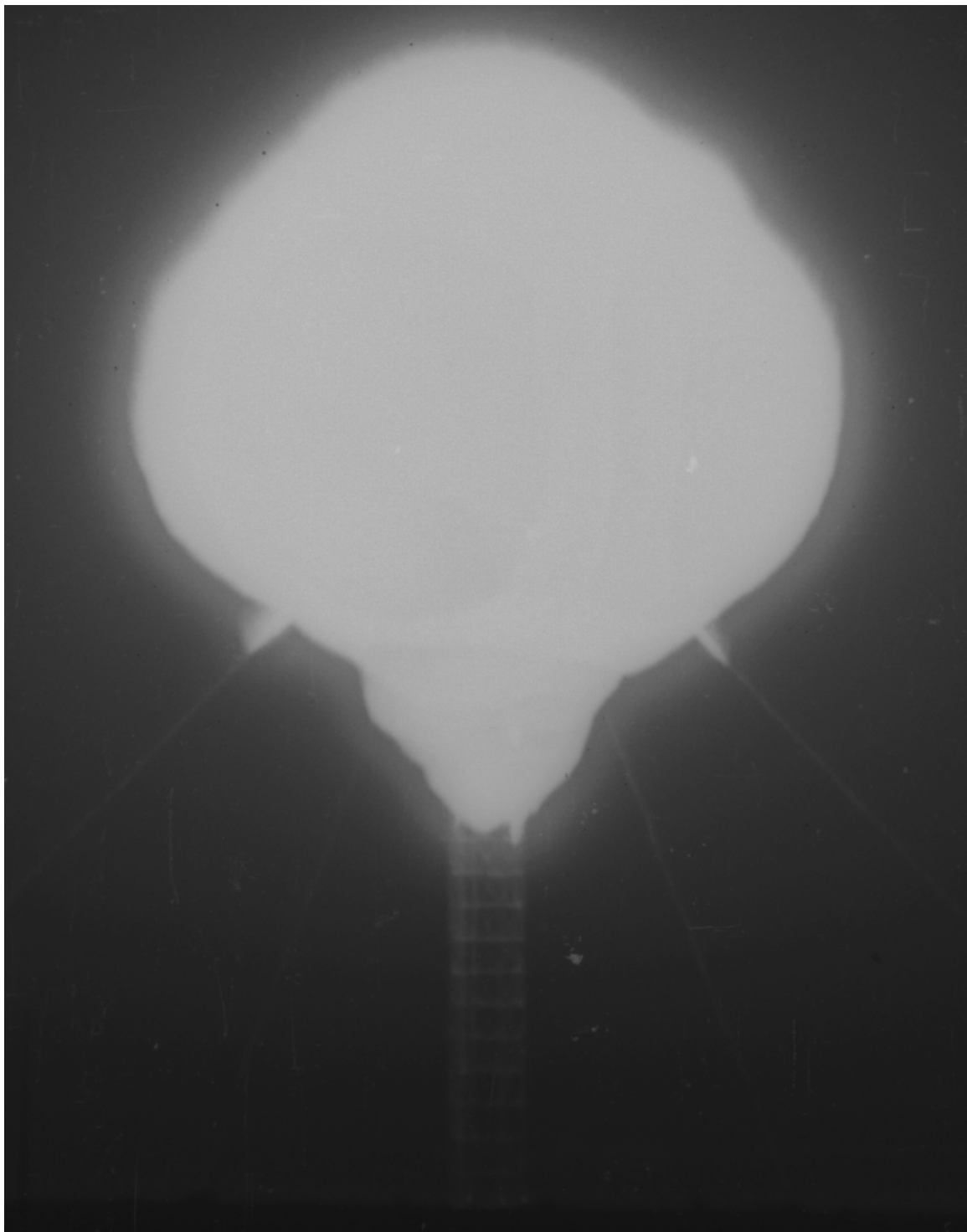


Figure 54. This figure shows one of the towers used for 3D sparse reconstruction of nuclear fireball towers for event Tesla.

Matched points for events were selected manually at select locations of each tower. Ten points were reconstructed of each tower using triangulation and bundle adjusted reconstructions. Each point was then compared to the ground truth location of each point. The average difference between ground truth using triangulation was 0.83 meters and the average difference using bundle adjustment was 0.68 meters.

These results highlight the capability of multiple view geometry to accurately reconstruct real world locations using matched points from different camera locations from historical nuclear tests at sub-meter resolution. The primary missing component to be able to perform this same type of reconstruction for a nuclear fireball is an automatic feature detection and matching algorithm. As is discussed in the next section, no investigated algorithm has been shown to be successful.

### **Issues with Automatic Feature Detection.**

A 3D sparse reconstruction of event Tesla using matched points for SIFT is shown in Figure 53. The 3D bundle adjustment solution outlined in this report using the matched points is shown in Figures 55 and 56. Both figures are from the same reconstruction, using three cameras, located at the same viewing location.

Figure 55 demonstrates what appears to be an accurate reconstruction in two of the spatial directions. But as Figure 56 demonstrates the  $z$  or depth component has an uncertainty greater than 50 meters. With a radius under 100 meters, this sparse reconstruction does not have sufficient accuracy to meet the requirements of true real world applications. This high degree of uncertainty stems from the fact that the cameras used for the reconstruction had a field-of-view separation of less than  $0.05^\circ$ . A 3D reconstruction following a multiple view geometry from such a small angular view separation results in uncertainties in the depth component that are too high for the desired applications. An accurate 3D sparse reconstruction requires matching

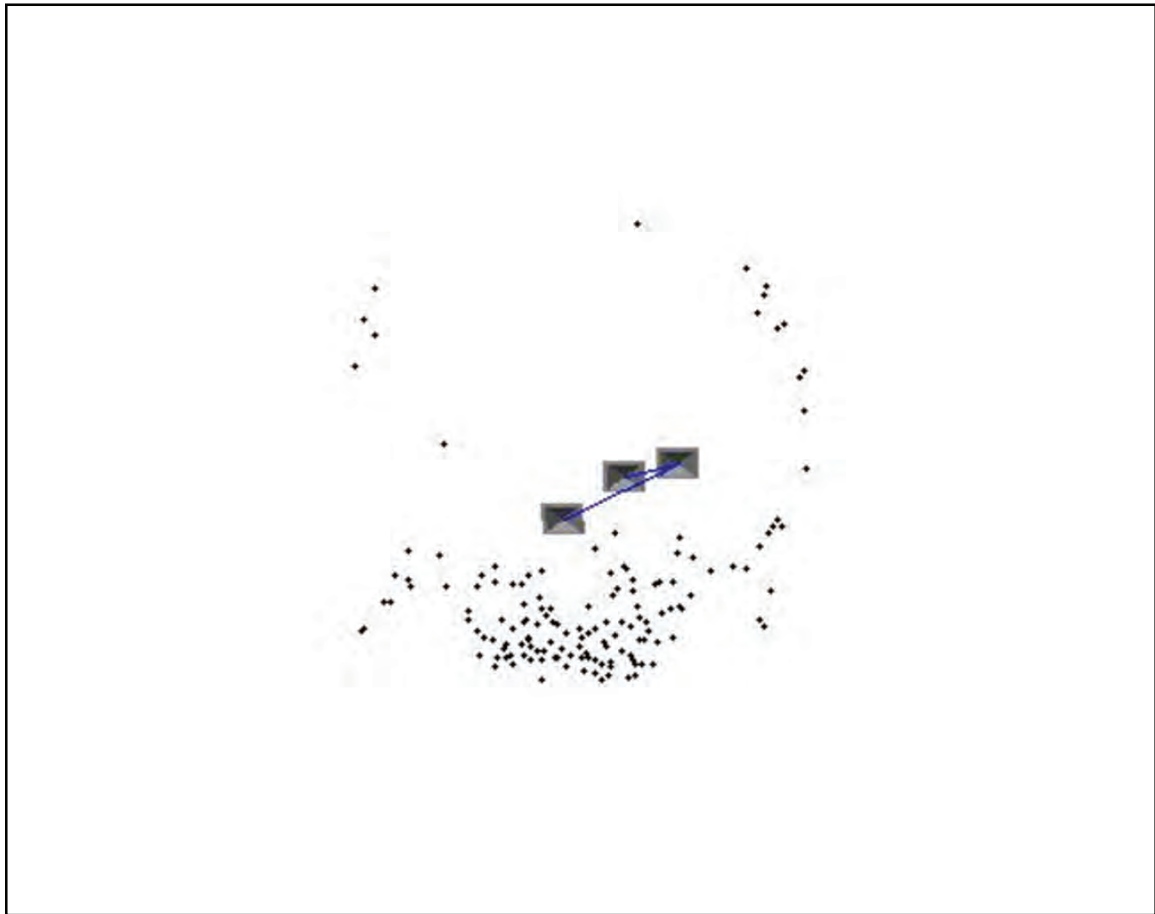


**Figure 55.** This figure shows a sparse point cloud reconstruction of event Tesla, provided key matched points between cameras on the same truck showing the reconstruction perpendicular to camera view direction.

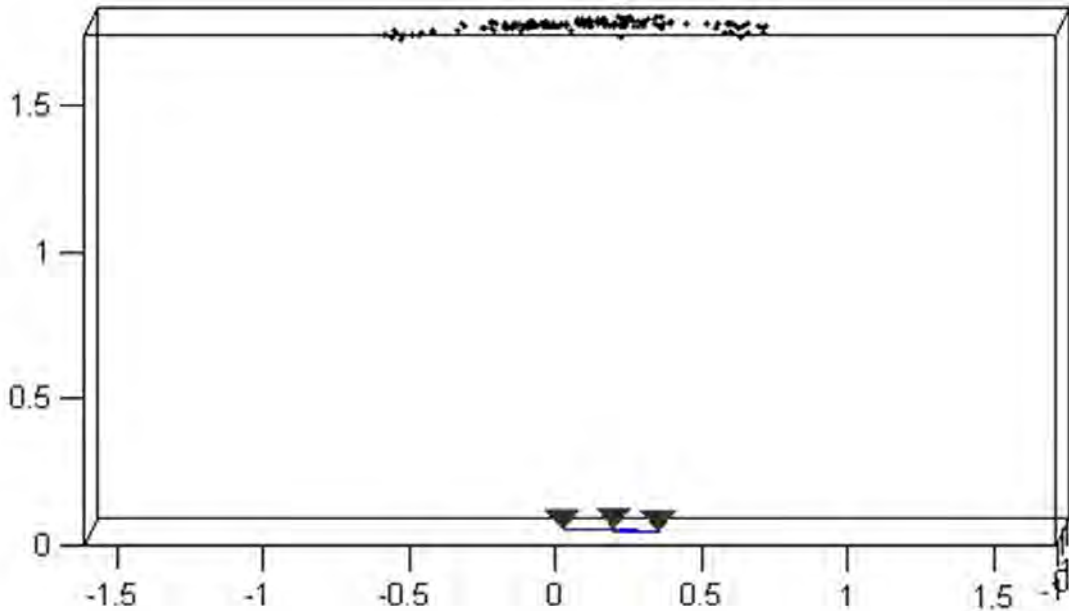


**Figure 56.** This figure shows a sparse point cloud reconstruction of event Tesla, provided key matched points between cameras on the same truck showing the reconstruction parallel to camera view direction.

features from different trucks, to get the required angular separation.

Analysis using SIFT and SURF has shown that these two feature matching techniques do not perform well for large angle separations (greater than  $60^\circ$ ). For all of the test shots analyzed for this work, the use of SIFT and SURF for automatic feature detection and matching across cameras located on different trucks has been unsuccessful. The primary difficulty is that both SIFT and SURF make the assumption that the object doesn't change its output source properties based upon look angle. They both rely upon a differencing method to build a descriptor. A nuclear fireball, however, is a gas. Therefore, it's output is view dependent due to limb-darkening effects.

Limb-darkening has a significant effect on feature matching algorithms. This is highlighted in Figure 57 where eleven manually matched points from two time aligned Tesla images show the drastic variance in apparent brightness from different

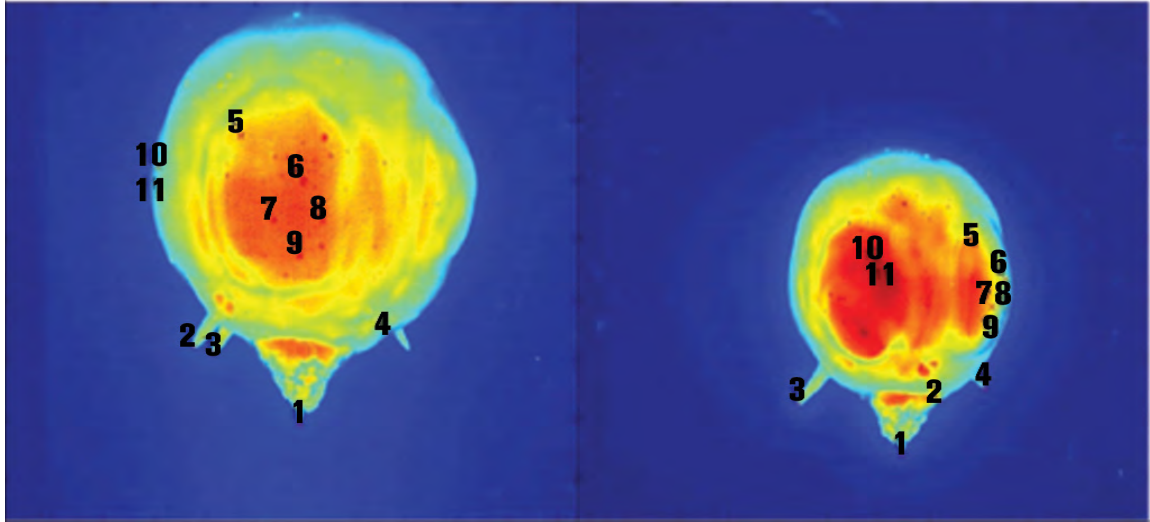


**Figure 57.** The difference in apparent intensity for identical points from different look angles for a nuclear fireball. As can be seen in the figure, matched points have varying intensities and surrounding gradients between these two time matched images for event Tesla.

look angles. Because of intensity differences from varying camera views, any feature matching technique that relies upon descriptors using a first or second derivative of intensity to classify image features will not be capable of matching across different images from cameras on different trucks.

Another example of the difficulties in relating feature points across images from time aligned cameras is highlighted by Figure 58. The FOV separation between the two cameras was under 10 degrees. One of the images was taken at a distance of approximately 5 km and the other at 20 km. The images were captured using an identical film type, filter, and camera. Due to atmospheric transmission the spectrum of light reaching the detector is drastically different. The optical path length of longer wavelengths (red photons) is much longer than shorter wavelengths (blue light). Because of this atmospheric attenuation, key features found on the non-rigid dynamic gas are not consistent even for time aligned small angularly separated cameras. This is because the longer wavelength photons have a higher probability of coming from deeper, more dense, and hotter regions of the fireball. Nuclear fireball observed

features are directly related to not only look angle, but also the spectrum of photons reaching the detector and the detector's response to that spectrum.

## 5.2 3D Reconstruction of a Nuclear Fireball

Due to the lack of varying camera look angles and complexity of performing a 3D reconstruction, the 3D reconstruction of a nuclear detonation requires the use of both single and multiple view image techniques for the majority of United States atmospheric nuclear tests. This section outlines a single image 3D reconstruction technique that uses limb-darkening results in order to determine non-spherical structure. This 3D reconstruction technique uses the fact that higher temperature regions will not only radiate more, but also expand at a faster rate. Therefore, regions of the fireball that are most intense, also have the highest velocities, and ultimately protrude farther out from the center of detonation than other regions. This technique is most similar to structure from illuminance or shape from shading techniques used in a variety of computer vision applications [58, 59, 58, 60].

### 3D Reconstruction Using Limb-Darkening Coefficients.

The single image 3D reconstruction technique outlined in this report is a variation of structure from illuminance or shape from shading that incorporates the limb-darkening intensity roll-off in order to produce fireball shape. The advantage of single image reconstruction techniques is that they do not require a large variance of camera look angles to perform reconstructions. The primary disadvantage is that the reconstruction requires an additional technique such as multiple view geometry or ground truth in order to determine accuracy or uncertainty.

Determining structure from illuminance using limb-darkening is described by the following steps:

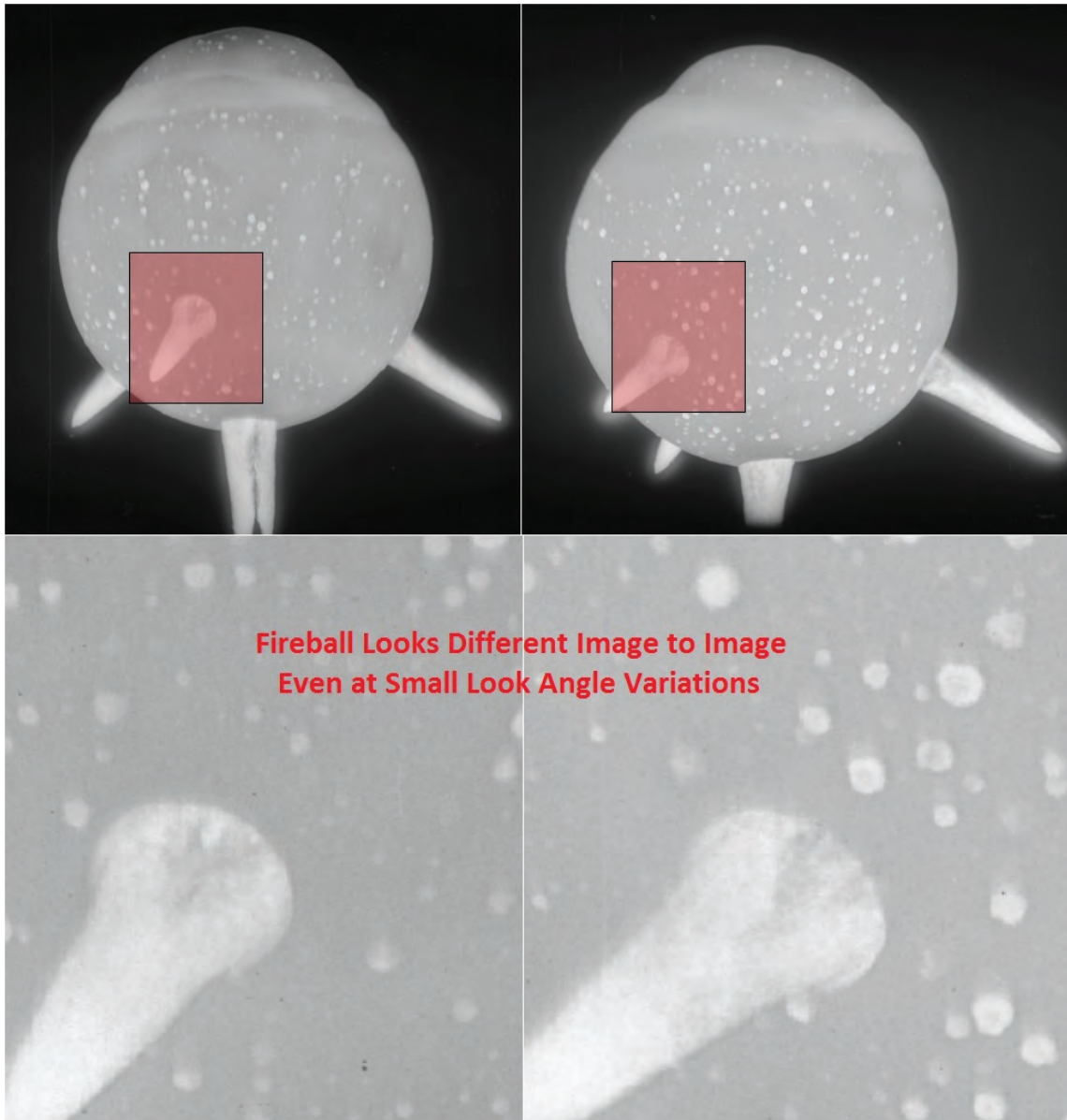


Figure 58. Nuclear fireballs can appear drastically different even at small look angles. The two images, collected using identical cameras, film types, and lenses, are separated by a look angle of approximately  $7^\circ$ , but are at varying distances, 5 km compared to 20 km from ground zero.

1. Determine the center of fireball
2. Calculate  $\theta$ , the angle between the fireball surface and the observer, as shown in Figure 32
3. Use RANSAC to determine limb-darkening coefficients
4. Estimate structure assuming a spheroid
5. Adjust structure based upon observed point radiance relative to expected radiance determined by solved limb-darkening coefficients
6. Perform an averaging filter over the reconstruction to eliminate small hot spots found on many of the nuclear detonations

RANSAC was used to determine the best fit for each frame to the limb-darkening law. The use of RANSAC in 3D reconstruction work is identical to that outlined in Section 4.1. For RANSAC analysis 10 basis points were selected with a distance threshold of 0.15, which was determined from the analysis of varying distance thresholds.

The structure of a nuclear detonation, even for a free air burst, is not entirely spherical. This is predominately due to asymmetries caused by bomb debris and the temperature variation along the surface and inner regions of nuclear fireballs. This is highlighted in the Figure 59, which shows the specific intensity of each fireball pixel as a function of  $\theta$  for a single frame from nuclear test Tesla using RANSAC to determine the best fit line. Of particular note is the wide variation in data, caused by fluctuations in temperature as well as structure (non-spherical). This is further highlighted by comparing Figure 59, a tower shot, to Figure 34, a free air detonation. The tower shot data, shown in Figure 59, has a much lower inlier rate (approximately 60%), compared to Figure 34 (approximately 90%).

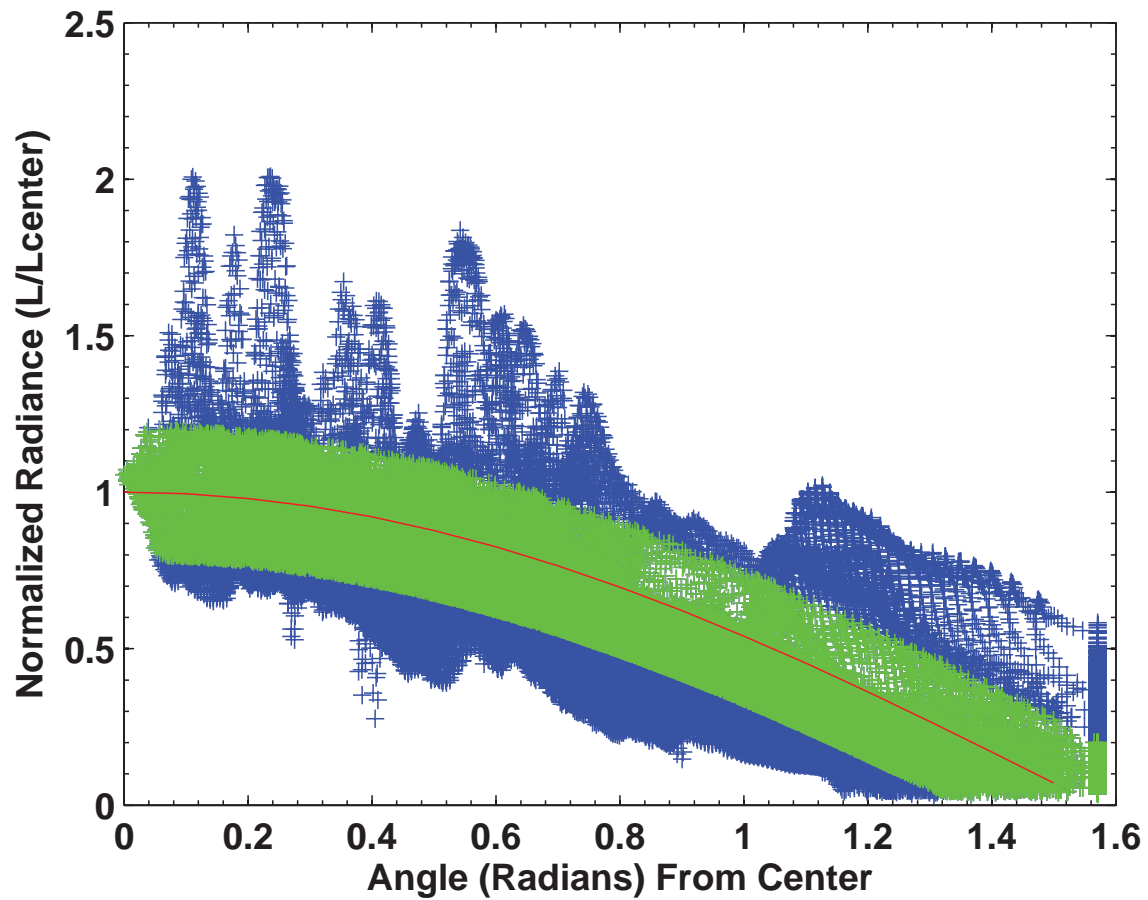
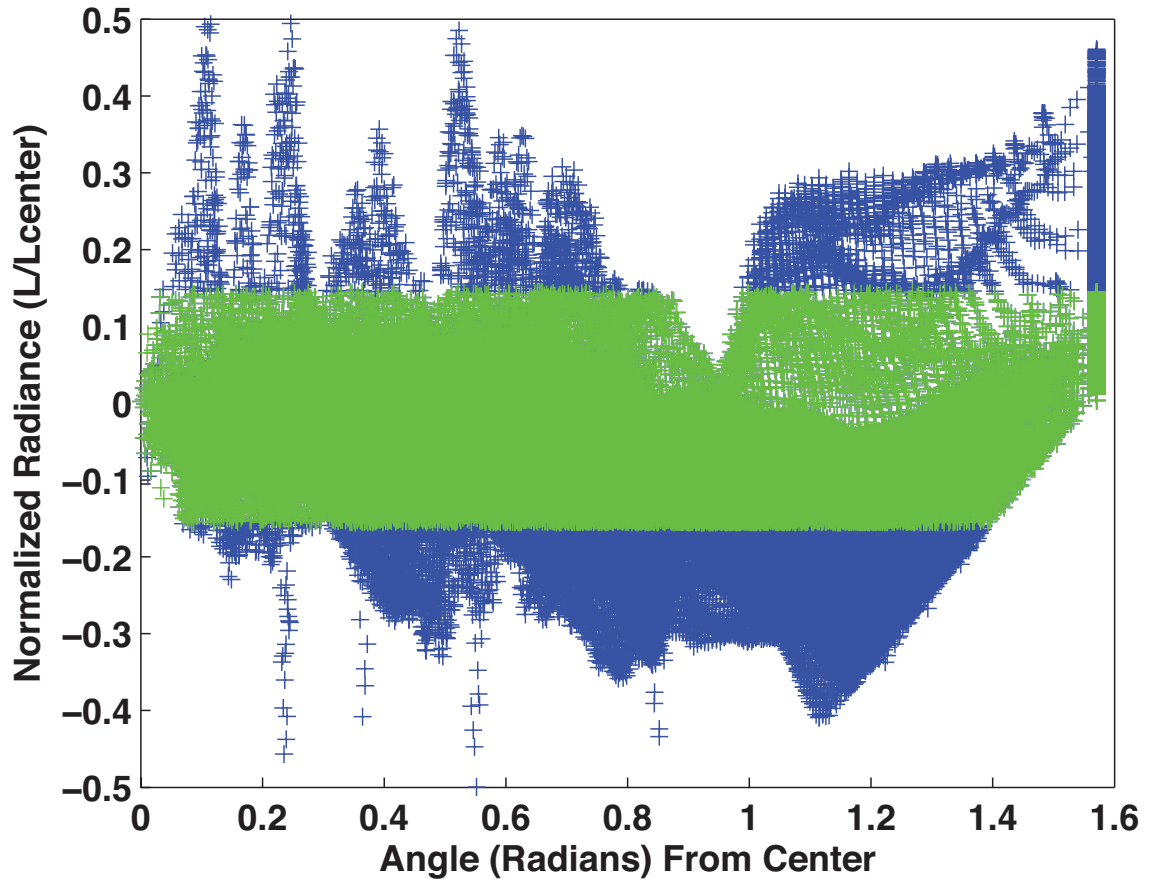


Figure 59. Example results of Wasp Prime best fit using RANSAC. The blue data points are outliers and the green data points are RANSAC inliers.

### Limb-Darkening Coefficients.

For 3D reconstruction research Equation 15 was used for analysis. Figure 59 shows the limb-darkening results for a single frame near the time of  $T_{min}$ . For Figure 59, the green data points are the inliers and blue data points are the outliers. All data points that exceed this defined 0.15 distance threshold are determined to be protruding or receding from the expected spherical shape. This is highlighted in Figure 60, which shows the difference between the expected radiance, determined by the limb-darkening coefficients, and the observed radiance.



**Figure 60.** RANSAC applied to limb-darkening analysis. Blue data points are outliers and green data points are inliers. The height of the data point corresponds to a relative increase in expected depth of the fireball.

Blue data points shown in Figure 60 highlight the pixels that reflect non-spherical

structure in the fireball. These are the features that either protruded (positive values) or receded (negative values) from the expected spheroid shape by a specified amount. The expected spheroid shape is estimated by

$$Z_s = \sqrt{R^2 - X^2 - Y^2} \frac{A^2}{C^2}. \quad (36)$$

$Z_s$  is the depth component of a spheroid,  $X$  (horizontal) and  $Y$  (vertical) are the two spatial dimension of the film,  $A$  is the semi-diameter of the nuclear fireball in the  $X$  direction (set equal to the radius for this work), and  $C$  is the semi-diameter of the fireball in  $Y$  direction. Structure from limb-darkening is set equal to

$$Z_a = Z_s \times SF, \quad (37)$$

where  $Z_a$  is taken as the adjusted depth component factoring in 3D structure, and  $SF$  is the shape function set in this research equal to a form of the logistic function

$$SF = \frac{L}{1 + D \times E^{Int_F}}. \quad (38)$$

$Int_F$  is the normalized radiance (y-axis of Figure 60), and  $L$ ,  $D$ , and  $E$  are appropriate fits determined for different events and different frames. For event Tesla near time of breakaway, appropriate values for  $L$ ,  $D$ , and  $E$  were determined to be 1.43, 1.48, and 0.29 from comparison to a bundle adjusted multiple view geometry solution. The results of these assumptions are shown in Figure 61. Equations 36-38, were developed as original work, to be used as estimates for 3D structure using limb-darkening. It is recommended that through analysis of additional films an understanding of the uncertainties in this approach can be better assessed.

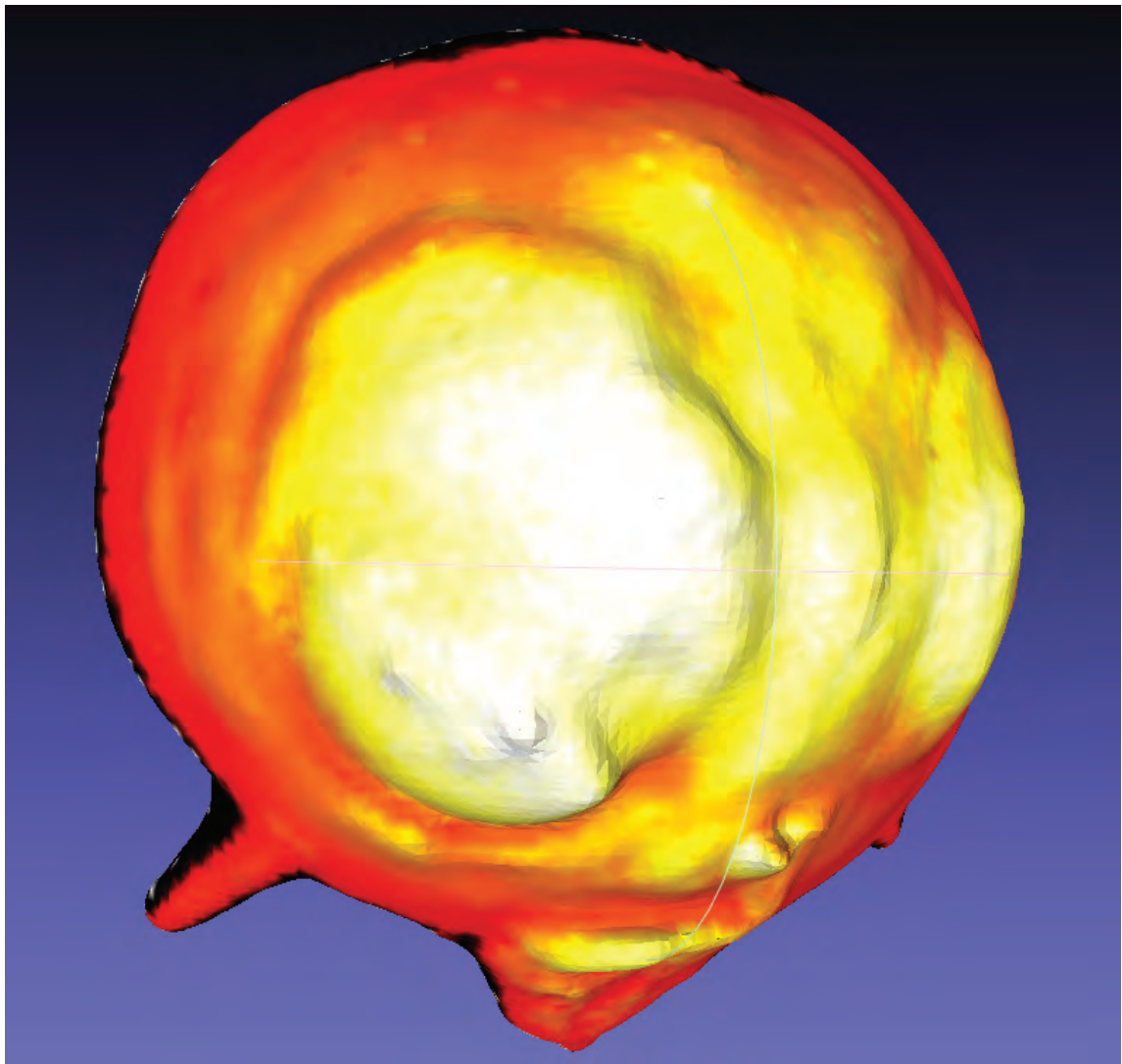


Figure 61. This figure shows the final product of a 3D reconstruction with the projection of a color coded temperature profile of the event.

### **Single Image 3D Reconstruction Limitations.**

Although single image techniques are capable of performing a 3D reconstruction, there is a natural limit to the accuracy in which 3D reconstructions can be achieved from single images. As an example, this particular 3D reconstruction fails to accurately reconstruct the thin protruding spikes created from the fireball interacting with cable lines connected to the tower. The single image reconstruction technique using only structure from limb-darkening coefficients does not capture the proper orientation of this feature leading to an improper reconstruction. These features are also optically thin (less than a few optical path lengths thick) and the current algorithm assumes an optically thick radiating object. This means that even if the temperature at the surface is higher, it is not likely to appear that way, as shown in Figure 25. Additionally, although the reconstruction appears to properly capture the larger protruding regions of the fireball, the exact dimensions of these features are not known outside of a few points, and systematic uncertainties cannot be determined.

All single image reconstruction algorithms must perform a conversion between arbitrary units to proper physical dimensions. For example 3D reconstruction using limb-darkening coefficients (3D shape-from-illuminance) must perform a conversion between relative illuminance to real world depth. Multiple view reconstructions are, therefore, necessary in order to supplement single image reconstruction results. Based upon current research it appears that the combination of single and multiple view techniques are required in order to perform accurate 3D reconstruction for the majority of atmospheric nuclear tests. Current research is focused on developing techniques that can determine automatic key feature descriptors and match those features across cameras located at different viewing locations specifically for nuclear fireballs. This will enable future research to perform automatic sparse reconstructions, provide more insight into the uncertainty of single image techniques, and lead to dense reconstruc-

tion techniques.

### 5.3 Time Alignment Using the Fundamental Matrix

One of the primary concerns when performing time alignment for the nuclear test films is the uncertainty associated with the timing marks burned into the films. The timing mark accuracy (nominally 200 marks per second) is quoted as having a 0.2% error in time [11]. Because of this timing error, matching true time between different cameras begins to have an uncertainty greater than one frame for larger time scales [56]. Fortunately at these larger times, the radial growth is much slower than at earlier times, so it is feasible that uncertainties of plus or minus a frame may still allow for accurate 3D reconstructions using multiple view geometry. It is also possible that this uncertainty at other times may be too severe to allow for proper reconstruction. Because of this uncertainty, an independent method is desired that would be capable of verifying the time alignment between different camera views.

A method, referred to here as F-test, has been outlined that demonstrates the ability to perform frame alignment between a pair of cameras. This method works by using the observation of a dynamically changing event as the key input for time alignment. The process can be outlined as follows:

1. Collect data from at least two cameras viewing the same dynamic event.
2. Determine the epipolar relationship between the two cameras at one instant in time using either portions of the non-dynamic background or scene, or a known time aligned frame. Determine the fundamental matrix using RANSAC to eliminate outliers.
3. Using a single frame from one image/video sequence run through SIFT or SURF matches for the entire other image/video sequence focusing primarily on the

dynamic portions of the scene. Accept only feature matches that pass the fundamental matrix test  $xFx' = t$  using the fundamental matrix derived in step 2, where  $t$  is the user defined acceptance distance threshold.

4. Record the ratio of the number of acceptable matches to the total number of matches that pass this strict F test. If all of the feature points were detected only on the dynamic portion of the scene, and the scene shows movement greater than two pixels per frame, the frame with the highest ratio of accepted matches is the true time matched frame.

An experiment was conducted using a deflating balloon observed by standard commercial video cameras, referred here as camera 1 and camera 2. In the background scene a laptop was used with a real world clock operating to verify the accuracy of time alignment between frames. This experimental setup is shown in Figure 62.

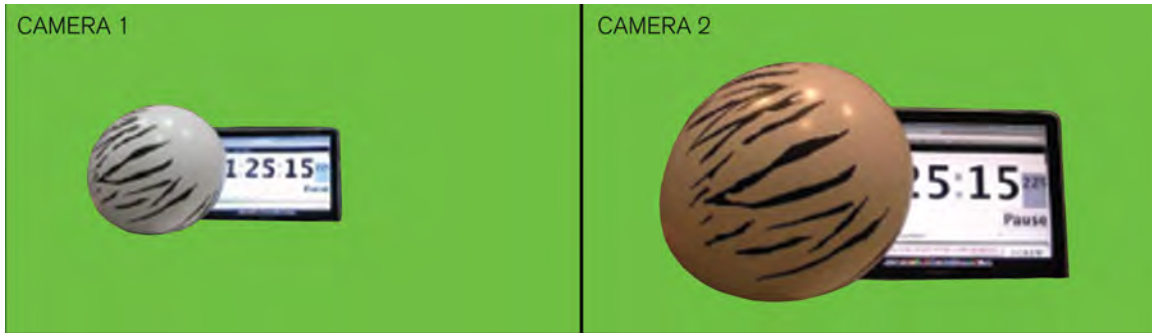


**Figure 62.** Two images from different cameras used to test the theory that the optimizing feature matches between two different cameras using a dynamic region can be used for time alignment. A black and white balloon was deflated while the two cameras recorded data. Camera fundamental matrices were determined using the stationary background. The deflating region was then isolated for each frame.

The balloon was deflated, attempting to simulate a time rate of change in volumetric dimension similar to a nuclear fireball. Figure 63 shows the change in volume as the balloon is deflating through six frames from one of the camera views.

Each camera was stationary during the test, so a single fundamental matrix could be used to determine the epipolar constraint between cameras. A known aligned

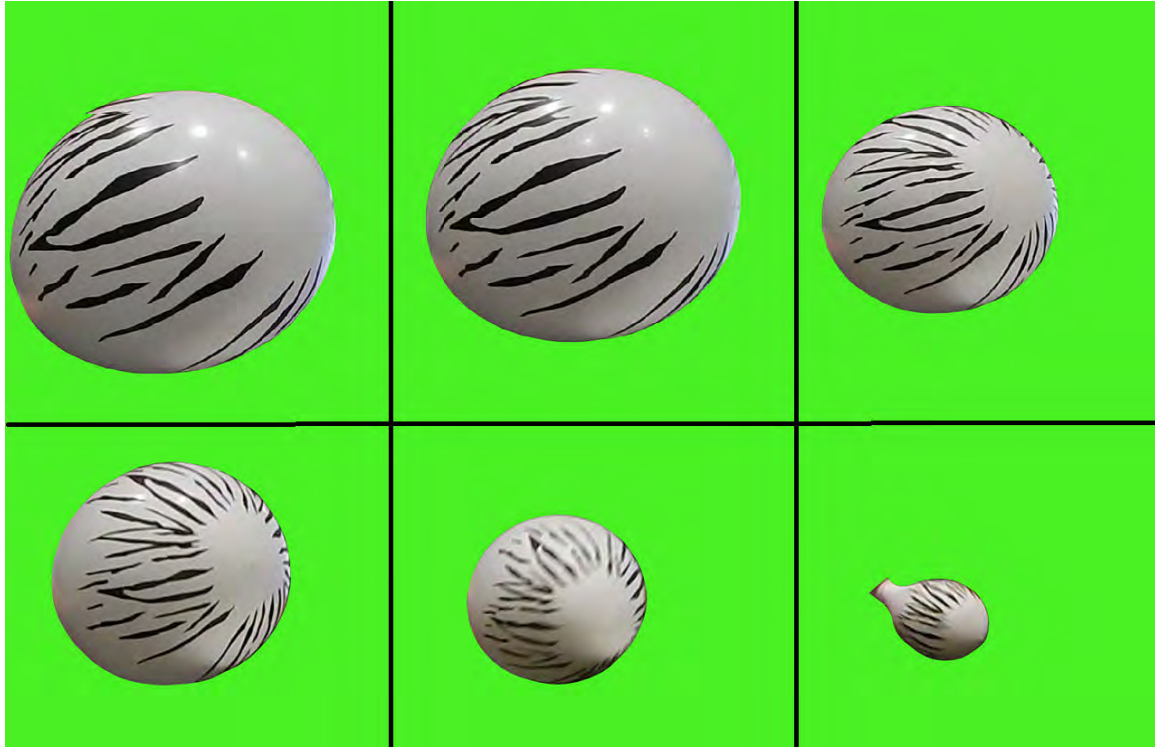


**Figure 63.** Six frames of a balloon used to test whether or not the fundamental null hypothesis could be used to time align separate cameras.

frame match between the cameras was used in conjunction with SIFT algorithms in order to solve for the fundamental matrix. A different frame from camera 1 was then chosen to be matched along all frames from the camera 2 sequence. The results of this feature matching is shown in Figure 64.

Near frame 100, a peak appears that shows that a large concentration of matched points were accepted in this region. This large acceptance rate corresponds to the moment in time in which the dynamic scene is aligned between the two different cameras viewing the event. At frame 103, 100% of all SIFT points passed the fundamental matrix test. The frame with the largest rate of accepted matches is the proper time aligned frame.

This F-test can be performed for an entire sequence of film. Figure 65 demonstrates the results of applying the F-test to camera 1 frames compared to camera 2

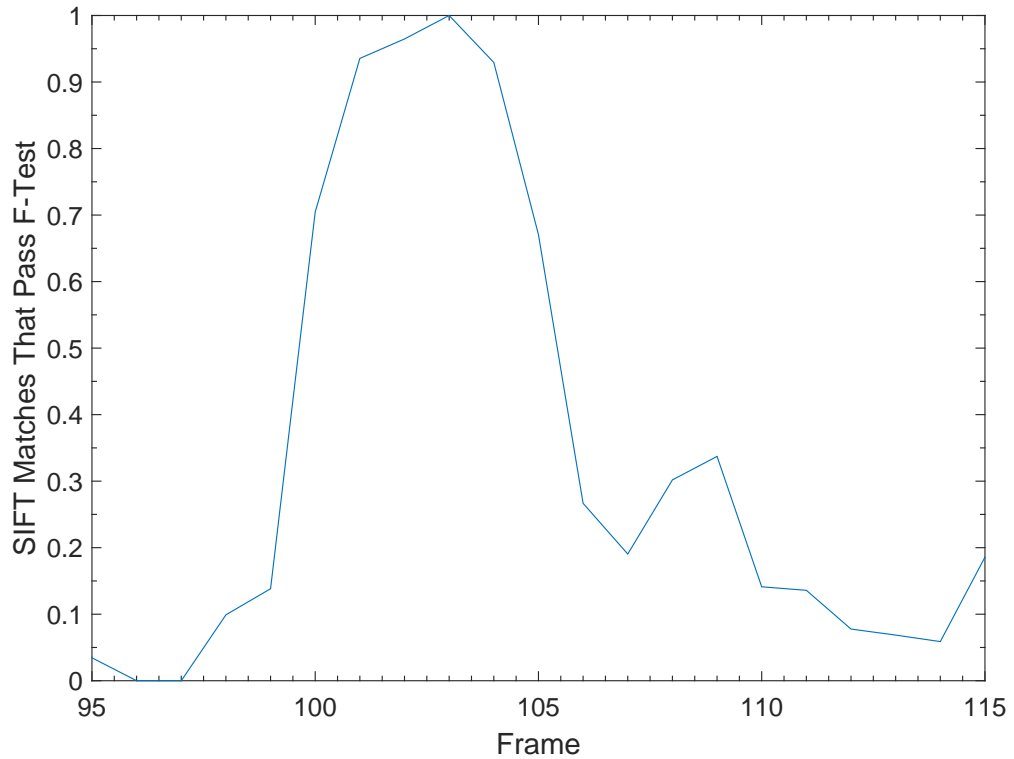


**Figure 64.** The results of attempting to time align two different cameras by optimizing feature matches for a dynamic region. A black and white balloon was deflated while the two cameras recorded data. Camera fundamental matrices were determined using the stationary background. The deflating region was then isolated for each frame. SURF matches for a single frame from the camera on the left (camera 1) was then run against all frames for the camera on the right (camera 2). This plot shows the normalized results of this analysis.

frames focusing on frames that are within  $\pm 3$  frames to the true matched frame. For this test  $t$ , the user defined acceptance distance threshold was set equal to 0.005.

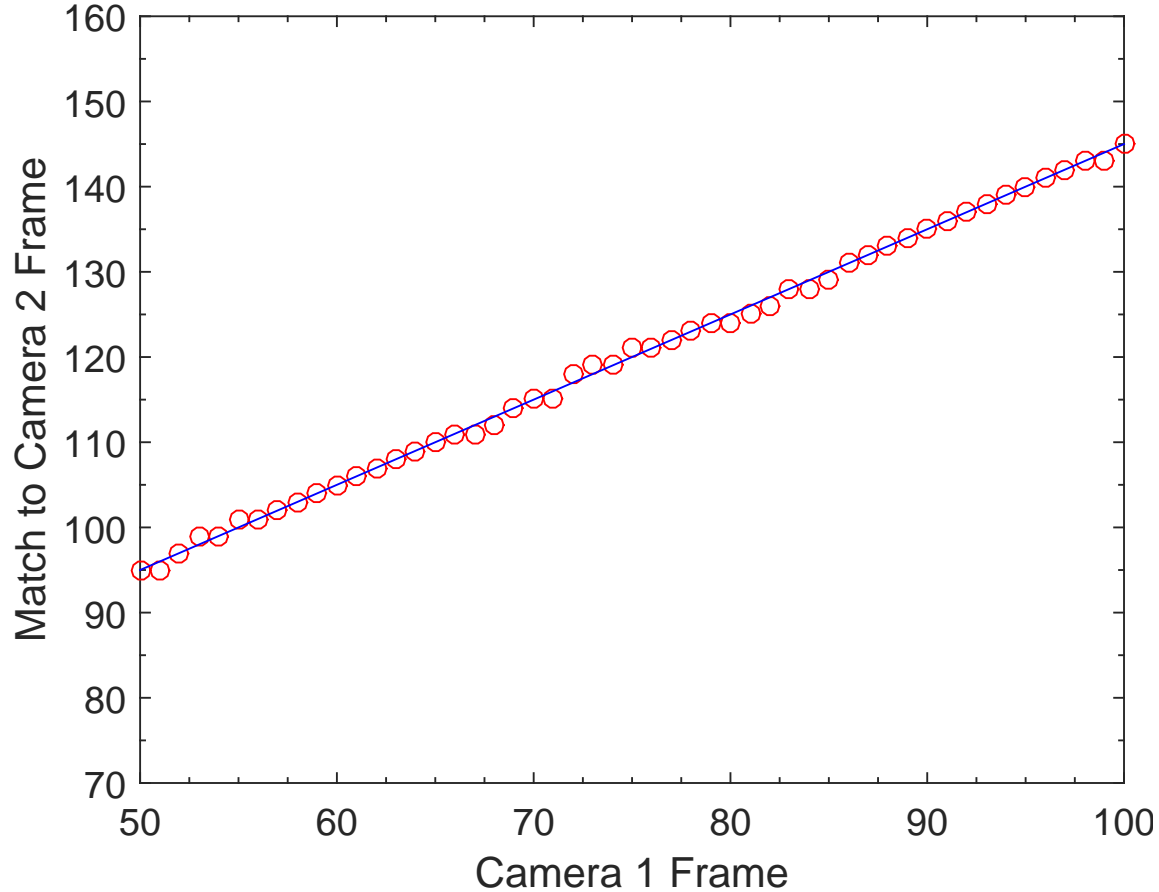


**Figure 65.** The results of time aligning two cameras using the F-Test and a deflating balloon. For this example  $t = 0.005$

Figure 65 demonstrates the ability to match camera frames accurately, identifying the correctly time aligned frame 70% of the time. And being 100% accurate to within 1 frame. For this test sequence both cameras had a frame rate of 29 frames per second with resolutions of 1920 x 1080. This same F-test was conducted for  $t$  values ranging from 0.001 to 1, with results provided by Table 5. Results from Table 5 conclude that for this particular test case that a  $t$  value of 0.005 results in the best percentage of time aligned matches.

This technique could be applied to verify time alignment of frames from nuclear

**Table 5. Time Alignment of Frames Using F-Test**

<b>t</b>	<b>Exact Frame</b>	<b>1-Off</b>
0.001	0.432	0.785
0.003	0.628	0.902
0.005	0.706	1.000
0.01	0.686	0.981
0.03	0.138	0.589
0.05	0.138	0.374
0.1	0.138	0.295
0.3	0.118	0.315
0.5	0.079	0.234
1	0.020	0.138

testing films. The fundamental matrix could be determined by providing matched points for time aligning frames using a distinguishing feature in the films. An example of a distinguishing feature could be the fireball interacting with the same segment of a tower. Once a fundamental matrix is determined, it can be used as the key discriminator of non time-aligned films. A properly time aligned film should read the highest percent of accepted matches at the frame where the dynamic object is most similar between cameras. For this research, this technique was not pursued past initial concept demonstration. The reason, as demonstrated in Section 5.1, is that SIFT and SURF feature descriptors perform poorly for the varying camera view angles found in a nuclear fireball testing film. If an appropriate feature descriptor is developed and validated on nuclear fireball films, then applying the technique outlined in this section may provide significant value for time aligning cameras.

#### 5.4 Discussion

The first dense 3D reconstruction of a nuclear fireball has been produced using a structure-from-illuminance or shape-from-shading variant that incorporates observed and measurable limb-darkening effects. Due to a multitude of reasons, a dense 3D

reconstruction using multiple view geometry has been shown to be physically limited due to the gaseous nature of a nuclear fireball. This is particularly true for the current algorithms generally used for feature detection such as SIFT and SURF. In order to advance the understanding of single image techniques, multiple view geometry is required in order to determine uncertainties. Future research will focus on combining both multiple view and single image techniques in order to produce more accurate 3D models of nuclear fireballs. The focus will be on developing a unique feature identifier and matching algorithm specifically designed for nuclear detonations.

## VI. Conclusions

### 6.1 Dissertation Summary

This dissertation provides multi-dimensional analysis of scanned atmospheric nuclear testing films. The digitized scientific nuclear testing films used for this research were provided by Lawrence Livermore National Laboratories. These films represent a unique data set that allows the scientific community the ability to analyze invaluable historic nuclear weapon effects data using modern digital image processing techniques.

This research developed methods that can be used for 3-dimensional (3D) reconstructions and temperature distributions of the early time nuclear fireballs. Initial developments have resulted in the first 2-dimensional (2D) temperature distribution of a nuclear fireball using digitized film. This temperature analysis underwent validation using the Digital Imaging and Remote Sensing Image Generation (DIRSIG) model which showed agreement within uncertainty between the multi-bounce Monte Carlo DIRSIG model and the analytical calculation. Verification was performed using historical thermal output data in combination with a 1-dimensional (1D) heat flux technique, which showed that the average 2D temperature agreed within  $\pm 5\%$  of the historically bound 1D temperature. Temperature results were then used to derive thermal yield values, which agreed within  $\pm 10\%$  of the historically accepted values.

This same process was extended to perform the first limb-darkening calculation of nuclear fireballs. Limb-darkening coefficients were then used to derive a temperature profile of the nuclear fireball as a function of optical path length. The results indicate that five of the seven laws are consistent with each other, agreeing within 15% out to 5 optical path lengths. These same five limb-darkening laws also agree to within approximately 5% of each other for all times between 2 to 10 ms, but show disagreement between 0.1 ms and 2 ms. For Wasp Prime this time period corresponds to  $T_{min}$ , and

breakaway has been identified as a possible physical reason for the higher uncertainty during this time period. Validation and verification of this technique was performed by comparing a nuclear fireball radiance image derived from limb-darkening coefficients to radiance determined from digitized film corresponding to a time aligned frame. Results showed agreement on average within  $0.125 I_o$ , where  $I_o$  is the radiance at the center of the fireball, for every film and equation analyzed.

The first dense 3D reconstruction of a nuclear fireball has been produced using a structure-from-illuminance or shape-from-shading variant that incorporates observed and measurable limb-darkening effects. A dense 3D reconstruction using only multiple view geometry has been shown to be physically limited. This is predominately due to the inability to automatically generate common features amongst varying images captured from cameras located on different trucks using common computer vision feature descriptors such as Scaled Invariant Feature Transform and Speeded Up Robust Features. However, in order to advance the understanding of single image techniques, multiple view geometry is required in order to determine uncertainties. Accurate dense reconstructions are likely to require both single image and multiple view geometry in order to produce consistently accurate results.

## 6.2 Recommendations for Future Work

1. A calibration standard should be established that accurately maps scanned intensity on the film to optical density. This calibration standard should be scanned once a day in order to ensure no changes have occurred within the scanning process at any point from day-to-day operations. This same or similar calibration source could then also be used between different scanning locations if another organization other than Lawrence Livermore National Laboratory chooses to also scan films. This calibration standard would then allow for

direct comparison of the results from films scanned at multiple locations or from different scanners.

2. Temperature calculations should be conducted for additional films. Included in this dissertation was the introduction, validation, and verification of a temperature calculation that can be used for multidimensional analysis. As more films are scanned this technique should be applied to all appropriate films.
3. Limb-darkening calculations should be further verified with DIRSIG and validated using Taylor's equation. Included in this dissertation was the introduction and verification of a limb-darkening calculation. For a free air detonation, Taylor's equation could be used as a possible validation source if optical path lengths are well known. As more films are scanned this technique should be applied to all appropriate films.
4. A validated feature descriptor and matcher should be developed that can correlate points of a nuclear fireball between films found on different trucks. An ideal feature descriptor and matcher should also be capable of detecting features that have both high, medium, and low pixel intensities. This range of intensity values would allow single image 3D reconstruction using limb-darkening coefficients to be more accurate.
5. Once developed, the validated feature descriptor and matcher could then be used to produce sparse 3D reconstructions. These sparse reconstructions could then be used to ground single image techniques, such as those shown in this dissertation, in order to produce dense reconstructions of nuclear fireballs using automated techniques.

## Bibliography

1. “United States Nuclear Tests July 1945 Through September 1992,” *Department of Energy*, 2000.
2. H. Brode, “Thermal Radiation from nuclear explosions,” The RAND Corporation, Tech. Rep., 1963.
3. H. Bethe, “Theory of the Fireball,” Los Alamos National Laboratory, Tech. Rep., 1964.
4. G. Taylor, “The Formation of a Blast Wave by a Very Intense Explosion. I. Theoretical Discussion,” *Proceedings of the Royal Society of London. Series A, Mathematical and Physical Sciences*, vol. 201, pp. 159–174, 1950.
5. Y. B. Zel'dovich, *Physics of Shock Waves and High-Temperature Hydrodynamic Phenomena*. Foreign Technology Division, 1965.
6. D. Lynes, “An Analysis of Methods to Determine Nuclear Weapon Yield Using Digital Fireball Films,” Master’s thesis, AFIT, 2012.
7. E. Symbalisty, “RADFLO Physics and Algorithms,” LANL, Tech. Rep., 1995.
8. J. McGlaun and S. Thompson, “CTH: A Three-Dimensional Shock Wave Physics Code,” *International Journal of Impact Engineering*, 1990.
9. K. Budge and J. Peery, “RHALE: A MMALE Shock Physics Code Written in C++,” *International Journal of Impact Engineering*, 1993.
10. C. Crepeau, C. Needham, and S. Hikida, *SHAMRC Second-Order Hydrodynamic Mesh Refinement Code Methodology Vol 1*, Applied Research Associates Std., 2001.
11. N. W. E. L. Class, “Nuclear Weapon Effects Laboratory Class,” LLNL, Tech. Rep., 2013.
12. D. Sach, “Manual of Weapon Effects Tests,” Standford research Institute, Tech. Rep., 1957.
13. “Operation Teapot Timing and Firing,” EG&G, Tech. Rep., 1955.
14. “Buster Jangle,” EG&G, Tech. Rep., 1951.
15. “Radiometric Data Reduction System for Photographic Film,” EG&G, Tech. Rep. EGG-1183-414, 1967.
16. R. Hillendahl, “Operation Teapot: Basic Thermal Radiation measurements,” Tech. Rep., 1959.

17. Kodak, "Basic Photographic Sensitometry Workbook," 2006.
18. "Operation Teapot Film Data Sheet Catalog," Report No. LV-193, 1955.
19. C. Pacleb, "Analysis of the Nuclear Thermal Pulse Using Digitized Scientific Test Films," Master's thesis, AFIT, 2012.
20. L. Berkhouse, S. Davis, F. Gladeck, J. Hallowell, C. Jones, E. Martin, F. McMullan, and M. Osborne, "Ball of Fire Observations, Operation Greenhouse," Defence Nuclear Agency WT-101, 1951.
21. J. Palmer, *The Art of Radiometry*. SPIE, 2010.
22. "Kodak Filter No. W-12 (Deep Yellow) product sheet."
23. A. Berk, Anderson, Acharya, Chetwynd, Bernstein, Shettle, Matthew, and Adler-Golden, *Modtran 4 user's manual*, Air Force Research Laboratory, 1999.
24. "Kodak Reference Handbook," Eastman Kodak Company, Tech. Rep., 1946.
25. R. Slaughter, J. McClory, and T. Peery, "Two-Dimensional Temperature Analysis of Nuclear Fireballs Using Digitized Film," *J. Appl. Remote Sens.*, 2015.
26. C. Bridgman, *Introduction to the Physics of Nuclear Weapons Effects*. Fort Belvoir, VA: Defense Threat Reduction Agency, 2001, vol. 8725.
27. E. Dereniak and G. Boreman, *Infrared Detectors and Systems*. Wiley, 1996.
28. S. Brown, *DIRSIG Users Manual Release 4*, Digital Imaging and Remote Sensing Laboratory, 2010.
29. S. Brown and R. Schott, "Verification and Validation Studies of DIRSIG Simulation Model," Digital Imaging and Remote Sensing Laboratory, Tech. Rep., 2010.
30. T. Peery, "Modeling Nuclear Weapon Fireballs in DIRSIG," Master's thesis, Air Force Institute of Technology, 2014.
31. J. Lienhard, "A Heat Transfer Textbook," Phlogiston Press, 1981.
32. W. Fussel, "Color Temperature of Operation Castle," Naval Research laboratory, Tech. Rep., 1955.
33. R. Deuel, "Operation Dial Flower Analysis of High Resolution Optical Data," Defence Nuclear Agency, Tech. Rep., 1974.
34. H. Grier, "Operation Greenhouse Ball of fire observations," EG&G, Tech. Rep., 1951.

35. W. Plum, R. Hillendahl, F. Laughridge, and J. Nichols, "Basic Thermal Radiation Measurements from Ground Stations," U.S Navy Radiological Defense Laboratory, Tech. Rep., 1959.
36. R. Dresser, "Operation Redwing, Thermal Flux and Albedo Measurements from Aircraft," Tech. Rep., 1961.
37. R. Shapley, "On Darkening at the Limb in Eclipsing Variables," *Astrophysical Journal*, vol. 36, p. 239, 1912.
38. Z. Kopal, "Detailed Effects of Limb-Darkening Upon Light and Velocity Curves of Close Binary Systems," *Harvard College Observatory Circular*, vol. 454, pp. 1–12, 1950.
39. A. Diaz-Cordoves, J. and Gimenez, "A New Nonlinear Approximation to the Limb-Darkening of Hot Stars," *Astronomy and Astrophysics*, vol. 259, no. 1, pp. 227–231, 1992.
40. D. Sing and et al, "Transit Spectrophotometry of the Exoplanet HD 189733b," *Astronomy and Astrophysics*, vol. 505, no. 2, pp. 891–899, 2009.
41. A. Claret and P. Hauschildt, "The limb-darkening for spherically symmetric NextGen model atmospheres: A-G main-sequence and sub-giant stars," *Astronomy and Astrophysics*, vol. 412, no. 1, pp. 241–248, 2003.
42. D. Klingsmith and S. Sobieski, "Nonlinear Limb Darkening for Early-Type Stars," *Astronomical Journal*, vol. 75, no. 2, p. 175, 1970.
43. A. Claret, "A New Non-Linear Limb-Darkening Law for LTE Stellar Atmosphere Models," *Astronomy and Astrophysics*, vol. 363, pp. 1081–1190, 2000.
44. D. Sing, "Stellar Limb-Darkening Coefficients for CoRot and Kepler," *Astronomy and Astrophysics*, vol. 510, no. A24, 2010.
45. P. Tremblay and P. Bergeron, "Spectroscopic Analysis of DA White Dwarfs: Stark Broadening of Hydrogen Lines Including Non-Ideal Effects," *Astrophysical Journal*, vol. 696, pp. 1755–1770, 2009.
46. e. a. A. Gianninas, "Limb-Darkening Coefficients for Eclipsing White Dwarfs," *Solar and Stellar Astrophysics*, 2013.
47. K. Schwarzschild, "Über das Gleichgewicht der Sonnenatmosphäre," *Göttinger Nachrichten*, vol. 41, pp. 1–24, 1906.
48. D. Schmitt, R. Slaughter, and G. Peterson, "Quantifying 3D Positional Uncertainty of Radiological Material From Nuclear Detonation Video," *Nuclear Science and Engineering*, 2015.

49. M. Fischler and R. Bolles, “Random Sample Consensus: A Paradigm for Model Fitting with Applications to Image Analysis and Automated Cartography,” *Commun. ACM*, vol. 24, no. 6, pp. 381–395, Jun. 1981. [Online]. Available: <http://doi.acm.org/10.1145/358669.358692>
50. P. Torr and A. Zisserman, “MLESAC: A New Robust Estimator with Applications to Estimating Image Geometry,” *Computer Vision and Image Understanding*, 2000.
51. M. Agrawal and K. Konolige, “FrameSLAM: From Bundle Adjustment to Real-Time Visual Mapping,” *IEEE Transaction on Robotics*, 2009.
52. P. Meer, C. Stewart, and D. Tyler, “Robust Computer Vision: An Interdisciplinary Challenge,” *Computer Vision and Image Understanding*, 2000.
53. R. Hartley, *Multiple View Geometry in Computer Vision*. Cambridge, 2003.
54. K. Walli, “Relating Multimodal Image Data in 3D,” Ph.D. dissertation, Rochester Institute of Technology, 2010.
55. C. Harris, “A Combined Corner and Edge Detector,” Tech. Rep., 1988.
56. S. Lowe, “Distinctive Image Features from Scale-Invariant Keypoints,” Tech. Rep., 2003.
57. H. Bay, “Speeded-Up Robust Features (SURF),” Tech. Rep., 2008.
58. K. Ikeuchi and B. Horn, “Numerical Shape from Shading and Occluding Boundaries,” *Artificial Intelligence*, 1981.
59. B. Horn and M. Brooks, “The Variational Approach to Shape From Shading,” *Computer Vision, Graphics, and Image Processing*, 1986.
60. S. Loncaric, “A Survey of Shape Analysis Techniques,” Tech. Rep., 1998.

## REPORT DOCUMENTATION PAGE

Form Approved  
OMB No. 0704-0188

The public reporting burden for this collection of information is estimated to average 1 hour per response, including the time for reviewing instructions, searching existing data sources, gathering and maintaining the data needed, and completing and reviewing the collection of information. Send comments regarding this burden estimate or any other aspect of this collection of information, including suggestions for reducing the burden, to Department of Defense, Washington Headquarters Services, Directorate for Information Operations and Reports (0704-0188), 1215 Jefferson Davis Highway, Suite 1204, Arlington, VA 22202-4302. Respondents should be aware that notwithstanding any other provision of law, no person shall be subject to any penalty for failing to comply with a collection of information if it does not display a currently valid OMB control number.

**PLEASE DO NOT RETURN YOUR FORM TO THE ABOVE ADDRESS.**

1. REPORT DATE (DD-MM-YYYY) 17-09-2015	2. REPORT TYPE Dissertation	3. DATES COVERED (From - To) October 2012 - September 2015		
4. TITLE AND SUBTITLE  Multidimensional Analysis of Nuclear Detonations		5a. CONTRACT NUMBER		
		5b. GRANT NUMBER		
		5c. PROGRAM ELEMENT NUMBER		
6. AUTHOR(S) Slaughter, Robert C., Captain, USAF		5d. PROJECT NUMBER		
		5e. TASK NUMBER		
		5f. WORK UNIT NUMBER		
7. PERFORMING ORGANIZATION NAME(S) AND ADDRESS(ES) Air Force Institute of Technology Graduate School of Engineering and Management (AFIT/EN) 2950 Hobson Way Wright-Patterson AFB OH 45433-7765		8. PERFORMING ORGANIZATION REPORT NUMBER AFIT-ENP-DS-15-S-029		
9. SPONSORING/MONITORING AGENCY NAME(S) AND ADDRESS(ES) National Nuclear Security Administration U.S. Department of Energy 1000 Independence Ave., S.W. Washington D.C. 20585 POC: Dr.Vaughn Standley, vaughn.standley@nnsa.doe.gov		10. SPONSOR/MONITOR'S ACRONYM(S) NNSA		
		11. SPONSOR/MONITOR'S REPORT NUMBER(S)		
12. DISTRIBUTION/AVAILABILITY STATEMENT DISTRIBUTION STATEMENT A: APPROVED FOR PUBLIC RELEASE; DISTRIBUTION UNLIMITED.				
13. SUPPLEMENTARY NOTES This material is declared a work of the U. S. Government and is not subject to copyright protection in the United States				
14. ABSTRACT The focus of this research is to develop the methods for 3-dimensional reconstructions and temperature distributions of early time nuclear fireballs. Initial developments have resulted in the first 2-dimensional temperature distribution of a nuclear fireball using digitized film. This same process was then extended to perform the first limb darkening calculations of nuclear fireballs. Limb darkening coefficients were then used to derive a temperature profile of the nuclear fireball as a function of optical path length. A 3-dimensional reconstruction was performed using a variation of a structure from illuminance technique in combination with limb darkening coefficients to produce structure using a single image. This dissertation also highlights the difficulties in using common computer vision feature descriptors such as Scaled Invariant Feature Transform and Speeded Up Robust Features on nuclear weapons testing data. The use of these techniques to produce accurate dense reconstructions is likely to require both single image and multiple view geometry in order to produce consistently accurate results.				
15. SUBJECT TERMS Nuclear detonations, Nuclear fireballs, digitized film, 3D reconstruction, thermal analysis, fireball temperature, limb darkening, nuclear films, time alignment, digital image processing, computer vision				
16. SECURITY CLASSIFICATION OF: a. REPORT U b. ABSTRACT U c. THIS PAGE U		17. LIMITATION OF ABSTRACT UU	18. NUMBER OF PAGES 133	19a. NAME OF RESPONSIBLE PERSON Dr. John McClory, AFIT/ENP 19b. TELEPHONE NUMBER (Include area code) (937) 255-3636 x7308 john.mcclory@us.af.mil